Biennial Scientific Report
2003 – 2004

Weather, Climate and Seismology

Contents

Preface

Introduction

Highlights

Severe weather research and the link to operations 12
The Numerical Weather Prediction development chain 22
A modern strategic approach on the redesign of synoptical observations networks 28
Development of the KNMI Operational Data Centre (KODAC) 32
European Climate Assessment & Dataset project (ECA&D) 36
First results of the Ozone Monitoring Instrument 40
Using Lidar/Radar observations to improve cirrus cloud parameterisations 44
Estimating extreme wave height probabilities from observations and the ERA-40 reanalysis 48
CLIWOC - the climatological database for the world's oceans 52
Simulation of present-day and future climate with RACMO2 56
The coupling between the stratosphere and the troposphere 62
Past climate changes 66
Assessing the skill of seasonal forecasts 72
The Challenge project: ensemble simulations of the global climate 78
Seismic hazard in the North of The Netherlands 84

Appendices

Organisational charts 90
Publications
· *Numerical Modelling Research and Development 92*
· *Observations Research and Development 96*
· *Climatological Services 100*
· *Climate Variability Research 102*
· *Oceanographic Research 104*
· *Atmospheric Research 107*
· *Atmospheric Composition Research 112*
· *Climate Analysis 120*
· *Policy Advice and Related Services 122*
· *Seismology 124*

Acronyms

Preface

In the past KNMI has published biennial reports on weather, climate and seismology research in separate volumes. The tradition of publishing reports on KNMI's research continues with this fifth report, in which for the first time all research topics are combined in one volume. This is not only convenient for the interested reader, but also expresses the intention of the Management Team to establish a closer cooperation between weather and climate research.

Closer cooperation within KNMI in the fields of weather and climate will be profitable for KNMI in general, e.g. in the field of modelling. The need for closer cooperation in these fields was also recommended by the international commission which reviewed KNMI's research programme in the beginning of 2004.

For me personally, the results of the Challenge project (ensemble simulations of the global climate) constitutes the highlight of KNMI-research in this period, as it directly contributes to answering the major question posed by the Dutch Government to KNMI: 'How will the climate change in our part of the world?'.

Aside from the Challenge results, there are many more highlights presented in this volume. I trust that everybody will find something of interest in this report. I wish you pleasant reading and thank all KNMI-colleagues who contributed to our research successes.

Dr. Ir. Frits J.J. Brouwer
Director-General KNMI

Introduction

The Royal Netherlands Meteorological Institute provides data, knowledge and information in the fields of weather, climate and seismology. Research is conducted in each of these areas. The research programme encompasses experimental, modelling and theoretical elements.

KNMI delivers weather products to the general public, to public organisations and to weather related businesses. The main aim is to provide these products to society in support of economic activity and public safety. In support of KNMI's operation department, which delivers the weather products, weather research at KNMI aims at delivering new and improved methods of observation and prediction. These efforts span a broad part of applied meteorology and range from observation applications research to air-sea interaction modelling. Much research effort goes into methods for the detection and prediction of severe weather, the monitoring of extremes, the definition of weather alarm levels, and the development of alarm indicator tools. This research helps fulfil an important task of the institute, i.e. to provide warning of meteorological hazardous situations. An important research focus at KNMI is the HIRLAM Numerical Weather Prediction model, which is developed and maintained in an international collaborative framework. HIRLAM is run and used operationally at KNMI and provides an integration framework for the improved observation and understanding of weather processes. In addition, at KNMI development work is done to support data reception, processing and storage. This activity especially benefits work related to climatological research and satellite observations. In this report, several projects underpinning the various goals described above are highlighted.

Climate research continues to be of great importance to society. On the basis of assessments made by international bodies, such as the Intergovernmental Panel on Climate Change and following progress made by the United Nations Framework Convention on Climate Change, the government of the Netherlands is

implementing a far-reaching adaptation and mitigation policy. At the same time, there is an increasing awareness of a number of weak points in our understanding of the climate system and the limitations to the predictability of climate. KNMI's climate research has responded to these developments by focusing on: 1. reduction and/or quantification of uncertainty; and 2. the development of climate scenario's for decision making. This research is done in a large number of national and international projects often under the umbrella of international programmes such as the World Climate Research Programme, the Global Climate Observing System, the related Earth Observation System and the International Biosphere Geosphere Programme. This report highlights some of the results of the past two years in observations (ozone, cirrus cloud, ocean data), understanding (simulation past and present climates, stratosphere/troposphere coupling) and predictability (skill of seasonal forecasts, ensemble simulations of the global climate). Public research is not complete without the effective communication of results to society. KNMI strives to achieve this in an objective, factual and transparent manner which is neutral with respect to policy while serving as broad an audience as possible. Outreach activities are described in the section on "Policy advice and related services" (see page 122-123).

The Seismology Division has both an operational and a research task. Operationally, it is responsible for the monitoring of seismic events. Its research programme focuses on the assessment of seismic risk for both natural and induced events. In addition, it has a programme on atmospheric infrasound and activities related to the implementation of the Comprehensive Nuclear-Test-Ban Treaty. This report describes progress made on quantifying seismic hazards in the north of The Netherlands.

In February 2004 an international committee reviewed KNMI's research programme. This committee identified many research efforts of high international quality, but also made some suggestions for improvement. Notably, the need for an improved relationship between research and services in all three areas, weather, climate and seismology, and the need to improve the synergy between weather

and climate research, particularly in the field of model development. At the time of writing of this Introduction actions are being taken to implement these recommendations.

This fifth Biennial Report presents 15 research highlights, followed by overviews of publications per Division. New, this edition, is the bringing together of weather, climate and seismological research in one single document. We hope this new format contributes to an improved presentation of the research conducted at KNMI.

Dr. Sylvia Barlag
Head Observations and Modelling Department

Prof. Dr. Gerbrand Komen
Head Climate Research and Seismology Department

Highlights

Severe weather research and the link to operations

Iwan Holleman, Albert Jacobs, Kees Kok, Vladimir Makin, Hans Roozekrans, Maurice Schmeits, Paul de Valk, Daan Vogelezang, Hans de Vries and Ben Wichers Schreur

Introduction

KNMI's major focus in meteorological research is to better observe, understand, and forecast severe weather events, and to link research knowledge and products to operations and warning systems.

New generation observing systems, such as the Meteosat Second Generation (MSG) satellite, enable us to observe the state of the atmosphere with much higher spatial and temporal resolution. At the same time new techniques and methods have been developed which can be applied to retrieve more information from measurements, such as high quality wind profiles from Doppler weather radar, and thunderstorm development, fog, and low stratus clouds from MSG.

Life–threatening situations and economic losses caused by severe weather should be minimized. We realize, and even demonstrated on occasion, that the forecast quality of our present-day models has improved significantly, and even might be sufficient to timely warn for disasters like the extensive floodings caused by the 1953 storm surge. But next to the forecaster, authorities responsible for public safety require adequate and timely information, and should be made aware as well. As a result part of our focus has shifted towards transferring knowledge and linking developed forecast methods to warning systems.

Fundamental research, increasing the understanding of atmospheric and air-sea processes that lead to extreme weather events, such as hurricane type winds, is needed, and at the same time is challenging, as well. A broad field with many players from the different disciplines of research, application development, operations, and user community, should be covered altogether. In order to keep our focus, and prevent waste of our scarce means, we recently launched a severe weather programme under which innovation on severe weather research and warning systems will be carried out in a controlled way.

This highlight gives a selection of the achievements that have been accomplished on severe weather research in recent years. We start with the detection of winds by Doppler radar, the development of a new wind gust prediction scheme, and some new unexpected results on the impact of hurricane type winds on the drag of the sea surface. Hereafter we present the new MSG satellite imageries and their application products. We then focus on the development and use of warning systems for extreme weather events. Here we present a probabilistic forecast system for (severe) thunderstorms and a warning system for extreme precipitation amounts for the Dutch Water Boards. Finally we demonstrate how present-day operational weather and sea-state forecasting models would have performed on the disastrous storm surge of 1953.

Wind observations by Doppler radar

Doppler weather radars are capable of providing high quality wind data at a high spatial and temporal resolution. This kind of data is of great value for operational weather forecasting and Numerical Weather Prediction models. Operational application of Doppler velocity data is hampered by the rather low unambiguous velocity, typically 10-15 m/s for a C-band radar. The so-called 'dual-PRF technique' can be employed to extend this unambiguous velocity by a factor of three or more, but it gives rise to a small fraction of de-aliasing errors (1-2 %). At KNMI we have performed an extensive analysis of dual-PRF velocity data and we have developed a post-processing algorithm for correction of the data[1)].

Figures 1a and 1b show the raw and post-processed velocity data obtained during the passage of a cold front. It is evident from Figure 1a that the raw velocity data contain numerous de-aliasing errors. After the first pass of the post-processing algorithm only two de-aliasing errors remain (see Figure 1b), and a second pass corrects these. The performance of the algorithm has been evaluated by processing and analysing roughly 300 Doppler scans. It is found that the post-processing algorithm efficiently corrects de-aliasing errors and that it produces velocity data of high quality. Further application of Doppler radar data in wind profiling, shear detection, dual-Doppler analyses, and NWP models is facilitated by this work.

Doppler weather radars can only observe the line-of-sight component of the three-dimensional wind field, the so-called radial velocity. However, wind profiles above the radar site can be retrieved using dedicated methods. When the observed radial velocity

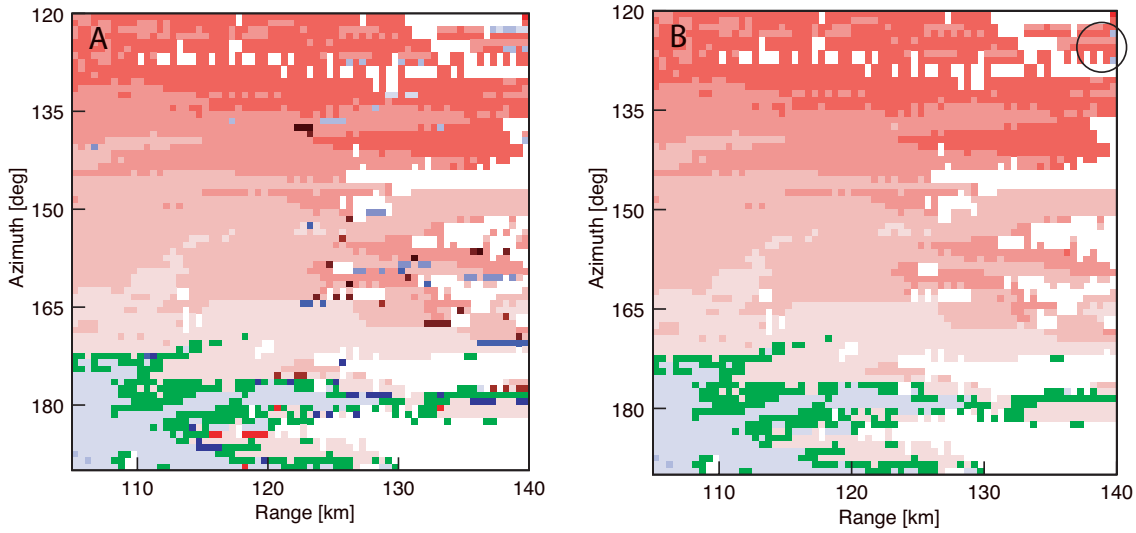

Figure 1. Part of the raw (a) and post-processed (b) velocity data obtained during the passage of a cold front. The circle marks two aliasing errors that are not corrected after the first pass of the algorithm.

Severe weather knowledge and methods finding their way to operations and warning systems

is displayed as a function of azimuth, the resulting curve will have the form of a sine. The wind speed and direction can be determined from the amplitude and the phase of this sine. Nowadays, two different metho ds (known as Velocity Azimuth Display and Volume Velocity Processing VVP) are widely used to retrieve wind profiles from Doppler radar observations. Despite the widespread use of these two retrieval methods, only a few verification studies have been reported and no intercomparison study has been published.

At KNMI we have performed an intercomparison of the two retrieval methods and an extensive verification of the retrieved wind profiles against radiosonde and Hirlam profiles[2]. Nine months of wind profile data have been used for this intercomparison and verification. It is found that the most simple implementation of the VVP retrieval method provides the best wind data. Figure 2 shows the calculated bias and standard deviation of the VVP wind profiles against the Hirlam background. For both Cartesian components, a small positive bias and a standard deviation between 2.0-2.5 m/s are found. In fact these observation minus background statistics are at least as good as those of radiosonde profiles (not shown), and this demonstrates the high quality of the Doppler radar wind profiles.

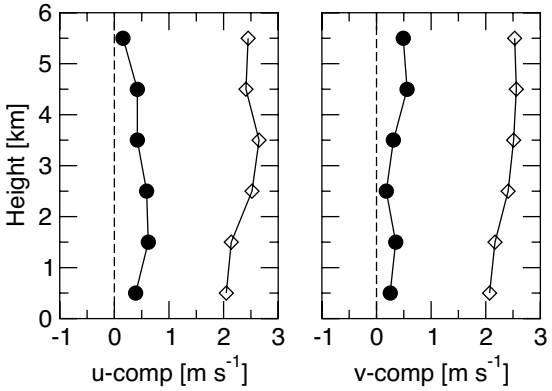

Figure 2. Profiles of the bias (bullets) and standard deviation (diamonds) of the Cartesian u- and v-components from the verification of the VVP wind data against the Hirlam model.

Extreme wind: detection and prediction

The prediction and detection of extreme wind conditions are important aspects of weather warnings and alarms. High winds and wind gusts affect both the safety and economy of traffic in general and in shipping, high speed trains and airport operations in particular. Extreme wind conditions may also cause substantial damages to property. An increase in the reliability of extreme wind warnings and alarms requires research and development into all aspects of

Knowledge of air-sea interaction at hurricane wind speeds is of primary importance for severe weather forecasts, extreme sea-state forecasts, marine engineering, and public and transport safety

the production chain leading to the issue of weather warnings and alarms: from improved understanding of the probabilistic nature of wind gusts through to the development of support tools for operational forecasters and applications for end users. Several projects have contributed to advances in the area of extreme wind forecasting.

GUSTO

Traditional wind gust forecasts at KNMI are based on a combination of the Wieringa[3] gust theory for high wind, near neutral stability conditions and a statistical regression developed by Ivens[4] for the maximum wind velocity associated with squalls and heavy showers in autumn and winter, based on upper air measurements. The Wieringa gust theory provides the median maximum gust in relation to the mean wind speed and surface roughness. In the GUSTO project an alternative theory, starting from earlier work by Beljaars[5], was developed that provides an explicit relation between the probability of exceeding a gust threshold and the mean wind speed, surface roughness, height above the surface, length of the forecast interval, characteristic time scale of the turbulence and in the case of measurements the characteristics of the measurements and the size of the observation network. The increased understanding of the dependence of gusts on these parameters allows for a wider application of the theory. GUSTO has been applied to the characterization of building induced wind disturbances at the airports of Amsterdam (Figure 3) and Hong Kong and to a crosswind related aircraft landing incident investigation. GUSTO has been used to implement a TKE based gust prediction scheme in HIRLAM. This prediction is routinely available to forecasters along with a prediction of convective gusts from the Ivens regression applied to HIRLAM forecasts.

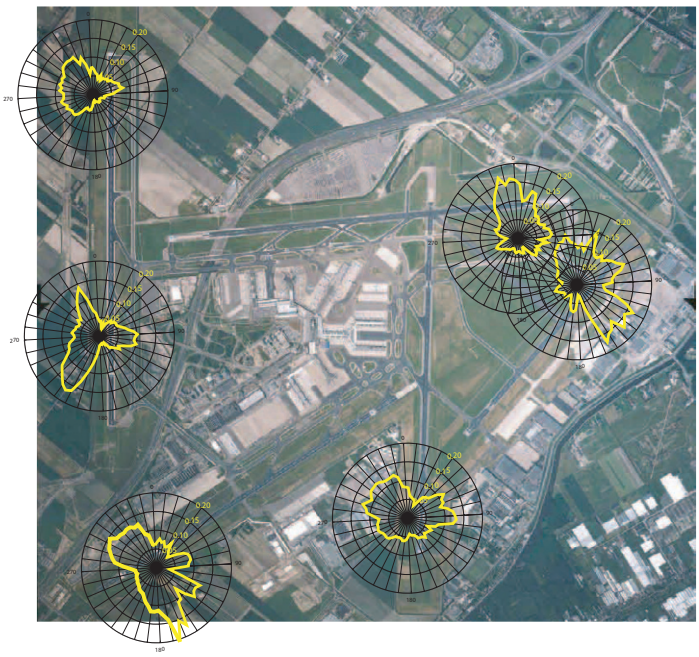

Figure 3. GUSTO has been used to characterize building induced windhinder at Schiphol airport through an analysis of the directional dependence of the effective roughness marked in yellow at the six windmasts of the airport.

Tuning of CBR (Cuxart, Bougeault, Redelsperger)

The introduction of surface stress turning in CBR[6], the prognostic TKE scheme of HIRLAM, has eliminated the need for an artificial increase in vertical mixing under stable conditions and has led to an improvement in surface wind forecasts and wind profiles, in particular of low level jets, while maintaining synoptic quality[7].

Pseudo satellite imagery

The occurrence of gusts near so-called 'dark stripes' deserves the forecaster's attention. Pseudo satellite imagery and model cross-sections based on HIRLAM output have been developed as a support tool for the forecaster to monitor, interpret and evaluate model output in these cases[8].

Drag of the sea surface at hurricane winds

Knowledge of the air-sea interaction at hurricane wind speeds is of primary importance for severe weather forecasts, extreme sea-state forecasts, marine engineering, and public and transport safety. Up to now little was known on this subject, and formulations of the sea drag for the above mentioned problems were, and still are, simply extrapolated from parameterisations obtained for much lower wind speeds. A comprehensive field study of the air-sea interaction at high wind speeds in tropical cyclones was recently reported by Powell et al[9]. The authors obtained quite an unexpected result that at the wind speed increasing above the hurricane force of about 33 m/s the drag coefficient levels off and starts to decrease with

a further increase in the wind speed. This is contrary to the behaviour of the drag coefficient parameterisations that are currently used in ocean applications. This result is illustrated in Figure 4, where the friction velocity u_* and the drag coefficient at 10 meter height defined as

$$CD_{10} = \frac{u_*^2}{u_{10}^2}$$

are shown (u10 is the wind speed at 10 meter height). The drag coefficient and the friction velocity that follow from the logarithmic profile

$$u(z) = \frac{u_*}{\kappa} \ln \frac{z}{z_0}$$

and the roughness length traditionally defined by the Charnock relation

$$z_0 = 0.01 \frac{u_*^2}{g}$$

are shown in Figure 4 as well. The drag parameterisation in terms of the Charnock relation is widely used in different ocean and atmosphere studies. From the figure it is clear that the parameterisation considerably overestimates the drag coefficient and the friction velocity when the wind speed exceeds 33 m/s.

Makin[10] made an attempt to explain the reduction of the sea drag at hurricane wind speeds as a consequence of the sea spray. To that end, a resistance law of the sea surface at hurricane wind speeds was derived. At hurricane wind speeds sea spray droplets originating from actively breaking waves form a deep suspension layer above the sea surface. It is further assumed that a thin adjacent to the sea surface part of the suspension layer is characterized by a regime of limiting saturation. In this regime for the case of an unrestricted supply of droplets on the underlying surface, which is expected under hurricane winds, the airflow absorbs maximum possible amount of droplets for the given friction velocity. The description of the suspension layer in the regime of limiting saturation is based on the balance equation of the turbulent kinetic energy for an airflow with suspended particles, in this case sea spray droplets. Introducing an additional assumption that some droplet parameters in the regime of limiting saturation reach their critical value a reduction of the drag coefficient for the wind speed exceeding hurricane values of about 33 m/s is obtained in agreement with the experimental data. That is illustrated in Figure 4.

A new generation of geostationary satellites for meteorology

In January 2004 a new generation geostationary meteorological satellite became operational. The satellite named Meteosat Second Generation (MSG) is the first of a series for the coming decade. MSG observes the earth in twelve spectral channels, with a frequency of four times per hour and a sub satellite pixel resolution of 3 × 3 km², in one channel even 1 × 1 km². This is a significant improvement compared to previous geostationary satellite observing in three channels and producing two images per hour with a pixel resolution of 5 × 5 km² and 2.5 × 2.5 km². The extension of the spectral channels will enable new applications some of them yet unknown. At KNMI the satellite products are used in forecasting, observation research, climate research, and, NWP research and developments.

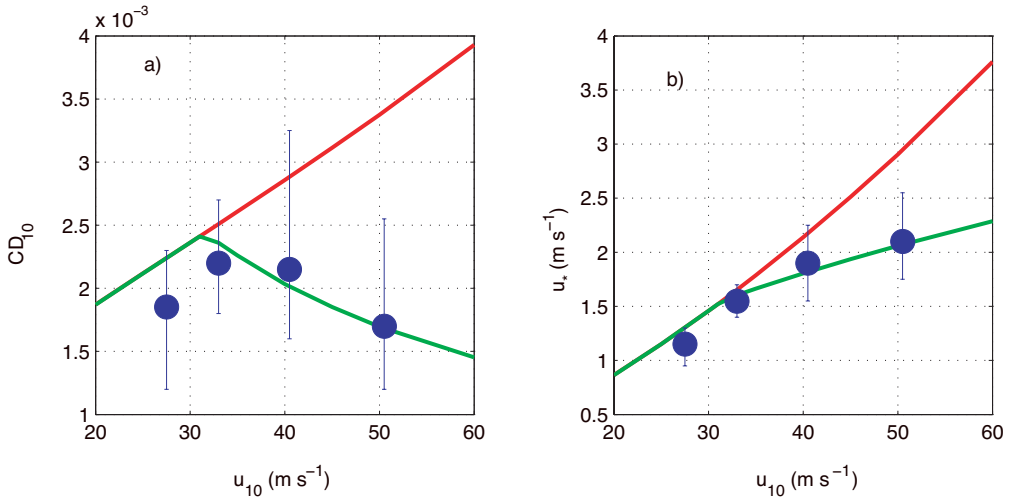

Figure 4. Drag coefficient (a) and friction velocity (b) versus wind speed. Solid line, according to Makin (2005) [10]; dashed line, according to Charnock relation; open circles, data by Powell et al. (2003) [9].

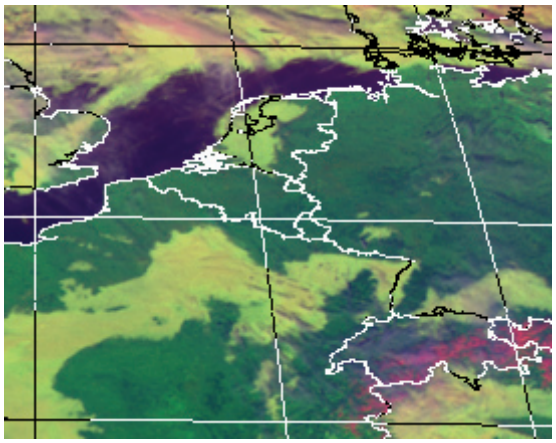

Figure 5. Fog detection over the Netherlands and Northern France by METEOSAT 8 on November 25, 12:00 GMT. The combination of the reflectance channels at 0.6 and 1.6 micron combined with the infrared radiation channel at 10.8 micron enables the differentiation between fog/low stratus, (in yellow) high clouds, (in pink) snow, (in reddish pink) and cirrus (blue/white).

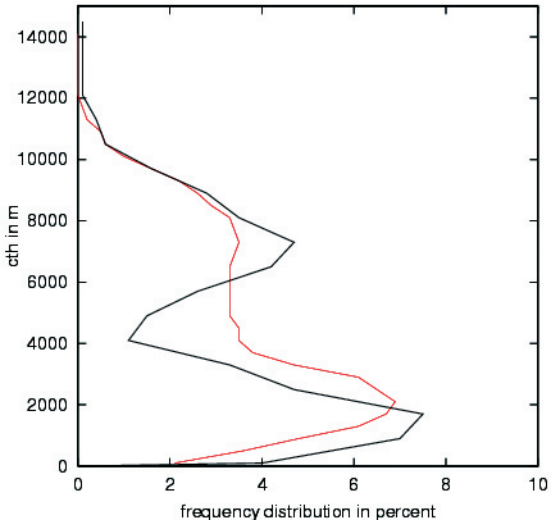

Figure 6. Comparison of cloud top height (cth) determination based on METEOSAT 8 imagery (red line) and MODIS imagery (black line) for September 2003.

Satellite Application Facilities

The European Meteorological Satellite Organization (EUMETSAT) set up so-called Satellite Application Facilities (SAF)[11] in collaboration with national meteorological services (NMS). A number of different SAF products can be directly used by the NMS. For operational use KNMI will concentrate on the products of the SAF on nowcasting and short range forecasting[12], like Rapid Developing Thunderstorms and the ability to distinguish fog and low stratus from other types of cloudiness.

The products of the SAF on nowcasting and short range forecasting need to be validated. KNMI concentrates on validation studies as part of the CLOUDMAP2[13] EC funded project and by other validation studies. In CLOUDMAP2 various cloud products from different satellite sensors and ground based remote sensors were compared to each other. An example is given in Figure 5.

Cinesat

In order to fully exploit the information content of the imagery KNMI acquired a CINESAT[14] software system. This system enables a quick display, re-projection, and, combination and manipulation of the spectral channels. The latter option allows a clear distinction of fog and low stratus, e.g. in Figure 6. By comparison of sequential series of imagery the developments and movements of atmospheric phenomena, like convective clouds can be tracked and forecasted.

Outlook

Research on the applications of the new METEOSAT 8 only recently started. The heritage of the previous satellite program shows that a large number of new applications can be expected. KNMI will continue its efforts in validation studies of the various products and will contribute in the development of new products and applications. A new field will be the synergy of various remote sensors on satellite and ground based like radar and lidar.

Probabilistic forecasting of (severe) thunderstorms

In the INDECS (Indices for Extreme Convective Situations) project the technique of Model Output Statistics (MOS[15]) has been used to derive logistic regression[13] equations for the (conditional) probability of (severe) thunderstorms in the warm half-year (from mid-April to mid-October) in the Netherlands[16]. For 12 regions of about 90 x 80 km^2 each and for projections out to 48 hours in advance (with 6-hour periods), we have developed these equations using combined (post-processed) output from the HIRLAM and ECMWF models as the potential predictor dataset. The predictands are derived from the SAFIR[17] lightning data, being either the probability of a thunderstorm (≥2 discharges) or the conditional probability of a severe thunderstorm (≥500 discharges) under the condition that ≥2 discharges will be detected.

The most important predictor in the thunderstorm forecast system is the square root of the ECMWF 6-h

Figure 7. (a) +12h (absolute) probability forecast of severe thunderstorms (%) for 15-21 UTC on July 17 2004. This forecast is based on the 06 UTC run of the MOS system. (b) Location of all lightning discharges (dots), as detected by the SAFIR network, during the same period. In every region more than 500 discharges were detected.

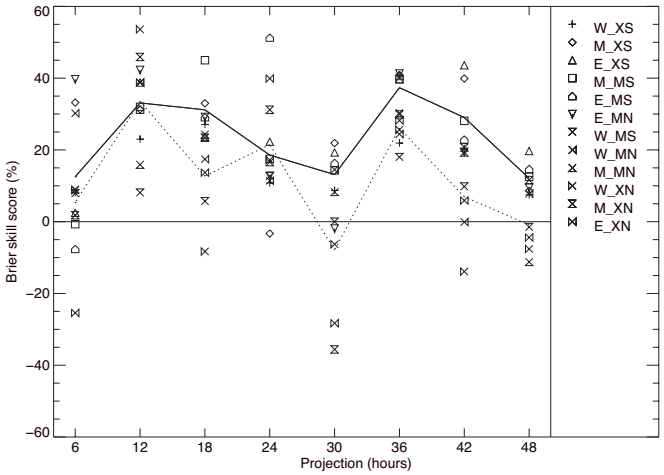

Figure 8a. Brier skill score (BSS)[13] with respect to the 1999-2001 climatology, as a function of projection for the 00 UTC run of the MOS thunderstorm forecast system for all 12 regions (indicated by the different symbols). The solid (dotted) line represents the average BSS for the 6 land (coastal) regions[16].

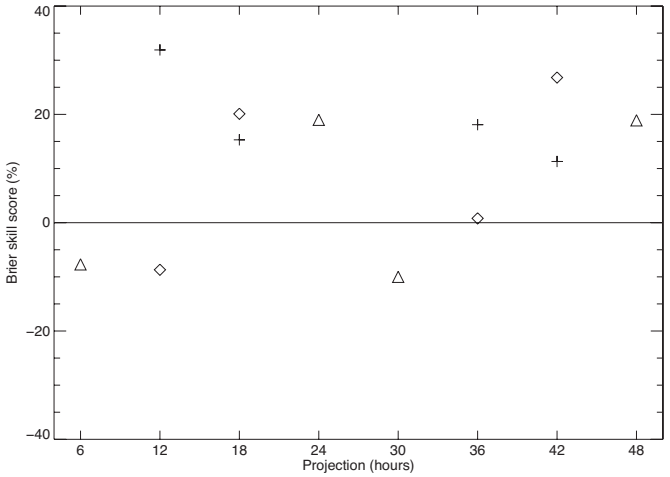

Figure 8b. Same as (a), but for the 00 UTC run of the MOS severe thunderstorm forecast system for the 6 pooled land regions (pluses), for the 6 pooled coastal regions (diamonds), and for all 12 pooled regions (triangles). The verification period is from 19 May - 7 October 2003.

convective precipitation sum, and the most important predictor in the severe thunderstorm forecast system is the Boyden index, computed from the HIRLAM forecasts[16]. Figure 7a shows an example of a probabilistic forecast of severe thunderstorms and Figure 7b shows the detected discharges. Of course, (probability) forecasts cannot be verified using only one case, so we present objective verification results for the (independent) warm season of 2003. We can conclude from these results (Figure 8) that the overall skill of the 00 UTC run of the MOS (severe) thunderstorm forecast system is good. The thunderstorm forecast system (Figure 8a) shows the best skill for the afternoon (09-15 UTC; +12h and +36h forecasts), for the

evening (15-21 UTC; +18h and +42h forecasts) and for the first night (21-03 UTC; +24h forecasts). The severe thunderstorm forecast system (Figure 8b) shows the best skill for the afternoon in the land regions, and for the evening and night in all regions.

As the overall verification results for the 06, 12 and 18 UTC runs of the MOS (severe) thunderstorm forecast system are also good, the system was made operational at KNMI in April 2004. However, the system shows (slight) overforecasting (not shown), presumably as a result of the increase in HIRLAM resolution in the beginning of 2002[16]. This can be eliminated by calibration or by updating the regression coefficients when more data from the high-resolution HIRLAM are included.

Finally, future developments in our MOS system may be an increase in the spatial resolution (dependent on projection), an increase in the temporal resolution from 6 to 3 hours, and an even more extreme criterion for severe thunderstorms together with the inclusion of advected observations (from radar, SAFIR and possibly MSG) as potential predictor sets for the 0-12h projections.

Warning system of extreme precipitation amounts for the Dutch Water Boards

In cooperation with the Union of Water Boards an automated warning system has been developed aiming at providing optimal meteorological information in cases of risks of flooding. Large economic losses may arise due to large amounts of precipitation in short periods of time that exceed the containment capabilities of the Water Board. The critical amount depends, among other things, on the geography and the pumping capacity of the particular Water Board, the recent precipitation history, but also on the time of year. Depending on the probability of exceeding this critical precipitation amount (which is different for each of the Water Boards) the water manager may take precautionary actions. This probability threshold

Figure 9. Location of the 12 participating Water Boards.

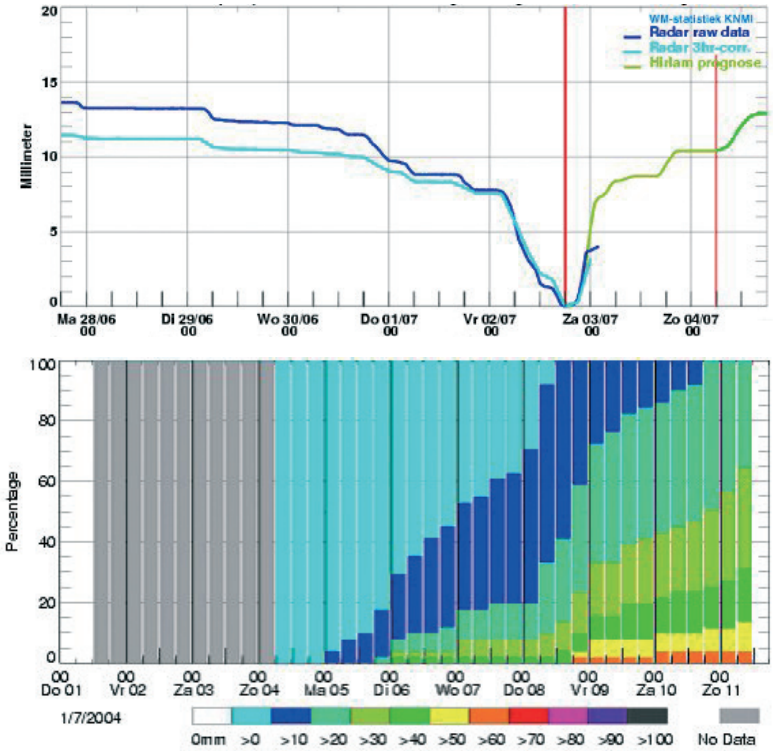

Figure 10. Example of the graphical presentation of the warning system issued at 02UTC 3 July 2004. It shows a 36-hour deterministic forecast of the Hirlam operational model (top panel) (in green) and a probabilistic forecast obtained from EPS (bottom panel). Also the 5-day history of observed area averaged precipitation is given (in blue) in the top panel (with time running backwards). The first few hours of the Hirlam forecast are replaced by radar observations. The corrected radar data are also given (in lighter blue).

depends on the costs of these measures with respect to the expected losses that are incurred when no actions would be taken (a so-called cost-loss analysis).

At the moment 12 of the 37 Dutch Water Boards participate in the project (Figure 9). They have specified a number of combinations of critical precipitation amounts over particular periods and the corresponding probability thresholds. The Water Board is warned automatically whenever the predicted probability of exceeding the critical amount is higher than the threshold probability.

The warning system covers a 14-day period consisting of a 5-day rainfall history and a 9-day forecast of area-averaged precipitation. The history is determined from weather radar reflections[18], not from station observations. The first 36 hours of the forecast are based on the deterministic output of the Hirlam model, which runs 4 times a day. No probabilistic information for this range is available yet. For the remaining part of the forecast range probabilistic output is derived from the Ensemble Prediction System (EPS) of the ECMWF, which is used once a day. The first few hours of the Hirlam forecast are substituted by the already available radar observations. The warning system is updated every hour. An example of the graphical presentation of the system is given in Figure 10.

The system is operational since December 2003. The results so far indicate that the warnings are a helpful additional tool in the decision making process of the Water Boards[19]. However, in some cases the precipitation derived from radar data only shows serious shortcomings. In the near future we plan to implement a correction algorithm, which incorporates the station observations[18]. A longer-term prospect is the development of a technique to obtain probabilistic information on the short range. This will further enhance the benefits of the system for the Water Boards.

The 1953 storm surge revisited

On the occasion of the 50-year remembrance of the disastrous storm surge of 1953 the question arose how present-day forecasting tools would have performed on that situation. One of the reasons that the disaster took so many lives was that the warning period was short and the surge took place in a weekend when most of the authorities dealing with public safety could not be reached anymore when the scale of the event became clear to forecasters.

The Reanalysis/Reforecasting projects of NCEP/NCAR[20] and ECMWF[21] made it possible to investigate this question further. With the observations that were collected by NCEP/NCAR for the period, ECMWF was able to rerun the global model and also the EPS system, however on a more coarse resolution than the current operational system. With all these data available, it became also feasible to run Hirlam and the WAQUA/DCSM98 storm surge model, in the configurations as they are used for day-to-day weather and sea level forecasts at KNMI.

The storm surge forecast based on the Hirlam run of Friday 30 Jan 1953 06:00 UTC is the first in which the highest high tide in Vlissingen on Sunday 1 Feb occurs. The forecast, although still lower than observed, already exceeds the (present) alarm level. This signal is confirmed by the later runs, which eventually overestimate the highest water level somewhat. Figure 11 shows the water level from WAQUA/DCSM98, and the wind and sea level pressure from Hirlam for Sunday 1 Feb 1953 3:00 UTC for the +45h and +3h forecasts.

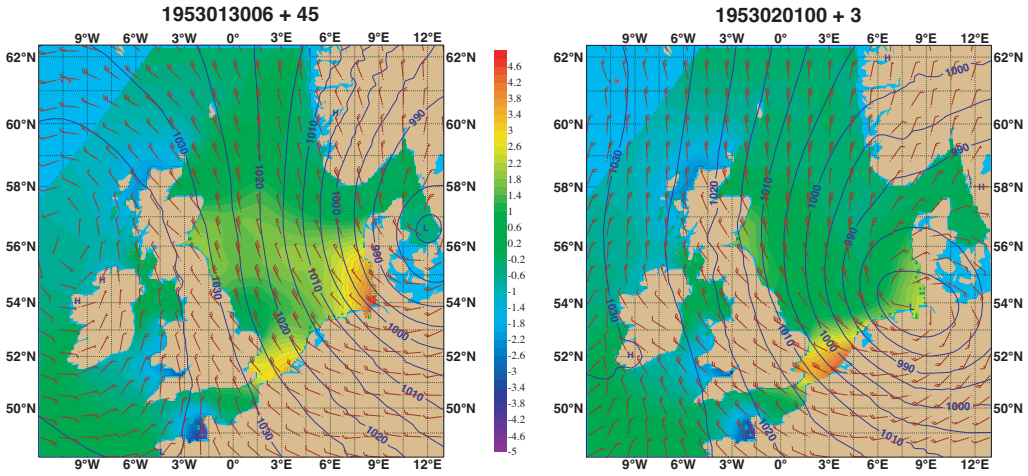

Figure 11. Hirlam wind and pressure [hPa] and WAQUA/DCSM98 water level [m] for 1 Feb 1953 3:00 UTC, forecast +45 and +3 hours ahead.

In operational practice, storm surge forecasts do not go beyond +48h and the information from the ECMWF EPS is also not yet being used. Only recently a project has started to validate medium range WAQUA/DCSM98 storm surge forecasts on ECMWF input and to generate calibrated probability forecasts for water levels. This case, however, gave a good opportunity to test the value of such forecasts. The WAQUA/DCSM98 model was run with as input the deterministic ECMWF model and also with the 50 members from the EPS. Starting with the run based on the analysis of Thursday 29 Jan 12:00 UTC, which would have been available early on Friday morning, there is a clear indication that the alarm level will be reached or exceeded in Vlissingen on the highest and also the following high tide. Figure 12 shows the water level time series in Vlissingen for these runs.

Hence, even with the limited amount of observations available for 1953 compared with the present situation, the storm surge was clearly present in both the WAQUA/DCSM98 storm surge forecasts based on Hirlam and on ECMWF, which would have been available on Friday morning. This would have given the forecasters ample time to issue warnings to the authorities who could have taken measures to limit the loss of life and the damage.

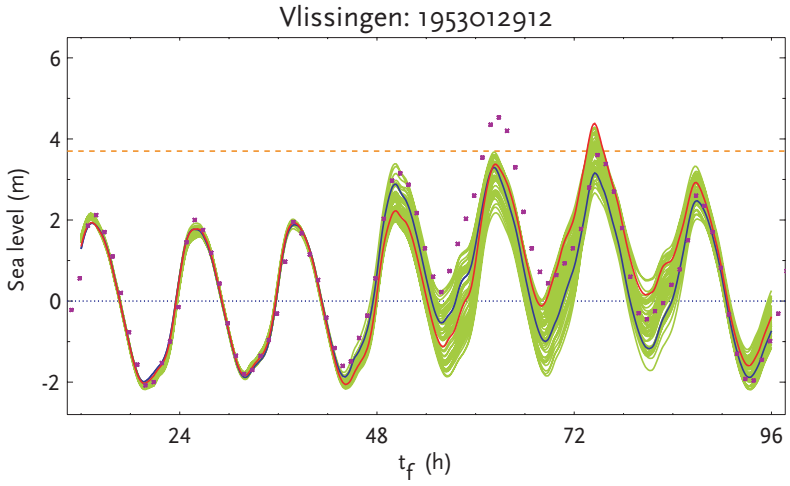

Figure 12. WAQUA/DCSM98-ECMWF forecasts for the water level in Vlissingen: deterministic (red), EPS (green and blue), observations (dots) and the current alarm level (orange).

1) Holleman, I. and H. Beekhuis, 2003. *Analysis and Correction of Dual-PRF Velocity Data.* J. Atmos. Oceanic Technol., **20**, 443-453.
2) Holleman, I., 2003. *Doppler Radar Wind Profiles.* KNMI Scientific Report, WR-2003-02.
3) Wieringa, J., 1976. *An objective exposure correction method for averaged wind speeds measured in a sheltered location*. Quart. J. Roy. Meteor.Soc., **112**, 867-889.
4) Ivens, R.A.A.M, 1987. *Forecasting the maximum wind velocity in squalls.* Proceedings Symp. Mesoscale Analysis & Forecasting, Vancouver, Canada, ESA SP-282.
5) Beljaars, A.C.M., 1983. *De invloed van meetsystemen op de waarneming van gemiddelden, standaarddeviaties en maxima.* KNMI Scientific Report WR-83-2.
6) Cuxart, J., P. Bougeault and J.L. Redelsberger, 2000. *A turbulence scheme allowing for mesoscale and large-eddy simulations.* Quart. J. Roy. Meteor. Soc., **126**, 1-30.
7) Tijm, A.B.C., 2004. *Tuning CBR.* HIRLAM Newsletter **46**, 18-28.
8) Tijm, A.B.C., 2004. *HIRLAM pseudo satellite images.* HIRLAM Newsletter **46**, 59-64.
9) Powell, M.D., P.J. Vickery and T.A. Reinhold, 2003. *Reduced drag coefficient for high wind speeds in tropical cyclones.* Nature, **422**, 279-283.
10. Makin, V.K., 2005. *A note on the drag of the sea surface at hurricane winds.* Bound.-Layer Meteor. **115(1)**, 169-176.
11) EUMETSAT: www.eumetsat.de 'programmes under development' 'safs'
12) safnwc: *www.nwcsaf.inm.es*
13) CLOUDMAP2 : *www.cloudmap.org*
14) cinesat: *www.cinesat.com*
15) Wilks, D.S., 1995. *Statistical methods in the atmospheric sciences: an introduction.* Academic Press, San Diego/London, ISBN 0-12-751965-3, 467 pp.
16) Schmeits, M.J., C.J. Kok and D.H.P. Vogelezang, 2005. *Probabilistic forecasting of (severe) thunderstorms in the Netherlands using model output statistics.* Wea. Forecasting, **20**, 134-148.

17) Wessels, H.R.A., 1998. *Evaluation of a radio interferometry lightning positioning system.* KNMI Scientific Report WR-98-04.
18. Holleman, I., 2003. *Neerslaganalyse uit radar- en stationswaarnemingen.* KNMI Intern Rapport IR 2003-06 (in Dutch).
19. Kok, C. J., D. H. P. Vogelezang, B. Wichers Schreur and I. Holleman. *Beschrijving van het automatisch waarschuwingssysteem voor extreme neerslaghoeveelheden t.b.v. de waterschappen* (in Dutch). In preparation.
20. Van den Dool, H.M., R.E. Kistler, S. Saha and J.F. den Tonkelaar, 2003. *Reanalysis and Reforecast of the Jan 31 - Feb 1 1953 North Sea Gale.* (*http://www.knmi.nl/voorl/nader/watersnood53vandendool.pdf*)
21. Jung, T., E. Klinker and S. Uppala, 2003. *Reanalysis and reforecast of three major European storms of the 20th century using the ECMWF forecasting system*, November 2003. (*http://www.ecmwf.int/publications/library/ecpublications/_pdf/era40/ERA40_PRS_10.pdf*)

The Numerical Weather Prediction development chain

Jan Barkmeijer, Hans Bonekamp, Siebren de Haan, Gert-Jan Marseille, Jeanette Onvlee, Ad Stoffelen, Sander Tijm, John de Vries and Ben Wichers Schreur

Introduction

Weather forecasts from numerical weather prediction (NWP) models effectively are the end result of a chain of activities. This chain begins with the design of future observing systems, continues with existing observation systems and the manner in which they are used in an NWP model, and ends with the numerical forecast model itself. The best way to consistently enhance the quality of NWP forecasts is to bring about improvements in each of the key elements of this chain. Research in the field of NWP at KNMI has therefore focussed on aspects of all these key elements. To illustrate the advances made in recent years, examples of research activities are presented which, taken together, highlight the NWP chain from start to end:

- Studies of the impact of future observing systems on NWP forecast models: sensitivity observation simulation experiments on the impact of future Doppler wind lidar observations
- Studies of the impact of available new observing systems on NWP models: humidity observations from ground-based Global Positioning System (GPS) receivers
- Adapting the products of existing observing systems to the changing demands of NWP models: development of a high-resolution satellite wind product suitable as input for detailed NWP models
- Improving data assimilation and initialisation in NWP models: The introduction of a 3D-Var scheme and the launching DFI initialisation method in HIRLAM
- Improving the NWP forecast model itself: advances in the HIRLAM model physics.

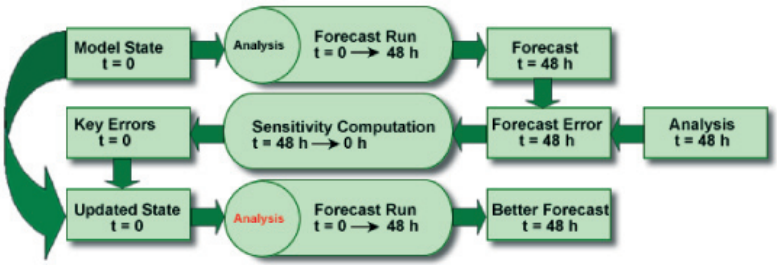

Figure 1. Background state sensitivity experiment. The updated analysis (red) provides the SOSE pseudo truth.

Future observing system impact assessment for real extreme cases

To minimize the occurrence of serious forecast failures in situations of extreme weather events with large socio-economic impact is of critical importance to operational meteorology. It is therefore of great interest to test future meteorological observing systems a priori on their ability to reduce the probability of such forecast failures, which would make them a cost-effective investment. Lacking an established methodology to test the impact of simulated observations in real atmospheric cases, we developed such a method[1] in the context of the ADM-Aeolus mission[2] as represented in Figure 1.
The Sensitivity Observing System Experiment, SOSE, uses so-called sensitivity structures to define a pseudo truth that

- improves the 2-day forecast,
- has realistic spatial structures, and
- is compatible with the existing (real) observations.

This pseudo truth is subsequently used for the simulation of the future observing system under investigation. Obviously, when the new observing system is capable of partly observing the key analysis errors, it will contribute to improve the 2-day forecast.

Sensitivity computations are daily performed at ECMWF. As one might expect, it is found that the resulting key analysis errors are largest over data-sparse areas exhibiting substantial atmospheric dynamics, notably over oceanic and tropical regions[3]. These are precisely the regions where future observing systems may contribute most. However, it turns out that the computed key analysis errors conflict with observations at the initial time (t=0) [4], as no constraint is used to prevent this. This conflict is most acute in observation-rich areas where the computed key analysis errors appear to be not so realistic. We developed a constraint to force compatibility with observations by using the sensitivity computation to provide key background model state errors. The updated background state is subsequently used in the analysis, where it is merged with the observations at initial time, thereby forcing compatibility with these observations.

In our OSSE[5] environment tests, indeed the pseudo truth thus constructed, i.e. the updated analysis, lies

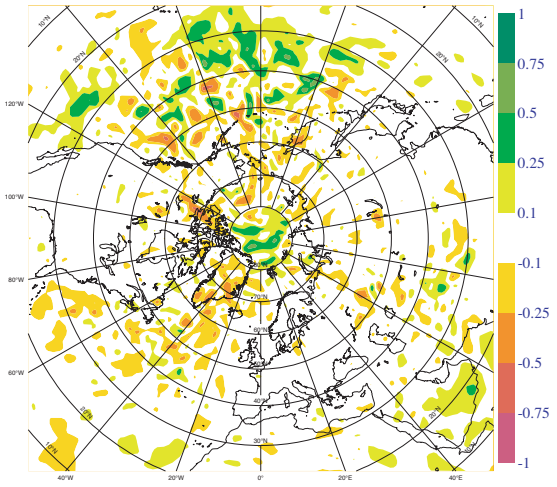

Figure 2. Mean analysis improvement [m/s] brought by the sensitivity-based analysis updates that improve the 2-day forecasts and are compatible with existing observations.

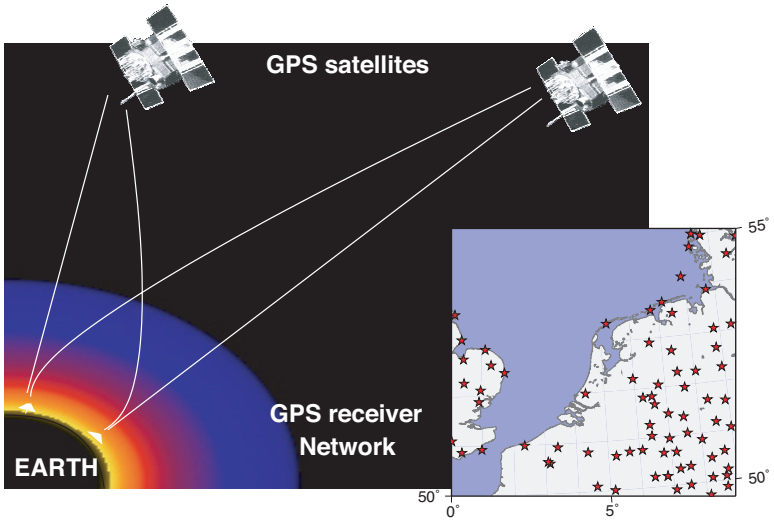

Figure 3. The GPS constellation consists of 24 satellites, a network of receivers and a processing centre, where the data is processed to estimate (amongst other parameters) the atmospheric delay of the signal. The satellite configuration is such that at any place on earth at least 4 satellites are above the horizon.

In order to consistently enhance the quality of NWP forecasts, it is essential to improve each of the elements of the NWP chain

closer to the true atmosphere than was the case with conventional key analysis errors (Figure 2). Although the observations used in the analysis with the updated background state do reduce forecast improvement, the updates in data-sparse regions remain substantial and result in significant 2-day forecast error reduction. As such, the method can be used to study the NWP impact of ADM-Aeolus and other future observing systems.

The effect of ground-based GPS humidity observations on NWP models

Humidity is highly variable in space and time and plays an important role in many atmospheric processes like cloud formation and precipitation. Humidity analysis and forecasting in numerical weather prediction has always suffered from lack of sufficient observations on relevant temporal and spatial scales. The Global Positioning System (GPS) can improve our ability to measure humidity indirectly with high temporal resolution and a spatial resolution better than that of the existing radiosonde network.

Carrier phase measurements from a network of ground-based GPS receivers can be processed into Tropospheric Slant Delay (TSD), Zenith Total Delay (ZTD) or Integrated Water Vapour (IWV) observations (see Figure 3). Tropospheric delay represents the propagation delay of a received microwave carrier signal from a GPS satellite due to refraction in the neutral atmosphere. The relation between refraction and humidity is well known[6].

From 1999 to 2004 the COST-716 action[7] investigated the exploitation of ground-based GPS for climate and NWP applications. Several European geodetic processing centres demonstrated that near-real-time availability of good quality GPS data is feasible within 1h45m. KNMI hosted a monitoring site showing IWV and ZTD time series from GPS and HIRLAM for 480 sites[8]. The time series can be used for NWP model validation and nowcasting of the vertical humidity distribution[9].

In the THROUGH project, humidity information from GPS slant observations has been assessed.
A standalone assimilation system was employed to analyse the atmospheric state using GPS observations only. The high temporal resolution of GPS slants is exploited by using the water vapour field retrieved from the previous hour as background in the assimilation. The 100km horizontal resolution of the receiver network proved insufficient to resolve small-scale humidity structures[10].

In the EU-FP5 project TOUGH, methods are being developed for the assimilation of TSDs in HIRLAM. Validation of TSD observations at 30s intervals has revealed that nonisotropic TSDs, which are alleged to contain small-scale humidity information, show little coherence with those computed from HIRLAM model fields and have a low signal-to-noise ratio (SNR). Averaging the data to 5-minute intervals proved a good compromise to improve the SNR while preserving the instantaneous character of TSDs. Coherence remained unchanged however.

High-resolution humidity observations from a dense GPS network can all originate from the same air mass. This is expected to result in observation errors being spatially correlated. To describe the correlated nature of TSD observation errors, a statistical covariance model has been constructed (Figure 4) that will be used in forthcoming impact studies together with the results of the validation. It is expected that small-scale humidity information may be beneficial in specific cases[11].

High-resolution satellite observations for NWP

Ever-increasing computing resources allow fast progress in NWP. More sophisticated data assimilation schemes such as 4D-Var become feasible on ever denser grids. However, analysis of weather on the small scales of present NWP models is limited by the observing system, which lags behind in its capability to resolve small-scale features. On current grid scales, wind observations over sea in particular are lacking[12].

In the context of the EUMETSAT Satellite Application Facilities (SAF) KNMI is responsible for scatterometer processing software and wind products[12]. Currently, a 100-km SeaWinds and a 50-km resolution ERS-2 scatterometer wind product are available operationally. Research has focussed on the development of a 25-km SeaWinds product. Scatterometer wind retrieval is ambiguous and multiple wind vector solutions are provided[13]. Moreover, geophysical noise in SeaWinds observations, notably due to rain, causes rather arbitrary local minima after wind retrieval. In fact, the more noise in the measurements, the more ambiguous and undetermined the wind retrieval. This provides little hope for higher resolution products, since these can only be achieved at the expense of more (geophysical) noise. The current operational product from NOAA is at 25 km but wind retrieval errors are suppressed by a spatial filter[14] that basically forces continuity on the wind direction field[13]. In NWP analyses, spatial filtering is performed using balance constraints, i.e., forcing rotation and small divergence at higher latitudes. As such, KNMI applies a 2D-Var[15] in the scatterometer wind processing for advanced wind field analyses. Recently we applied 2D-Var in combination with an extended output from the wind inversion, in which the a priori probability of each wind solution is defined. This method provides an improved 100-km wind product[13] and provides realistic information on sub synoptic scales at 25 km (Figure 5). Further tests[16] will allow tuning of the meteorological balance constraints and refined quality control of the input scatterometer winds at 25-km resolution. The 2D-Var method may equally well be applied in more complete 3D-Var or 4D-Var analyses.

HIRLAM data assimilation and initialisation

3D-Var

With the release of HIRLAM model version 6.0.0 in March 2003, three-dimensional variational (3D-Var)

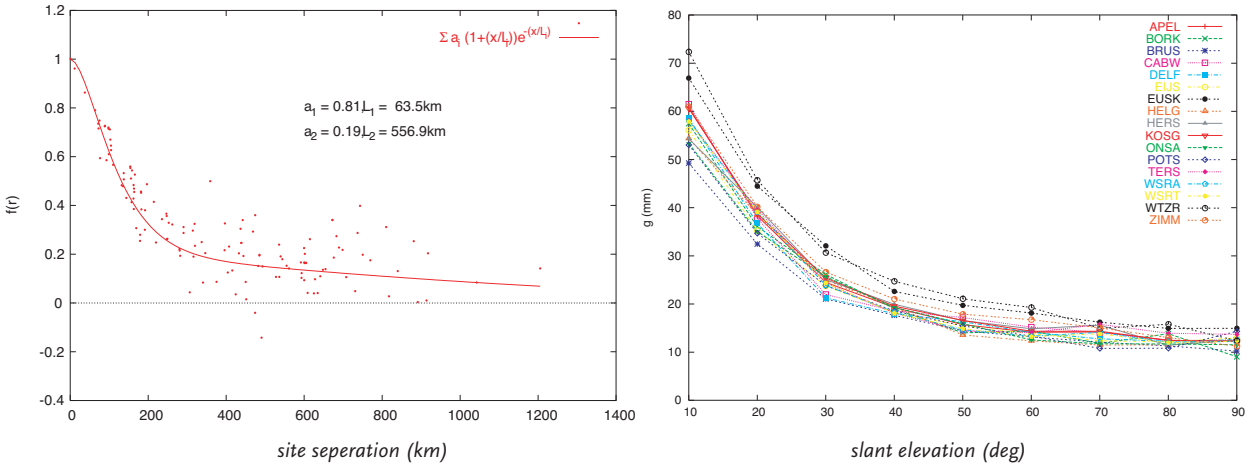

Figure 4. Component functions of the two-point observation error covariance model, with error correlation function (left panel) depending on receiver site separation and site-specific standard deviation of the error (right panel) depending on slant elevation angle.

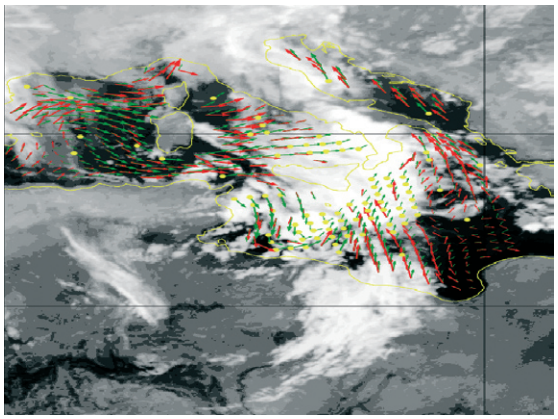

Figure 5. SeaWinds 2D-Var wind field in the Mediterranean (red arrows), showing inflow in a convective system south of Sicily. For comparison NWP 1000-mb winds are shown originating from NCEP (green arrows).

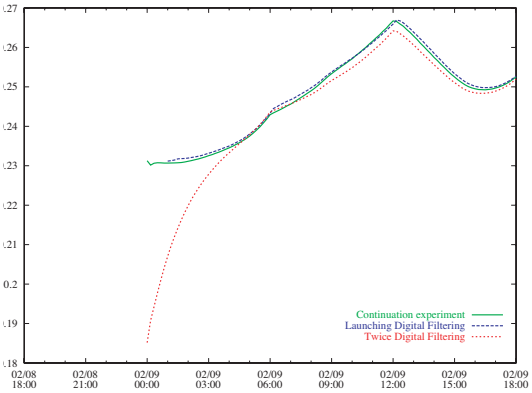

Figure 6. The backward integration in normal DFI (red) causes a spin-up in momentum flux (MOMF) as compared to the true model evolution (green). Initialisation with launching DFI (blue) eliminates this spin-up.

data assimilation[17] has replaced optimal interpolation as the reference data assimilation scheme. The 3D-Var scheme was implemented on KNMI SUN hardware and introduced into operations at KNMI with HIRLAM version 6.2.4. in June 2004.

Even while there has been no direct meteorological benefit from the introduction of 3D-Var it is considered to be a major step forward in data assimilation. It allows KNMI to use HIRLAM as a testbed for the development of observation operators for new data types and to contribute to and benefit from developments in this area by the international NWP community. It will thus speed up the introduction of new data types into operation.

The 3D-Var scheme also allows for other forms of manipulation of initial conditions, such as those that are the basis for short-range ensemble predictions or the interactive modification of model initial conditions by forecasters. Verkley et al. [18]) demonstrated how the HIRLAM 3D-Var system may be used to adjust a model state, including the analysis, after manual adjustment of the potential vorticity field. Their method is based on the correlation of the potential vorticity field with satellite water vapour imagery. The modified potential vorticity is assimilated by replacing the observation term in the cost function of 3D-Var by a potential vorticity term.

Launching DFI

For mesoscale models with resolutions better than 20 km, normal mode initialisation is not a valid method of initialisation. In HIRLAM it has been replaced by digital filter initialisation (DFI)[19]. This method is applicable to any model resolution and filters the complete model state. A drawback is that it requires an adiabatic backward integration of the model. This causes an unbalance between model dynamics and physics, resulting in an initial spin-up of the model parameters and wavelike disturbances emanating from regions with strong baroclinic development. These disturbances are sufficiently large to be noted by forecasters.

In response to criticisms of duty forecasters, the launching DFI method was developed at KNMI. In this method only the first two hours of the forward model integration are filtered to their midpoint. The forecast is then started from the initialised model state at analysis time plus one hour. This method achieves a comparable result as the incremental DFI method that is part of the HIRLAM reference system, but at a much lower computational cost. The method is effective in reducing model spin-up (see Figure 6), which is of importance now that the focus is shifting towards more frequent analyses and high resolution modelling for the nowcasting range.

Changes in HIRLAM model physics

Long standing problems in the HIRLAM weather forecast model have been a strong positive bias in the wind speed and wind direction, together with a negative bias in the surface pressure during winter at higher latitudes. The negative surface pressure bias is due to the fact that the ageostrophic flow is not strong enough, which results in the too slow filling of low-pressure systems. This pressure bias is not present in summer because the lows are less active then. From a comparison with Cabauw observations we

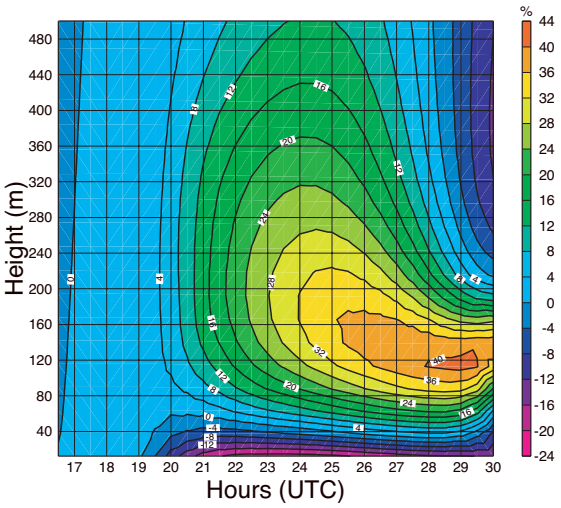

Figure 7. Wind speed difference (in %) as a function of time and height in a 1D experiment simulating summer nighttime conditions. The increase in wind speed above 50 meters (up to 40%) and the decrease closer to the surface during the night are caused by a decrease in mixing under stable conditions, enabling a much better representation of low-level wind speed.

learn that the positive wind speed and wind direction bias are caused by too strong mixing of momentum in the turbulence scheme. Improvement in one parameter (e.g. the reduction of the surface pressure bias) by changes in the physics have sofar always resulted in a deterioration in the other (the wind speed and direction biases).

In Tijm[20] a solution for this stalemate is proposed. He shows that a reduction of the surface stress in the ageostrophic direction, by a turning of the surface stress in the geostrophic direction, causes the ageostrophic winds to increase. Through the increase of the ageostrophic wind, the rate of filling of low-pressure systems is increased, causing a reduction of the surface pressure bias. This reduction causes smaller pressure gradients and also reduces the wind speed and wind direction biases. Therefore a single change in the physics causes improvement in the scores of surface pressure as well as those of wind speed and wind direction.

The ideas in Tijm[20] have been developed further by Sass and Nielsen[21], who make the rotation of the stress vector dependent on stability and roughness. Surface stress rotation also enables a reduction of the mixing of momentum under stable conditions. This reduction allows for a much better reproduction of the LES (large eddy simulation) results from the neutral/stable GABLS (GEWEX Atmospheric Boundary Layer Study) intercomparison study. It causes a large improvement in the profiles of wind and temperature close to the surface (see Tijm[22]). Figure 7 shows the relative difference in wind speed between the old and new turbulence schemes for a clear summer night. The adapted scheme enables the model to represent wind shear under stable conditions much better (e.g. in the case of low-level jets).

All changes described above have been introduced in the HIRLAM Reference System in 2004.

1) Marseille, G.J., A.Stoffelen and J. Barkmeijer. *The use of sensitivities to assess the added value of future space-borne Doppler wind lidars in extreme weather events.* Proc. 1st THORPEX International Science Symposium, 6-10/12/'04, Montréal, Canada, in press.
2) Stoffelen, A., P. Flamant, E. Källén, J. Pailleux, J.M. Vaughan, W. Wergen, E. Andersson, H. Schyberg, A. Culoma, M. Endemann, P. Ingmann and R. Meynart, 2005. *The Atmospheric Dynamics Mission for Global Wind Field Measurement.* Bull. Amer. Meteor. Soc., **86**, 73-87.
3) Marseille G.J. and F. Bouttier, 2001. *Climatologies of sensitive areas for short-term forecast errors over Europe*. ECMWF Research Department Techn. Memo 334.
4) Isaksen, L., M. Fisher and E. Andersson, 2005. *The structure and realism of sensitivity perturbations and their interpretations as 'Key Analysis Errors'*. Submitted to Quart.J.Roy. Meteor. Soc..
5) Marseille, G.J., A. Stoffelen, F. Bouttier, C. Cardinali, S. de Haan and D. Vasiljevic, 2001. *Impact assessment of a Doppler wind lidar in space on atmospheric analyses and numerical weather prediction.* KNMI Scientific Report WR-2001-03.

6) Thayer, G.D., 1974. *An improved equation for the radio refractive index of air.* Radio Sci., **9**, 803-807.
7) Elgered, G., H.-P. Plag, H. van der Marel, S. Barlag and J. Nash (Eds.), 2004. COST Action 716: *Exploitation of Ground-based GPS for Climate and Numerical Weather Prediction Applications.* Final Report, EU, Brussels (available at *http://www.oso.chalmers.se/~kge/cost716.html/*).
8) KNMI GPS water vapour monitoring web portal: *http://www.knmi.nl/samenw/cost716/*.
9) Haan, S. de, S.J.M. Barlag, H. Klein Baltink and F. Debie, 2004. *Synergetic use of GPS water vapour and meteosat images for synoptic weather forecasting.* J. Appl. Meteor., **43,** 514-518.
10) Haan, S. de and H. van der Marel. *Resolving spatial and temporal atmospheric water vapour structures using a ground-based GPS receiver network.* SRON report EO-050, in press.
11) Vries, J.C.W. de, 2005. *Validation and Error Modeling of Tropospheric Slant Delays.* Report on TOUGH Deliverable D37.
12) KNMI scatterometer web portal: *http://www.KNMI.nl/scatterometer/*.
13) Portabella, M., 2002. *Wind field retrieval from Satellite Radar Systems.* Barcelona University, Physics Department, ISBN 90-6464-499-3.
14) Leidner, M., R. Hoffman and J. Augenbaum, 2000. *SeaWinds scatterometer real-time BUFR geophysical data product, version 2.2.0.* NOAA/NESDIS, February 2000.
15) Vries, J.C.W. de and A. Stoffelen, 2000. *2D-VAR Ambiguity Removal.* Ocean and Sea Ice SAF Report, available from KNMI.
16) Stoffelen, A.C.M., S. de Haan, Y. Quilfen and H. Schyberg, 2002. *ERS Scatterometer Ambiguity Removal Scheme Comparison.* Ocean & Sea Ice SAF Report, available from KNMI.
17) Gustafsson, N., L. Berre, S. Hörnquist, X. Y. Huang, M. Lindskog, S. Navascués, K. S. Mogensen and S. Thornsteinsson, 2001. *Three-dimensional variational data assimilation for a high-resolution limited area model Part 1: General formulation and the background error constraint.* Tellus, **53A,** 425-446.
18) Verkley, W.T.M., P.W.C. Vosbeek and A.R. Moene. *Manually adjusting a numerical weather analysis in terms of potential vorticity using three-dimensional variational data-assimilation.* Quart.J.Roy. Meteor. Soc., in press.
19) Lynch, P. and X.Y. Huang, 1994. *Diabatic initialisation using recursive filters.* Tellus, **46A**, 583-597.
20) Tijm, A.B.C., 2003. *Different aspects of CBR.* HIRLAM Newsletter, **44**, p. 49-60.
21) Sass, B. H. and N. W. Nielsen, 2004. *Modelling of the HIRLAM surface stress direction.* HIRLAM newsletter **45**, 105-112.
22) Tijm, A.B.C., 2004. *Tuning CBR.* HIRLAM Newsletter, **46**, 18-28.

A modern strategic approach on the redesign of synoptical observations networks

Jitze van der Meulen

New developments in weather observations

By tradition in-situ measurements of the classic meteorological variables like temperature, pressure, wind, etc. are the backbone of the weather service. For more than a century these observations are carried out at weather stations, where skilled observers both perform instrument measurements and observe the various types of weather phenomena. Appropriate communications between weather stations worldwide enabled forecasters to inform on expected weather and the measurements were used to create weather maps. Typically, these maps were the basic source for any forecast.

During the last decades however, the introduction of (super-) computer technology and automatic measurement techniques has changed this traditional process significantly. Today computer simulation models describe the physical state of the atmosphere in all of its dynamics. The introduction of new, sophisticated observation technologies using these models has demonstrated high potential. This development is characterized by alternative technologies like active and passive remote sensing, from satellites or from the earth's surface. Moreover, the conventional instrument measurements and weather observations are fully automized using sophisticated optoelectronic sensor technologies, providing observational data in a digital format essential for input in computerized systems running dedicated applications.

These observations are performed automatically and unattended[1]. System control is done remotely at a service centre. Although this development is not welcomed by all disciplines in meteorology and in particular climatology, the synoptical meteorology experiences many advantages. Apart from automation of all types of in-situ observations, unattended data-acquisition, transport, processing and dissemination require an ultimate level of high performance processing systems. The architecture of such systems must be specified providing appropriate quality control, data management and maintenance facilities. Such data systems are successfully implemented in 2002 in the Netherlands[2]. Nevertheless, implementing the new techniques in the operational environment of forecasting services should be regarded as a great challenge.

Replacing human observations by automatic measurements has an impact on the performance of the observing system on the whole. Decrease of performance and quality is predicted when automizing a network and with a negative impact on the meteorological services as a consequence. In fact, the advantages of a uniform, fully automized and unattended observing networks prevail over the traditional situation provided that such a network is designed appropriately. There is not only advantage of more uniform observations without any subjectivity caused by human interpretation. Also data acquisition and dissemination is performed on a continuous and real time base. So instead of the one, three or six hourly reports, reports on the actual state of the atmosphere are available in real time. As a result the forecasted timing of upcoming (severe) weather phenomena is more accurate. Also rapid trends and changes in weather are registered and reported on line providing a more efficient weather information service.

Another advantage is the flexibility in appointing suitable locations for weather stations. For more than a century, such stations were chosen at sea shore locations, harbours, airfields, nearby buildings, etc. As a consequence poor and inadequate siting often resulted in low representativeness with regard to the surrounded area and distribution of these stations over the region of interest was not very homogeneous. Defining a new set of automatic weather stations for a synoptic network has become much easier and siting criteria are better met.

In the Netherlands, KNMI, the Royal Air Force and the Royal Navy organize the synoptical observing network together. In practice all stations are uniformly designed, so the observation techniques used in this network are identical for all locations. Therefore no special care has to be taken when designing the network, providing a relatively easy optimizing process. It turned out that after rearranging this network with fewer stations a better network homogeneity was established as well.

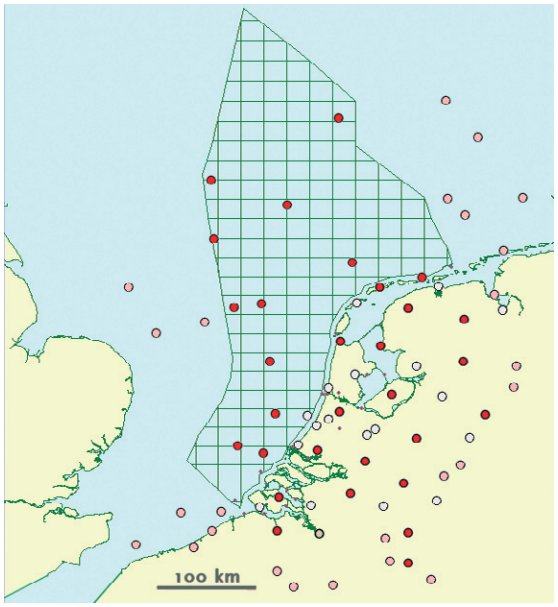

Figure 1. Synoptic Observations Network Netherlands 2005 (SWaNet-NL 2005)–design5): Red bullets (●): national synoptical stations, grey bullets (○): other national observing stations, pink bullets (◍): foreign stations, small red dots (•): additional wind mast.

R (%) distance d /km	5	10	15	20	25	30	35	40	45	50	55	60	65
Previous (N=20)	**3.2**	**12.6**	**26.8**	**43.3**	**60.2**	**74.3**	**84.5**	**91.4**	96.3	99.0	99.9	100-	100
Recommended (N=18)	**3.1**	**12.4**	**27.1**	**46.5**	**66.6**	**82.1**	**92.0**	97.4	99.5	99.9	100	100	100

Table 1. Network homogeneity parameter R represents the relative amount (in %) of all distances from every location in the Netherlands to a nearby station shorter than a certain fixed distance. For instance R(d=5 km) = 3.2% means that 3.2% of all location are at a distance of shorter than 5 km of any station. Clearly the distance at which 95% of all locations is close to a nearby station is reduced with about 5 km (from about 43 km to about 38 km).

Recent technological developments enable the design of more efficient automated networks

New functional design of a synoptic network

Nevertheless, the question of the density requirement itself has to be solved in the first place. In fact, such density dependents on the regional climate and all various meteorological variables require their own density. Typically, precipitation and wind require high density, while the density of a network of barometers may be quite low. Such density can be estimated on a simple way based on the prevailing wind or typical transport speeds of weather phenomena. A more sophisticated approach is based on statistical calculations of the covariance of the variable measured at the various locations assuming a sufficiently high correlation between these autonomous measurements. It is common experience that in practice the simple straightforward approach is sufficient. However, the latter approach, suggested in the leading WMO Guide on the Global Observing System[3], and its background reference 'The Planning of Meteorological Station Networks[4]' will result in inconsistencies, trivialities and undefined solutions and is therefore not suitable. Therefore, in the Netherlands the stated appropriate network density is based on prevailing wind speeds in combination with movement of fog and low-level clouds (about 25 km/h) and incoming fronts with showers with thunderstorms (about 50 km/h). Taking advantage of the real time functionality of the network, a spacing of about 50 km is found to be sufficient. Only for wind measurements a shorter distance is required (about 25 km) to meet the recommended correlation coefficient of 0.90 for two neighbouring stations. By placing some extra wind masts this requirement can be met in general. A network of precipitation measurements to measure daily amounts requires a small spacing of 15 km. This extreme requirement can only be met by using the ad-

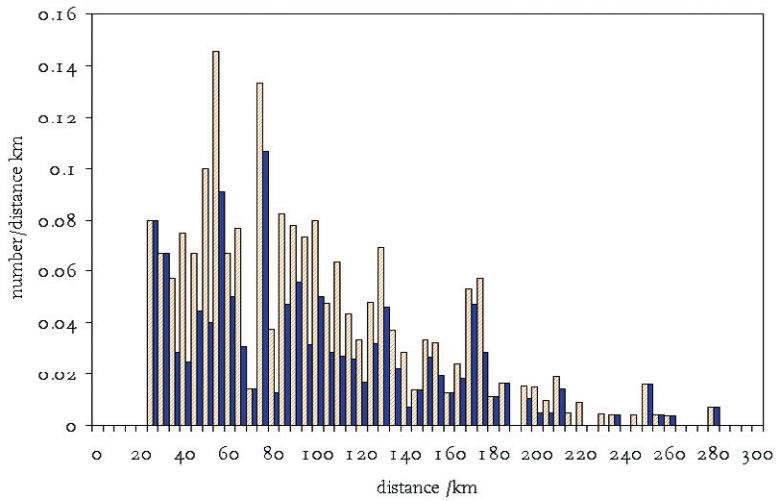

Figure 2. Clustered distributions for both the previous and the new design (////: previous, ■: new). The distributions represent all mutual distances between all stations, but normalized. Because the number of stations is reduced from 20 to 18, the total number of distances is smaller for the distribution representing the new design.

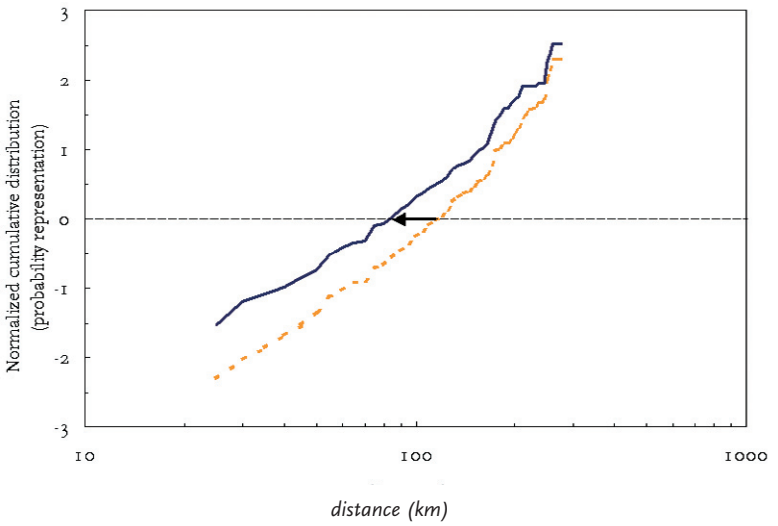

Figure 3. Cumulative representation of the normalized distributions shown in Figure 3 but in probability representation and with the distances on a logarithmic scale (dashed - - -: old, straight line —: new). Both distributions show a smooth behaviour indicating a sufficient high level of network homogeneity. Nevertheless, the new situation clearly indicates a distance improvement of about 25%.

ditional separate, autonomous network of 315 volunteering observers because a network with automatic gauges cannot be funded. Moreover the introduction of new precipitation radar systems will provide more redundancy. This solution has a great benefit because the high refreshment rate of radar systems provides an optimal real-time data source, extremely useful for synoptic practices.

Optimizing the meteorological station network

For an optimal network design the required level of homogeneity is the first constraint to be considered. Other relevant constraints are appropriate siting and representativity issues. A measure for the level of optimizing a network should be expressed best by a simple, well-defined single parameter. For a first order approximation such a parameter is chosen based on a statistical analysis of the distance between every position in the Netherlands and its nearby station. This parameter represents for instance the percentage of all locations on a distance larger than a certain distance from any station. It is found that with the new network design for the stations on land the 95% cumulative level will be between 35 and 40 km. In the previous situation with 20 land stations this distance was within 40 and 45 km (see Table 1). For the new network design[5] 99.9% of all positions on land are at a distance smaller than 50 km from a nearby station, fulfilling the requirement and providing sufficient redundancy. Over sea this requirement cannot be fulfilled due to the lack of suitable off shore locations (oil platforms), but a spacing of about 100 km should be acceptable for all practices (see Figure 1).

Other statistical techniques used for network design analysis are based on the mutual distances between all stations or between neighbouring stations only (e.g. sets of triangles of three neighbours). The latter technique is common practice to demonstrate the level of representativeness or the uncertainty of a derived interpolated variable valid for a location within such a triangle. However, for an overall impression of the homogeneity of a network, a statistical analysis of all mutual distances of the stations can be carried out. Optimizing the normalized (cumulative) distribution of these sets of distances is then the first target (distribution are normalized by dividing the number by the distance). In Figure 2 an example is given for two of such distributions, one for the previous set of stations on land an the other for the new design. From each distribution a cumulative distribution can be derived and showing in so-called probability representation will give an impression of the homogeneity. Figure 3 presents such a cumulative distribution as a function of distance, presented logarithmically. The figure shows a rather smooth and linear behaviour for both the past and the new situation. Although both lines are very comparable, an improvement (in terms of distances) is obtained by about 25%, a non-trivial and remarkable result because the number of stations is reduced by 10%.

1) Wauben, W., F. Kuik and T. Haig, 2002. *The New Meteorological Observation Network in The Netherlands*, WMO/TD-No. 1123, par. 1.1(6), WMO, Geneva, Switzerland, 4pp, available on CD-ROM
2) Wauben, W. and D. Hart. *The New Meteorological Observation Network in The Netherlands; Status and Operational Experience*. Submitted to WMO.
3) World Meteorological Organization, *Guide on the Global Observing System*. WMO - No. 488, WMO, Geneva, Switzerland, 191 pp.
4) Gandin, L.S., 1970. *The Planning of Meteorological Station Networks*. WMO-No. 265, TP. 149, WMO, Geneva, Switzerland, 35 pp.
5) Van der Meulen, J.P., 2005. *Synoptisch Waarneemnet Nederland 2005*. KNMI, De Bilt, the Netherlands, 23 pp. *www.knmi.nl/~meulenvd/projects/SwaNet2005*

Development of the KNMI Operational Data Centre (KODAC)

Maarten van der Hoeven, Ian van der Neut, Wim Som de Cerff, John van der Vegte, Michiel van Weele and Frans van der Wel

Introduction

KNMI provides weather, climate and seismological datasets to a varied group of customers. The number and size of the data volumes is increasing rapidly, with satellite data as important contributor. Currently, only part of the datasets are directly available via the Internet, although their number will grow given new (inter) national regulations that require easy and standardized access to a range of environmental data.

KODAC is the main strategy for the future spatial data infrastructure for all KNMI data, linking up with national and international efforts. It incorporates efficient data delivery to customers, both bulk data transfer and interactive data exploration and retrieval. For bulk data delivery, the Family of Operational Data Services (FORDS) will be developed. This chapter deals with the development of the interactive data search and retrieve part of KODAC.

KNMI has the disposal of several successful solutions for interactively searching and accessing datasets, but none of these systems can browse through all available datasets. A uniform and secure access to heterogeneous, distributed data sources improves the visibility of the KNMI data, and contributes to an optimal exploitation of available data. Customers can easily find datasets of interest and might even explore data they did not think of before.

KODAC benefits from knowledge and skills gained during the development of existing data retrieval systems (NL-SCIA-DC[1], TEMIS[2], ECA&D[3]). Information systems such as KODAC need to be accepted by and embedded in the entire organization. A phased approach is used to accomplish this. KODAC-1 is the first phase in which a working end-to-end system for one dataset will be implemented, demonstrating technical solutions and organizational benefits.

Users

Essential when building an information system is the correct translation from user demands and wishes into verifiable and specific user requirements. The users of the KODAC system can be divided into three groups: the end-users, the KNMI data providers and the system administrators. The group of end-users of KODAC is potentially very large and, in fact, includes all people interested in the interactive use of data from KNMI. As such KODAC will substantiate the open data policy of KNMI, in line with the KNMI law and EU regulations. Within KODAC the end-users are represented by the KNMI data providers as they are assumed to be in regular contact with the users of their datasets. One of the means that has been developed for direct interaction with the end-users is the organization of KODAC symposia.

An in-depth analysis[4] has been performed on the user requirements for KODAC by stakeholders from all user groups, together with the system developers. The document contains both functional requirements (e.g.,"KODAC shall present KNMI data as a unity from the end-users point of view") as well as non-functional requirements. The latter include, among others, the 'look-and-feel' requirements concerning the user interface (web-pages) in relation to the KNMI internetsite, the system usability (publish (upload), catalogue, browse, query, download, help, etc), as well as the system performance (e.g. peaks in data requests, number of concurrent users, waiting times, etc.).

The user requirements document has served as framework for the development of the prototype system of KODAC-1 and it provides a firm base for follow-up projects, even though information system requirements are not static. New insights may change requirements or priorities and new requirements may surface. In fact, flexibility to incorporate future user needs is one of the essential user requirements to the design of an information system like KODAC.

Architecture

The KODAC system needs to be able to retrieve data from a myriad of current and future sources. These can include tape archives, internal and external FTP and HTTP sites and so on. The KODAC architecture facilitates this by using flexible backend services feed the data products to the web frontend. By keeping properties (metadata) of the various data products in a database, the KODAC system can determine which backend service it needs to call on to obtain a requested data product. KODAC communicates with its backend services by using the SOAP (Simple

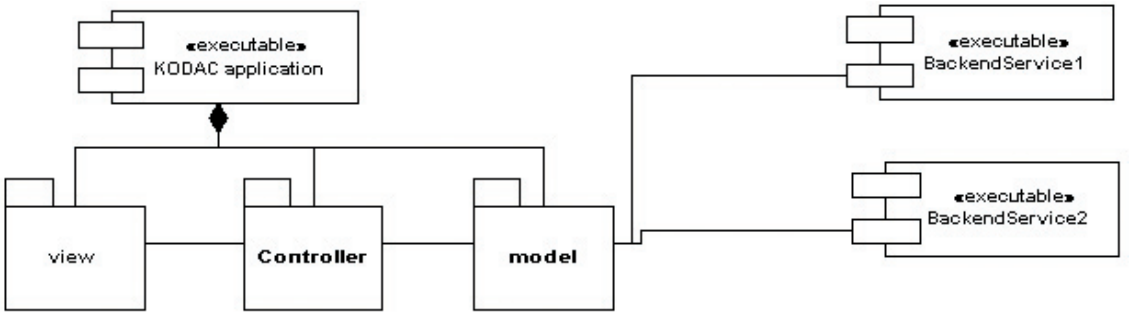

Figure 1. The architecture in the Unified Modeling Language (UML). The KODAC application interacts with the user through the 'view'. User requests are routed to the model by the controller. The model uses backend services that may reside on remote machines to fetch products.

KODAC is the main strategy for the future spatial data infrastructure for all KNMI data, linking up with national and international efforts

Object Access Protocol), also known as 'Web Services' protocol.

KODAC's frontend is built using the state of the art Java Enterprise paradigms to ensure maximum scalability and code maintainability. The Apache TOMCAT[7] application server and Apache Struts[8] web application framework are used to facilitate a modular application that can be expanded with new services as the need arises. Dynamic discovery of product specific webforms, product pages and backend services are implemented using proven Design Patterns.

The KODAC system follows the Model-View-Controller design pattern, which ensures that the model (actual application logic) can be separated from the view (user interface). The controller component routes user requests to the core application. The core application, after discovering the appropriate backend service and associated view, returns this data to the view component.

Metadata

Metadata is of the utmost importance for archiving and discovering datasets. The structured description of their characteristics should follow de jure standards such that search procedures can be formalized. At KNMI, the ISO-19115 metadata standard has been accepted for assessing the contents of the metadata database for the KODAC system. This is in accordance with developments within WMO and the European Union (Inspire[5]).

At first, core metadata will be collected at dataset level to answer questions concerning the 'what, where, when and who': what theme, what geographic coverage, which time span and who is the point of contact for more background information. It will require some discipline to describe all data according to a standard, but the advantage is an increased chance of 'findability' on the web: KODAC will offer than a collection of links to datasets.

Standardized metadata supports the idea of a service-oriented architecture in which dedicated metadata services are able to exchange information in a seamless way. This will be the basis for dedicated portals, like UNIDART[6]. As KODAC has aspirations to establish a Dutch node in an international framework, the ISO metadata is essential.

Implementation plans

To proof the conceptual design of KODAC EDOW (Electronisch Dag Overzicht Weer), which is the daily delivery of customized climatological reports to paying customers, is used as a pilot. Until recently, delivery of this daily reports takes places by using fax machines. Because of degraded hardware, and changing demands of the paying customers, a new approach is taken to deliver the daily report by means of account-based web access.

The KODAC pilot will provide core functionality as specified in the requirements. It will implement the core features and will take care of user authentication and authorisation, as well as presenting the custom-

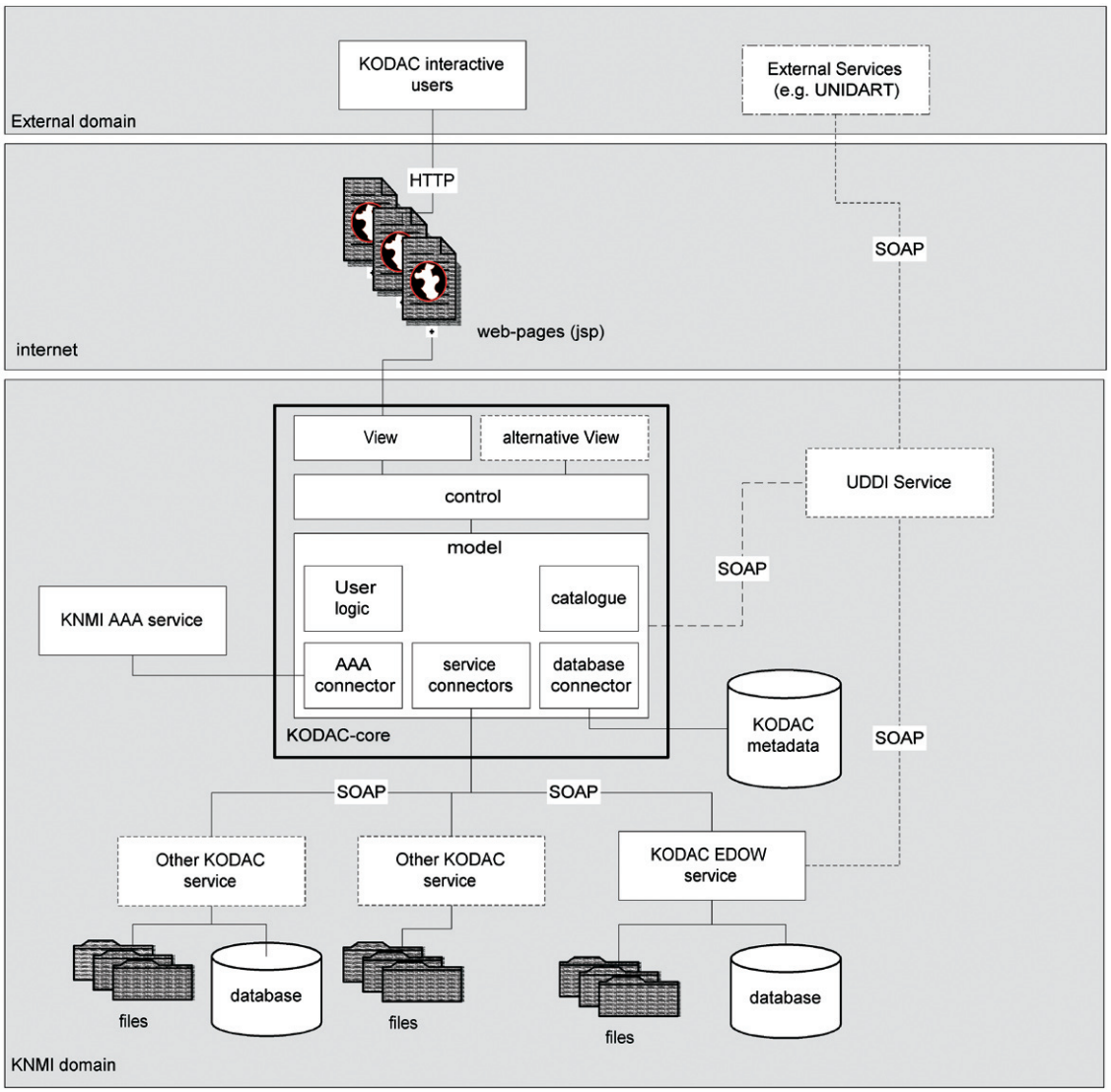

Figure 2. Schematic overview of the KODAC system. On the top the external domain with our customers is shown. The interactive users interact with the system using their web browser. The UDDI9) Service will be used by KODAC to discover the KNMI data services. Also External Services can interact and discover KODAC data services using this service. The KODAC core shows the Model View Controller (MVC) pattern in use, the model part shows the main parts of the business logic, among which the connection to the KNMI Authentication, Authorization and Accounting (AAA) Service. At the bottom of the picture the data services are shown. Here the actual data is retrieved, which can be in file (systems), database records or in online tape archive systems.

ized climatological reports to the users. One of the reasons of taking the climatological reports as pilot is that it will yield knowledge and proof that the design concept is feasible within a general KNMI scope.

The proof of concept, consisting of a fully functional system, will be made available in an operational environment, thus embedding the system in the KNMI infrastructure. After this, more datasets and more functionality will be added to the KODAC system.

Acknowledgements:
The authors wish to acknowledge the contributions by : Dick Blaauboer, Jan Willem Noteboom, Chris Verhoef, Maarten van der Hoeven, Henk van Dijk, Hans de Vries and Ruud van der Steeg.

1) NL-SCIA-DC: Netherlands Sciamachy Data Centre, *http://neonet.knmi.nl/neoaf/*
2) TEMIS: Tropospheric Emission Monitoring Internet Service, *http://www.temis.nl*
3) ECA&D: European Climate Assessment and Dataset, *http://eca.knmi.nl/*
4) Requirements document KODAC, version 2.1 (KODAC-URA.doc)
5) Inspire: Infrastructure for Spatial Information in Europe, *http://inspire.jrc.it/*
6) UNIDART: Uniform Data Request Interface. EUMETNET project for establishing a European data infrastructure for meteorological resources, *http://www.dwd.de/UNIDART*
7) Apache TOMCAT application server, *http://jakarta.apache.org/tomcat/*
8) Apache Struts framework, *http://struts.apache.org/*
9) UDDI. Universal Description, Discovery and Integration, *http://www.uddi.org/*

European Climate Assessment & Dataset project (ECA&D)

Albert Klein Tank, Aryan van Engelen, Maarten van der Hoeven and Janet Wijngaard

Introduction

Nature and society are more vulnerable for changes in severe weather and climate events than for changes in the mean state of the climate. Compared to the existing information on past changes in the mean (such as the observed global temperature rise), far less is known about past changes in extremes (such as the change in the number of intense rainfall events). Knowledge on past changes in extremes is relevant to establish baselines for adequate monitoring of future climate change and supports the detection of anthropogenic influences on climate. It also serves as a reference against which climate models are validated when assessing their ability to simulate the climate.

Objectives

The ECA&D project of EUMETNET, which is lead by KNMI, aims at increasing the knowledge on past changes in extremes over Europe through the analysis of historical records of observations at meteorological stations. The key question addressed is: how did the extremes of daily surface air temperature and precipitation change in Europe's climate of the 20th century, and what can we learn from this?

Daily dataset

For statistical reasons, a valid analysis of extremes requires long time series of observations to obtain reasonable samples. Also, series with at least a daily time resolution are needed to take into account the sub monthly nature of many weather and climate extremes. Europe is traditionally one of the regions of the world lacking a dataset of high-resolution observational series with sufficient density and quality that is readily available and accessible. ECA&D's objective is to produce such a comprehensive daily dataset.

Trends in extremes

To gain a uniform perspective on observed changes in climate extremes, the joint Working Group on Climate Change Detection of the World Meteorological Organization – Commission for Climatology (WMO–CCL) and the Research Programme on Climate Variability and Predictability (CLIVAR) recently defined a core set of standardized indices[1]. Each index describes particular aspects of climate extremes in daily data. ECA&D's objective is to analyse the trends in the extremes of Europe's climate of the past using these standardized indices.

Detection/Attribution

There is increasing concern that climate extremes may be changing in frequency and intensity as a result of human influences on climate. But natural variability masks anthropogenic trends and single extreme events (such as the 2003 summer heat waves in Europe) cannot be simply and directly attributed to anthropogenic climate change if the event in question might have occurred naturally. Anomalously higher numbers of extremes in recent years may provide a fingerprint of anthropogenic climate change. ECA&D's objective is to search for such fingerprints in carefully selected parameters of extremes derived from daily data.

Results

Web access to the daily dataset

The dataset constructed in ECA&D consists of daily series of temperature (min, max and mean) and precipitation at a large number of meteorological stations throughout Europe and the Mediterranean2). Most series cover at least the period 1946–99 (Figures 1 and 2). Almost all series are available for climate change research at *http://eca.knmi.nl*. The series at this website are blended with daily data derived from synoptic observations that are transmitted on a routine basis over the Global Telecommunication System and therefore always up-to-date. The website offers the possibility to create custom cross-sections through the data both in ASCII and NetCDF and provides an overview of the results of climate change analyses using indices of extremes as well.

Homogeneity assessment

In any long time series, changes in observation practices may have introduced inhomogeneities of nonclimatic origin that severely affect the extremes. Within the project[3] statistically tested the daily series (1901–99) of surface air temperature and precipitation with respect to homogeneity. The results were condensed for each series into three classes: 'useful–doubtful–suspect'. In the period 1901–99, 94% of the temperature series and 25% of the precipitation series were labelled 'doubtful' or 'suspect'. In the subperiod 1946–99, 61% of the temperature series and 13% of

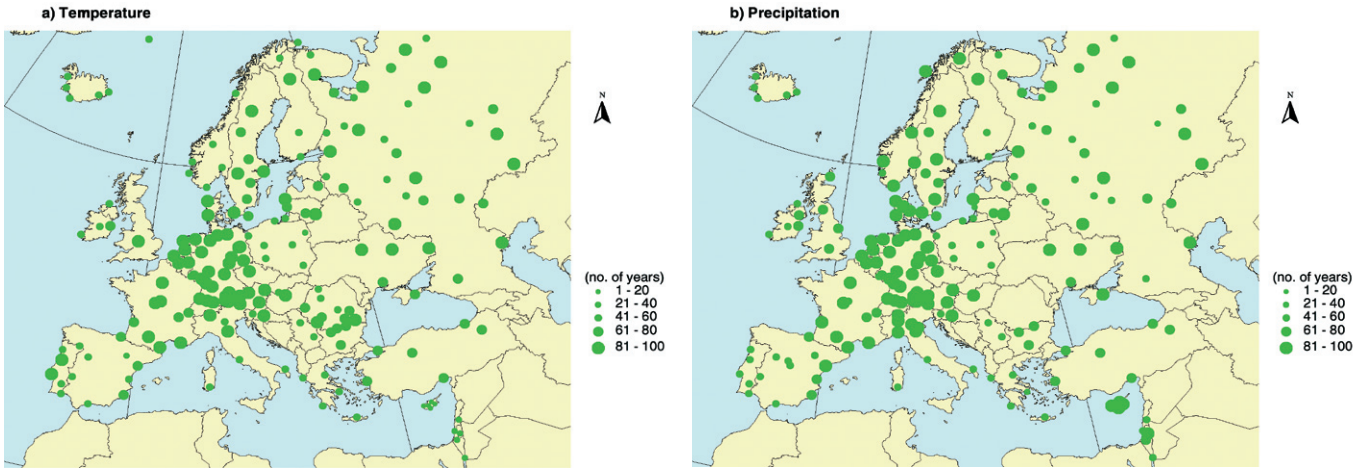

Figure 1. Stations with daily temperature (a) and daily precipitation (b) series in the ECA dataset. Station dots are scaled with the length of the time series.

The eca.knmi.nl website offers the possibility to query the ECA database and download daily station series

the precipitation series were assigned to these classes. About 65% of the statistically detected inhomogeneities in the temperature series labelled 'doubtful' or 'suspect' in the period 1946–99 were traced back to observational changes that are documented in the metadata. For precipitation this percentage was 90%. The remainder of the detected inhomogeneities may still be real climate related changes.

Indices

The high percentage of series labelled 'doubtful' or 'suspect' indicates that only part of the dataset was adequate for reliable trend analysis. The European trends (1946–99) in the temperature indices reflect the general warming: fewer cold extremes, more warm extremes. Averaged over all stations of the subset, the first decades of slight cooling saw narrowing of the distributions of daily minimum temperature and daily maximum temperature, whereas the last decades of strong warming saw widening of the distributions of daily minimum temperature and daily maximum temperature. For precipitation, all indices of wet extremes increased between 1946–99 when averaged over Europe. One index suggests that in wetting areas, the changes in the high intensity events were larger than expected on the basis of the changes in the average precipitation amounts, implying an amplified response of the wet extremes[4]. The indices results obtained in ECA&D did already feed into the worldwide studies of changes in indices of extremes as performed for the Third Assessment report of the IPCC[5,6]. They will also feed into similar activities that are planned in the preparatory stage of the Fourth Assessment Report AR4.

Fingerprints

Formal detection/attribution of anthropogenic climate change involves comparing the evolution of the most likely signal from anthropogenic change in GCM simulations of climate under changing greenhouse gas concentrations (the fingerprint) against the observations. Such studies did form the basis for the strong conclusion in the third assessment report of the IPCC that "most of the warming observed over the last 50 years is attributable to human activities". We have shown that some of the characteristic change patterns found in the daily data over Europe provide a signal of anthropogenic influence, as they are distinct from the estimated patterns associated with natural temperature variability[7]. Therefore, the identified patterns are good candidates for fingerprints in formal climate change detection/attribution studies.

Outlook

The ECA&D project shows that although climate data do exist, they are of insufficient quality, unavailable to the scientific community or scattered over many data holders. To keep its value for climate change research, the daily dataset needs to be updated at a regular basis, as well as further quality controlled and

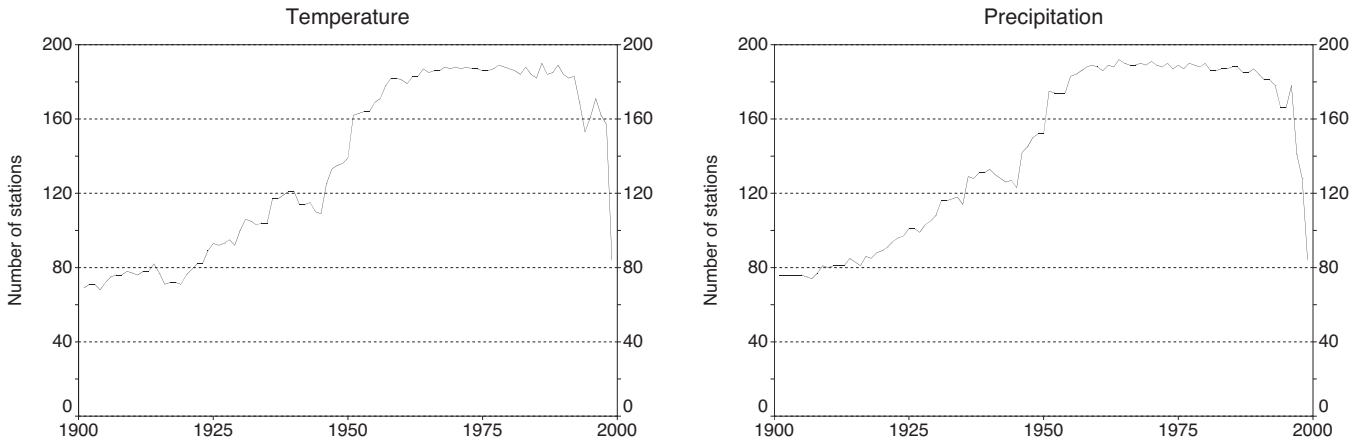

Figure 2. Number of stations with daily temperature (a) and daily precipitation (b) series in the ECA dataset.

elaborated with metadata information. A complicating factor in the comparisons between area-based extreme events in climate models and extremes in station observations is that the latter are point observations that require some form of area averaging (gridding) in order to adjust for the different scales involved. Gridding of the daily resolution series of ECA&D is part of the European Union Integrated Project ENSEMBLES, which started in September 2004 and runs for 5 years. ECA&D will continue the full range of its current activities, as the combination of data collection and dissemination with quality control, homogeneity testing and trend analysis proves to be essential for success. The short-term goal is to publish the third European Climate Assessment report in 2006. The long-term goal is to establish a European focal point for high-resolution (at least daily) climatic data, including metadata and results of extremes analyses.

1) Peterson, T.C., C. Folland, G. Gruza, W. Hogg, A. Mokssit and N. Plummer, 2001. *Report on the Activities of the Working Group on Climate Change Detection and Related Rapporteurs 1998-2001*. Report WCDMP-47, WMO-TD 1071, WMO, Geneva, Switzerland.
2) Klein Tank, A.M.G., J.B. Wijngaard, G.P. Können, R. Böhm, G. Demarée, A. Gocheva, M. Mileta, S. Pashiardis, L. Hejkrlik, C. Kern-Hansen, R. Heino, P. Bessemoulin, G. Müller-Westermeier, M. Tzanakou, S. Szalai, T. Pálsdóttir, D. Fitzgerald, S. Rubin, M. Capaldo, M. Maugeri, A. Leitass, A. Bukantis, R. Aberfeld, A.F.V. van Engelen, E. Forland, M. Mietus, F. Coelho, C. Mares, V. Razuvaev, E. Nieplova, T. Cegnar, J. Antonio López, B. Dahlström, A. Moberg, W. Kirchhofer, A. Ceylan, O. Pachaliuk, L.V. Alexander and P. Petrovic, 2002. *Daily dataset of 20th-century surface air temperature and precipitation series for the European Climate Assessment*. Int. J. Climatology, **22**, 1441-1453.
3) Wijngaard, J.B., A.M.G. Klein Tank and G.P. Können, 2003. *Homogeneity of 20th century European daily temperature and precipitation series*. Int. J. Climatology, **23**, 679-692.
4) Klein Tank, A.M.G. and G.P. Können, 2003. *Trends in indices of daily temperature and precipitation extremes in Europe, 1946-1999*. J. Climate, **16**, 3665-3680.
5) Houghton, J.T., Y. Ding, D.J. Griggs, M. Noguer, P.J van der Linden and D. Xiaosu (Eds.), 2001. *Climate Change 2001 The Scientific Basis*. Contribution of Working Group I to the Third Assessment Report of the Intergovernmental Panel on Climate Change (IPCC), Chapter 2, 156-159, Cambridge University Press, UK, pp944.
6) Frich, P., L.V. Alexander, P. Della-Marta, B. Gleason, M. Haylock, A.M.G. Klein Tank and T. Peterson, 2002. *Observed coherent changes in climatic extremes during 2nd half of the 20th century*. Clim. Res., **19**, 193-212.
7) Klein Tank, A.M.G., G.P. Können and F.M. Selten, 2005. *Signals of anthropogenic influence on European warming as seen in the trend patterns of daily temperature variance*. Int. J. Climatology, **25**, 1-16.

First results of the Ozone Monitoring Instrument

Pieternel Levelt, Ellen Brinksma, Pepijn Veefkind and René Noordhoek

Introduction

Which region in The Netherlands suffers from the worst air pollution? Where can I safely sunbath the day after tomorrow? Is the ozone layer already recovering a little? And how is the climate affected by the release of aerosols (tiny particles or droplets floating in the air)? These are just some of the questions the Ozone Monitoring Instrument (OMI) will help KNMI to answer with it's measurements from space. OMI was launched on board NASA'S EOS (Earth Observing System) Aura satellite on 15 July 2004. After a few busy months of testing and calibration of the instrument, the OMI data are now flowing into KNMI and NASA.

The OMI instrument

The OMI instrument[1,2] is a nadir viewing imaging spectrometer which measures the solar radiation backscattered by the Earth's atmosphere and surface over the entire wavelength range from 270 to 500 nm, with a spectral resolution of about 0.5 nm. The 114° viewing angle of the telescope corresponds to a 2600 km wide swath on the surface, which enables measurements with a daily global coverage. The light entering the telescope is depolarised using a scrambler and then split into two channels: the UV channel (wavelength range 270 - 365 nm) and the VIS channel (wavelength range 365 - 500 nm). In the normal operation mode, the OMI pixel size is 13 km × 24 km at nadir (along x across track). However, in the zoom mode the spatial resolution can be reduced to 13 km × 12 km. The small pixel size enables OMI to look 'in between' the clouds, which is very important for retrieving tropospheric information. OMI is a Dutch-Finnish contribution to NASA'S EOS Aura mission.

Science goals of OMI

Aura's mission is to study the Earth's atmosphere and climate[3]. The Aura satellite consists of 4 instruments, among which is OMI. OMI's science questions are: 1) Is the ozone layer recovering as expected? 2) What are the sources of aerosols and trace gases that affect global air quality and how are they transported? 3) What are the roles of tropospheric ozone and aerosols in climate change? and 4) What are the causes of surface UV-B change? OMI contributes by measuring ozone and various trace gases (nitrogen dioxide, bromide oxide, formaldehyde, sulphur dioxide and chloride oxide), aerosols, clouds and ultraviolet radiation[1,4]. The amounts are being calculated by using the specific radiative properties from each gas (or aerosol) on the reflected sunlight. The reflected sunlight measured by OMI contains 'fingerprints' of the gasses and aerosols in the atmosphere. OMI's unprecedented high spatial resolution of 13 km × 24 km at nadir in combination with daily global coverage (Figure 1), enables new studies of air pollution, the ozone layer and climate change. Also, because of the high spatial resolution, OMI can make much more observations with cloud free scenes as previous instruments – clouds are well known to disturb UV/VIS satellite measurements.

Is the ozone layer recovering?

The most notorious effect of the thinning of the ozone layer by man-made CFC's is the ozone hole situation above Antarctica each year during local

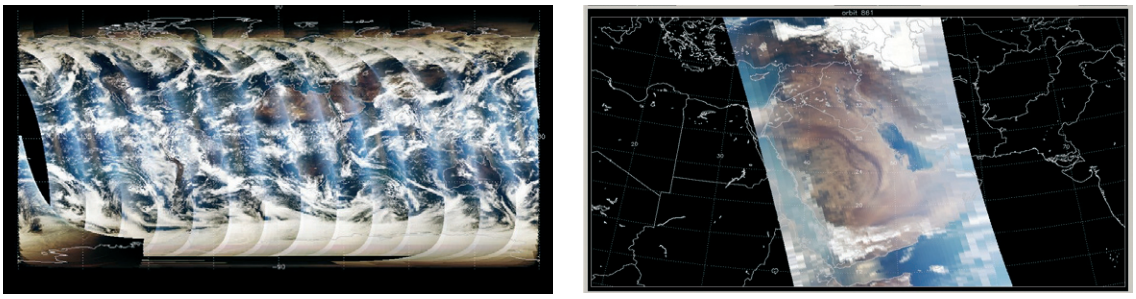

Figure 1. OMI (preliminary) measurement represented as colour images. On the left hand side: all measurements (made at the daylight side) on 3 October 2004. On the right hand side: a detail over Saudi Arabia on 12 September 2004. In this case, a zoom-in mode was used (the smallest ground pixel is here 13 × 12 km²). One can see clearly that resolution is best in the middle of the orbit (nadir view). The resolution is getting smaller towards the edge.

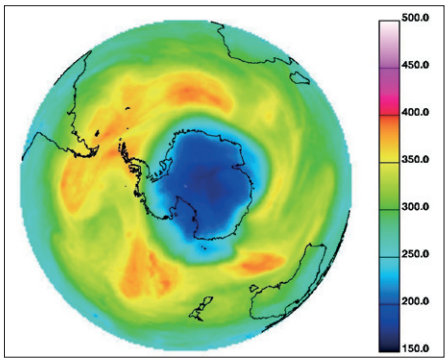

Figure 2. The ozone hole above Antarctica as seen with OMI on 1 November 2004. The colour scale is in Dobson units (DU).

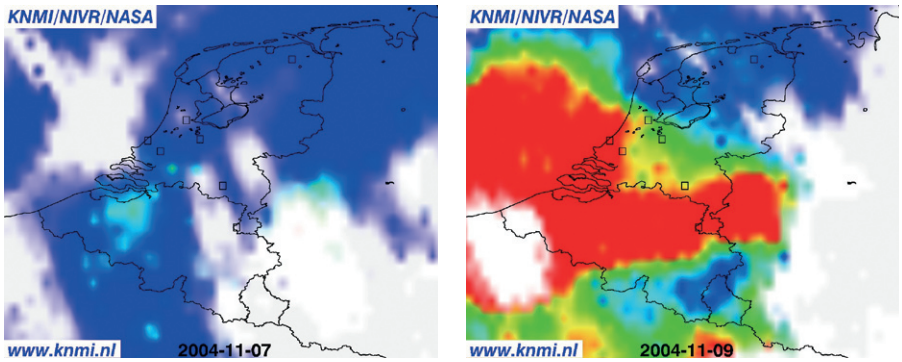

Figure 3. Nitrogen dioxide distribution (mainly caused by industry and traffic) map above the Netherlands of 7 and 9 November 2004. In the red areas is the pollution by nitrogen dioxide 5 to 10 times larger than in the clean, blue areas. White areas are covered with clouds. It is clearly visible that the air quality in The Netherlands can change considerable in 2 days time.

OMI's unprecedented high spatial resolution of 13 km × 24 km at nadir in combination with daily global coverage, enables new studies of air pollution, the ozone layer and climate change

spring (September – November). The ozone hole has been observed in both ground- and satellite measurements since the mid 1970's (it did not exist before that time). The preliminary observations (OMI was still in it's testing phase) of the ozone hole in 2004 (Figure 2) show that OMI works fine: the results show great detail and are consistent with observations by other satellites and ground measurements. Beside ozone, OMI also measures gasses that are related to the process of ozone destruction, like nitrogen dioxide, bromide oxide and chloride oxide.

The ozone layer is also thinning elsewhere in the world. Changes in ozone on time scales of several decades are studied to examine the impact of human actions. Long-term measurements of ozone are available, thanks to ground measurements (at some locations available already from the 1920's) and satellite measurements since the 1970's. Those long-term measurements should show us how much thinner the ozone layer has become. Determining this long-term trend is a difficult task as it is masked by all kinds of natural variations. Therefore, one needs decades of very precise measurements, preferable on a global scale. A more consistent picture should emerge by connecting the OMI measurements with those made by it's predecessors (among others NASA's TOMS series of satellites and ESA's GOME and Sciamachy instruments). How and when the ozone layer will recover is currently unknown. Most atmospheric models predict a recovery in the second part of the 21th century. Climate change can delay this recovery, due to predicted decreasing temperatures in the stratophere. OMI's measurements will contribute several pieces to this puzzle.

Air pollution at an urban scale

It was a great news story at the end of November 2004 in Dutch newspapers and television news reports: *"Scharwoude is the cleanest village, the 'Randstad', the South of Zeeland and Limburg are the most polluted regions of The Netherlands. KNMI can measure everyday everywhere air pollution on scales of large city thanks to aerosol and nitrogen dioxide observations from OMI"*. Those species are common in high concentrations on places with combustion processes. In The Netherlands that are typical places with industrial plants and busy traffic. OMI can map the distribution, displacement and time of existence of air pollution. OMI is the first satellite instrument which is able to map nitrogen pollution on a daily basis.

The Netherlands is one of the most polluted regions in the world. However, within The Netherlands, remarkably large differences are present: between different regions but also on a day-to-day basis. This is illustrated in the observations of 7 and 9 November 2004 (Figure 3). The first day is clearly cleaner than the second. The difference is caused by the weather conditions, especially wind speed and direction, and the difference in production of pollution (the first day is a Sunday). The impact of weather is most notable, like the smog conditions in the summer: pollution does not spread out vertically in high-pres-

sure regions, resulting in increased pollution near the surface.

Satellite measurements of air pollution by OMI are a good extension to the ground measurements made by the Institute for Public Health and Environment (RIVM). RIVM and KNMI are now working together in making an air quality forecast, which should forecast the amount of air pollution a few days ahead.

Biomass burning

Next to industry and traffic, biomass burning and desert dust are other important sources of air pollution. Biomass burning is caused by forest fires and agriculture land burnings and produces several species, of which tropospheric nitrogen dioxide, tropospheric ozone, formaldehyde and aerosols can be detected by OMI. Biomass burning occurs most often in South America, Africa and Asia. Figure 4 shows a good example of the fact that air pollution can travel over great distances, even to different continents. A cloud of tropospheric ozone, the so-called 'brown cloud' (also visible in tropospheric nitrogen, a precursor for tropospheric ozone) stretches from Brazil to Africa. OMI also has made first measurements of formaldehyde, an air pollutant which is mainly produced by biomass burning (see Figure 5).

Climate change

Ozone and aerosol in the troposphere (the lower 10 to 15 km of the atmosphere) influence the temperature on Earth and therefore the climate. Important climate parameters of these species are the amount and distribution as a function of height, and for aerosol also it's precise composition (which determine the radiation properties). OMI measurements of tropospheric ozone (see Figure 3) and aerosol, in particular the UV absorbing aerosols, will contribute to the research on climate change. In Figure 6 the first measurements of aerosol above Australia due to biomass burning are shown. OMI measures aerosol optical thickness, which is a measure for the amount of aerosols, and aerosol single scattering albedo, which gives information on the amount of absorption of a particular aerosol, and therefore on the type of aerosol. Figure 6 shows that for the aerosols surrounding and above Australia the single scattering

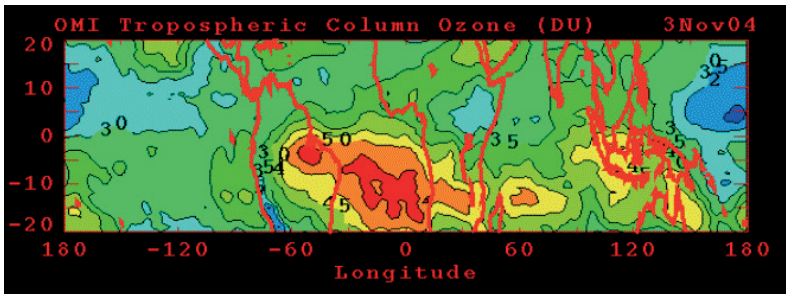

Figure 4. Tropospheric ozone on 3 November 2004, as retrieved from OMI measurements. The large cloud between Brazil and Africa is believed to originate from biomass burning. The colour scale is in Dobson units (DU).

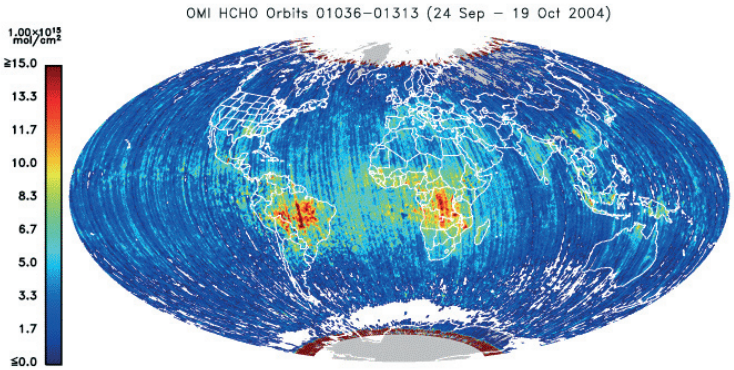

Figure 5. A twenty-six day average of OMI (preliminary) measurements of formaldehyde (HCHO) due to biomass burning and antropogenic emissions. The colour scale is in 10^{15} molecules per cm^2.

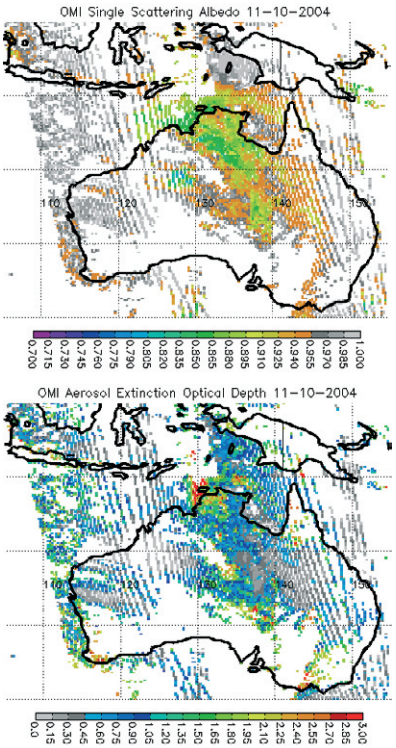

Figure 6. OMI Aerosol single scattering albedo (upper panel) and aerosol optical depth (lower panel) above Australia on the 11th of October 2004. Colour scales run for single scattering albedo and aerosol optical depth between 0 and 1 and 0 and 3 respectively.

albedo varies, which is an indication that the aerosols originate from different sources.

UV-index: Safely sunbathing?

Changes in the amount of ozone at time scales of a few days and resolved at urban scale resolution as measured by OMI can be used to calculate the UV-forecast for several days ahead. This so-called UV index can be used to advise the public to protect themselves better on days with unusual high UV radiation levels.

Volcanic Activity

OMI can measure volcanic activity by detecting volcanic aerosol and sulphur dioxide. The first measurements of OMI of sulphur dioxide are shown in Figure 7 and show the explosive eruption of the volcano Manam in Papua New Guinea at the 24th of October 2004. OMI proved to be able to measure passive out gassing of volcanoes. OMI's sensitivity to sulphur dioxide is about ten times higher than it's predecessor TOMS. OMI's measurements can potentially be used for aviation safety control.

Outlook

In 2005 KNMI and NASA will check and improve on the OMI data quality and start a large validation exercise, involving European and USA validation groups. Apart from off-line products, KNMI will also built a Near Real Time (NRT) System, which will be able to deliver the ozone columns within 3 hours after measurement. ECMWF and NOAA will use these data in their weather forecast systems. The Finnish Very Fast Delivery (VFD) System will be able to provide ozone columns and UV-B for Europe within 30 minutes after measurement. The VFD system is scheduled to be operational mid-2005, the NRT system at the end of 2005. It is expected that off-line OMI data will become gradually publicly available from mid-2005 onward, via internet (NASA-DAAC and KNMI). Based on the first results of OMI it is expected that OMI will be able to extend the ozone record of TOMS with the required accuracy. The tropospheric ozone and aerosol products will provide new measurements that can contribute to understanding the climate change question. OMI is expected to provide unprecedented tropospheric pollution data.

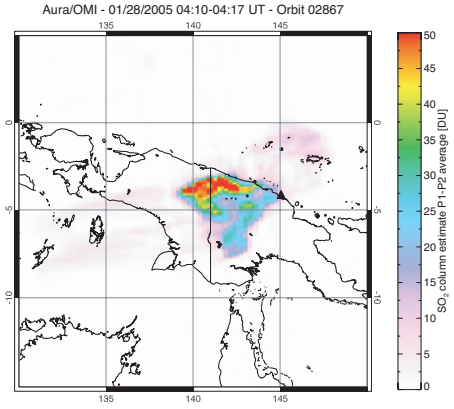

Figure 7. OMI SO2 (preliminary) measurements made 12 hours after the explosive eruption of the volcano Manan (4.01 degrees South, 145 degrees East) in Papua New Guinea on the 27th of January 2005. OMI is ten times more sensitive than TOMS.

Acknowledgements

The authors acknowledge R. Dirksen and M. Kroon (KNMI) for the RGB pictures (Figure 1), P. Veefkind (KNMI) for the ozone hole and nitrogen dioxide images (Figures 2 and 3), J. Ziemke (NASA-GSFC) for the tropospheric ozone image (Figure 4), T. Kurosu (Harvard Smithsonian) for the HCHO image (Figure 5), O. Torres (NASA-GSFC) for the aerosol images (Figure 6) and S. Carn (University of Maryland/UMBC) for the Manam explosion image of SO_2 (Figure 7). This work is sponsored by the space agencies NIVR, FMI and NASA.

1) Levelt, P.F., P.K. Bhartia, P. Stammes and K. Chance (Eds.), 2002. *OMI Algorithm Theoretical Basis Document, version 2, August 2002.* Available at *http://eospso.gsfc.nasa.gov/eos_homepage/for_scientists/atbd/index.php*

2) Stammes, P., P. Levelt, J. de Vries, H. Visser, B. Kruizinga, C. Smorenburg, G. Leppelmeier and E. Hilsenrath, 1999. *Scientific requirements and optical design of the Ozone Monitoring Instrument on EOS-CHEM*. Proceedings of Earth Observing Systems IV, Denver (CO), USA, July 1999, SPIE **3750**, 221-232.

3) Schoeberl, M.R., A.R. Douglass, E. Hilsenrath, P.K. Bhartia, J. Barnett, J. Gille, R. Beer, M. Gunson, J. Waters, P.F. Levelt and P. DeCola, 2004. *Earth Observing System Missions Benefit Atmospheric Research.* Eos, Transactions, American Geophysical Union, **85**, 18, 177-181.

4) Levelt, P.F. and 24 co-authors, 2000. *Science Requirements Document for OMI-EOS (RS-OMIE-KNMI-001, version 2, December 2000)*. Available at *http://www.knmi.nl/omi*

Using Lidar/Radar observations to improve cirrus cloud parameterisations

David P. Donovan, Gerd-Jan van Zadelhoff, Erik van Meijgaard and Reinout Boers

Introduction

It has long been recognized that cirrus clouds play an important role in determining the Earth's climate[1,2]. Cirrus clouds both reflect incoming solar radiation (exerting a cooling effect) and trap outgoing infrared (IR) thermal radiation (exerting a warming influence). Whether a given cirrus cloud has a net warming or cooling effect depends on its optical thickness, altitude and microphysical properties such as the size and shape of the cloud particles. For high altitude cirrus, the warming due to trapping of IR radiation emitted by the Earth's surface tends to dominate.

Of particular importance in determining an ice cloud's radiative properties is the effective radius (R_{eff}) of its constituent cloud particles. R_{eff} is a measure of the 'average-size' of the particles comprising a cloud and determines the relationship between the total ice crystal mass and visible optical depth. It also plays a large role in determining the appropriate visible scattering phase function and degree of IR absorption (single-scattering albedo). These scattering and absorption characteristics, in turn, determine the cloud's radiative impact. For spherical cloud particles R_{eff} may be defined in terms of the radii of the cloud particles. For non-spherical ice particles the situation is more complex. However, R_{eff} then can be defined in terms of the total mass and average cross-sectional area of the ice crystals.

In climate models clouds cannot be directly modelled[3]. This is due to the scale and complexity of the processes involved. Instead their properties must be specified or parameterised in terms of other larger scale variables. In particular, in climate models ice cloud effective particle size is either considered fixed or parameterised in terms of temperature[2]. One of our aims over the past two years has been to evaluate and improve the validity of these assumptions using data sets obtained by combined lidar/radar remote sensing of cirrus clouds.

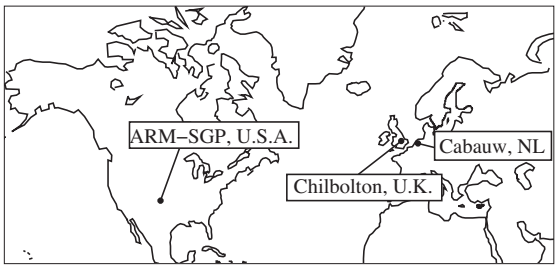

Figure 1. Approximate locations of the ground-sites considered in this work

Lidar/Radar ice cloud remote sensing

Over the past several years, a powerful new method for estimating ice cloud radiative properties, including their particle effective radius, from combined lidar and radar data has been developed at KNMI[4,5]. Lidar (Light Detection And Ranging) systems are similar in principle to Radar (Radio Detection and Ranging) systems and are often referred to as laser-radar systems. Both types of instruments transmit a pulse of electromagnetic energy and then detect the amount of energy that is scattered back to the receiver as a function of time. Since the speed of the signal is known, the time corresponding to a detected signal can be converted to range from the instrument and thus range-resolved profile measurements can be obtained. The key difference between lidars and cloud radars is that radars operate at microwave frequencies and employ antenna to transmit and receive signals while lidars operate using visible or IR light and employ lasers and telescopes. The difference in the lidar and radar returns from cirrus clouds are strongly influenced by the size of the particles. Informally speaking, cloud radars are more sensitive to 'large' cloud particles while lidars are relatively more sensitive to the 'small' particles. Thus, combined lidar and radar data may be used to estimate R_{eff} in cirrus clouds.

Comparing results from different sites

Previous work carried out at KNMI involved the analysis of 7 months of continuous data from the United States Government Atmospheric Radiation Measurement's (ARM) Southern Great Planes (SGP) site situated in Oklahoma in the US[7]. This work showed that the effective particle size of ice clouds over the ARM-SGP site could be parameterised in terms of the cloud temperature and the local ice water content (IWC)[7,8]. Since then, the KNMI lidar/radar procedure has been used in order to analyse a large amount of data from the Cabauw (Netherlands) and Chilbolton (UK) measurement sites. The approximate locations of the two

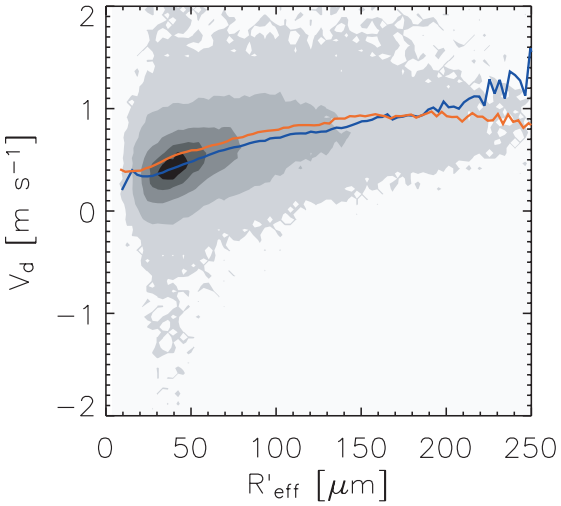

Figure 2. Relationship between observed Doppler velocity and lidar/radar effective particle size for Cabauw (Blue) and the ARM-SGP site (Red). The grey-scale contours are for Cabauw. The darkest contour corresponds to 10% of the measurements; the other contours contain 33%, 66% and 90% of the observations respectively.

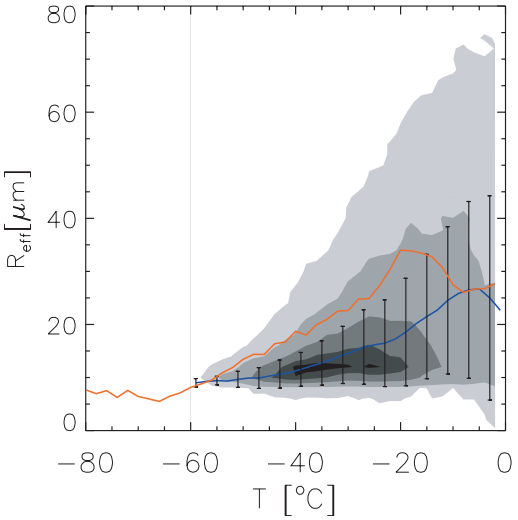

Figure 3. Observed relationship between effective particle sizes and temperature for Cabauw (blue line) and ARM (red line). The contours correspond to the Cabauw results and follow the same scheme as used in Figure 2.

In particular, in climate models ice cloud effective particle size is either considered fixed or parameterised in terms of temperature

European sites and the ARM-SGP site are shown in Figure 1. Both Cabauw and Chilbolton are participants in the EU-5 CLOUDNET program (*http://www.met.rdg.ac.uk/radar/cloudnet/*). The data from the three sites have been compared in order to ravel any differences or similarities regarding the morphology of the ice cloud particle effective radii.

In order to compare the ARM and CLOUDNET data sets in a consistent manner only clouds that were fully penetrated by the lidar (optical depth less that 3-4) were considered. Allowances for different instrument capabilities between the ARM-SGP site, Cabauw and Chilbolton (such as different radar sensitivities) were also taken into account. It was found that the relationship between Doppler fall velocity (measured by the Radars at each site) and ice cloud particle effect radii was similar at all three sites (see Figure 2). This finding gives us confidence that the data from the different sites can be usefully compared.

Analyses of two years of CLOUDNET data have revealed that a significant correlation between average effective particle size, temperature and IWC does exist. The relationship found for the CLOUDNET data (the Cabauw and Chilbolton results were nearly identical in this regard) set is qualitatively similar to that found for the ARM data. This is, the average value of R_{eff} was found to increase with both increasing temperature and IWC. However, the relationships found for the ARM and CLOUDNET data sets are notably different in a quantitative sense (see Figure 3). This is an important finding as it points to a general inaccuracy in how the effective size of ice crystal is parameterised in large-scale atmospheric models.

New Effective size parameterisation

In many atmospheric models ice cloud effective radius is treated as a function of temperature. Usually a single function is used globally. However, as shown in Figure 3, our results indicate that the same R_{eff} -vs-Temperature (or even R_{eff} -vs-T and/or IWC) relationship cannot accurately represent the observed relationship over the CLOUDNET and ARM sites. However, as shown in Figure 4, it was found that the mean profiles of R_{eff} as a function of normalized height into the cloud for different cloud physical thickness ranges are quite similar over all the sites considered in this study[9]. This finding is consistent with the physical picture of particle formation near cloud

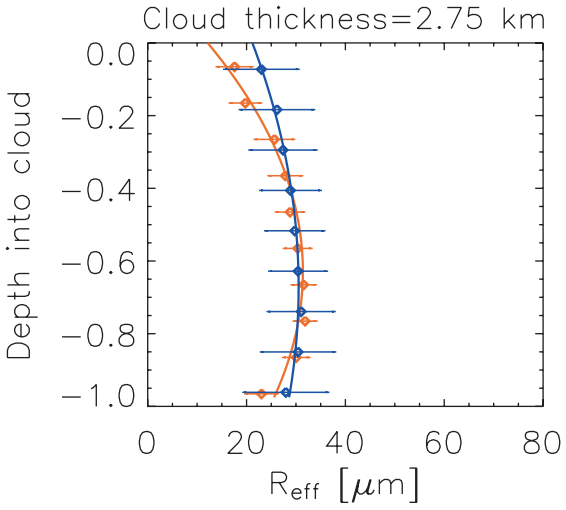

Figure 4. Average observed effective particle size as a function of normalized cloud depth for CLOUDNET *and* ARM-SGP *data. The results shown correspond to clouds whose physical thickness ranges between 2.5 and 3.0 km. Other similar relationships cover other thickness ranges.*

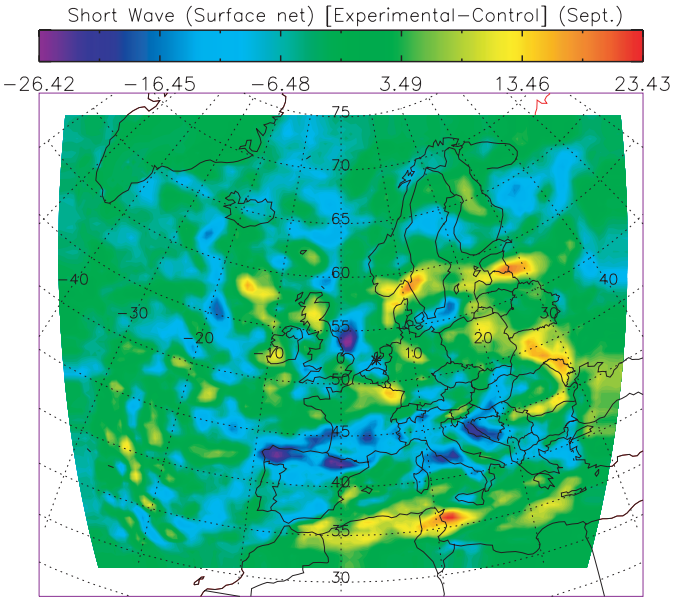

Figure 5. Difference in shortwave surface fluxes between the standard RACMO *ice cloud radiation scheme and a new scheme where ice cloud effective particle size has been parameterised as a function of cloud physical thickness.*

top followed by particle growth (mainly aggregation) as the ice particles fall followed by sublimation near cloud bottom.

Using the new findings, a new parameterisation that treats ice cloud R_{eff} as a function of cloud physical thickness has been formulated. The consequences of this new parameterisation are currently being studied using RACMO. In Figure 5 the differences in new shortwave surface forcing resulting from the new effective particle size parameterisation are shown. It can be seen that differences of up to 10-20 W/m² are present. These differences are significant and point to the importance of accurate representations of ice cloud radiative properties in atmospheric models. Predominant in Figure 5 are regions (blue) where the shortwave surface downward irradiance using the new parameterisation is smaller than previously. This means that, in general, the new parameterisation yields small values of R_{eff}. Similarly, the results imply higher cloud top albedos. This work is currently at a preliminary stage but is expected to eventually lead to an improved practical treatment of cirrus radiative effects in RACMO and other models.

Conclusion

The results of this work have been used to formulate parameterisations of cirrus cloud effective particle radii and other relevant quantities that are suitable for inclusion in atmospheric models. This work strongly argues that in formulating ice-crystal size parameterisation cloud physical thickness must play a role. The conventional procedure of parameterising ice cloud particle effective radii in terms of temperature has been shown not to be accurate when applied to two geographically dissimilar locations. Results using the new parameterisation have shown a significant impact on the surface and top-of-atmosphere radiation within RACMO. It is planned to extend this work by continuing the model analysis, analysing more data sets, assessing the implications for cirrus particle fall-speed parameterisations.

The KNMI lidar/radar procedure has been and will continue to be applied to the analysis of data sets including data acquired at Cabauw as part of the Cabauw Experimental Site for Atmospheric Research (CESAR) initiative. In addition, the KNMI lidar/radar procedure will be applied to future satellite missions such as CLOUDSAT/CALIPSO (NASA) and EarthCARE (ESA/JAXA). These missions will combine the novel profile information available from lidars and radars with traditional passive cloud remote sensing instrument data on a global scale. Future work will also concentrate on incorporating improved ice cloud related parameterisations within atmospheric models.

1) Arking, A, 1991. *The radiative effects of clouds and their impact on climate.* Bull. Amer. Meteor. Soc., **72**, 795-813.
2) Jakob, C., 2002. *Ice clouds in numerical weather prediction models: progress, problems, and prospects.* In: Cirrus, Oxford University Press, New York, USA, 327-345.
3) Quante, M. and D. O'C Starr, 2002. *Dynamical processes in cirrus clouds: A review of observational Results.* In: Cirrus, Oxford University Press, New York, USA, 346-374.
4) Donovan, D.P. and A.C.A.P. van Lammeren, 2001. *Cloud effective particle size and water content profile retrievals using combined lidar and radar observations, Part 1: Theory and examples.* J. Geophys. Res., **106**, 27425-27448.
5) Donovan, D.P., A.C.A.P. van Lammeren, R.J. Hogan, H.W..J. Russchenberg, A.Apituley, P.Francis, J.Testud, J.Pelon, M.Quante and J. Goddard, 2001. *Cloud effective particle size and water content profile retrievals using combined lidar and radar observations, Part 2: Comparison with IR radiometer and in situ measurements of ice clouds.* J. Geophys. Res., **106**, 27449-27464.
6) Donovan, D.P., M. Quante, I. Schlimme and A. Macke, 2004. *Use of equivalent spheres to model the relationship between radar reflectivity and optical extinction of ice cloud particles*. Appl. Opt., **43**, 4929-4940.
7) Donovan, D.P. and A.C.A.P. van Lammeren, 2002. *First ice cloud effective particle size parameterization based on combined lidar and radar data*. Geophys. Res. Lett., **29**, 10.1029/2001GL013731.
8) Donovan. D.P., 2003. *Ice-cloud effective particle size parameterization based on combined lidar, radar reflectivity, and mean Doppler velocity measurements*. J. Geophys. Res., **108**, 10.1029/2003JD003469.
9) Zadelhoff, G.-J. van, D.P. Donovan, H. Klein Baltink and R. Boers, 2004. *Comparing ice cloud microphysical properties using CloudNET and Atmospheric Radiation Measurement Program data*. J. Geophys. Res., **109**, 10.1029/2004JD004967.

Estimating extreme wave height probabilities from observations and the ERA-40 reanalysis

Andreas Sterl and Sofia Caires

Introduction

A weather forecast is essentially an initial value problem. Given the atmospheric state (the 'weather') at one time, the state at a later time can be calculated. The problem, however, with this simple view is that the atmospheric state is never known completely. For large parts of the atmosphere observations are not available (remote areas, upper air), and available measurements inevitably contain errors. To overcome this problem, the initial state for a new weather forecast is obtained by a combination of the latest forecast and all new observations. The latest forecast has usually been initialised six hours earlier and gives a good first guess for the initialisation of the new forecast. Most importantly, it provides a complete description of the atmosphere as by definition it has values of all relevant quantities at all grid points. The first guess is then combined with the newly available observations in a way respecting physical laws. The observations 'push' the first guess towards 'reality'. This step, by no means trivial, is called analysis. At ECMWF the analysis costs about half of the total CPU-time needed to make a 10 day forecast, the other half being used for the time integration.

As a consequence, operational forecast centres naturally produce a complete description of the atmosphere's state, usually four times a day. However, weather forecast models and analysis procedures are continually improved. Variability in the operational analyses is dominated by these changes rather than by natural variability, making them unsuitable to study long-term changes. The aim of re-analysis is to overcome this problem of inhomogeneity. A state-of-the-art analysis system is used to repeat the analysis procedure for the past. As a result one obtains a complete description of the atmosphere over a long period of time, which is free of inhomogeneities due to model changes. Unfortunately, inhomogeneities due to changes in data coverage remain[1].

ERA-40

The first global reanalyses were produced in the first half of the 1990s[2,3]. They are widely used in climate and meteorological research. Progress in modelling and data assimilation as well as the availability of new data sets led ECMWF to conduct a new reanalysis, ERA-40, covering the 45 years from September 1957 to August 2002. It uses a version of ECMWF's Integrated Forecasting System (IFS) that was operational in June 2001, albeit on a coarser grid (≈ 125 km instead of ≈ 40 km). A large subset of the complete ERA-40 data set is available at *http://data.ecmwf.int/data/d/era40_daily* on a 2.5° × 2.5° grid.

A distinguishing feature of the IFS is that over the oceans the surface roughness depends on the sea state[4,5], and the sea state is obtained from the WAM wave model[6]. Thus wave information is a natural product of ERA-40. One of the most important wave parameters is the significant wave height (H_S), a measure of the severity of the sea state. (To be precise it is the 20 minute-average of the upper third of a wave height record).

The length of the ERA-40 data set makes it especially suitable to study variability and extremes of weather-related quantities. Information about decadal variability of climate quantities and their extremes is of great interest for climate (impact) research. An example of an extreme parameter is the 100-year return wave height (H_{100}). This is the significant wave height that on average is exceeded only once every 100 years. It is used in the design of ships and of maritime structures.

Validation and correction of the ERA-40 wave product

We have thoroughly validated the raw ERA-40 wave data against buoy and altimeter data. Buoys provide high-quality continuous point measurements at a very limited number of sites. Satellite-born altimeters provide near-global coverage, but every point is sampled only once in several (typically 10) days.

Figure 1 shows the time series of H_S as derived from measurements at buoy 46001 in the Gulf of Alaska (148.3°W, 56.3 °N) during 1988 (blue), together with the corresponding ERA-40 data (red). Three properties of the ERA-40 data can easily be recognized:
(a) the two curves are nearly perfectly in phase,
(b) low wave heights tend to be slightly overestimated by ERA-40, and (c) high waves tend to be substantially underestimated. These three features are not a peculiarity of the special location, but a general

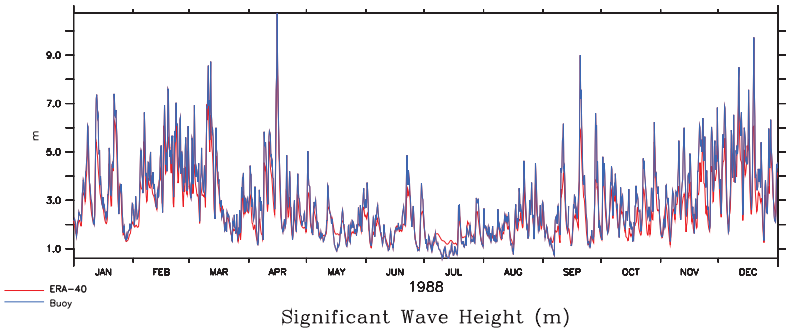

Figure 1. Measured (blue) and modelled (red) H_S at buoy 46001 (148.3°W, 56.3 °N) in 1988.

The length of the ERA-40 data set makes it especially suitable to study variability and extremes of weather-related quantities

property of the ERA-40 wave data. Among the reasons for these deficiencies are spatial resolution (P. Janssen, pers. communication) and a slight underestimation of high wind speeds[7].

Apart from the underestimation of large wave heights ERA-40 waves also suffer from inhomogeneities due to changes in the data that were assimilated. As a synthesized picture of the data Figure 2 shows the time series of the globally averaged monthly mean H_S from ERA-40 (blue). From 1991 onwards wave height data from altimeters flown onboard satellites became available and were assimilated. The impact of these data is clearly seen, especially for the period from December 1991 to May 1993, when erroneous data were used. Another inhomogeneity is visible in 1996, when the altimeter data changed from ERS-1 to ERS-2.

Fortunately, it was possible to devise a non-parametric correction method for the ERA-40 data. A corrected dataset was created[8] which has no bias with respect to altimeter-based wave height retrievals and which is free of obvious inhomogeneities resulting from differences in wave-height data that were assimilated (Figure 2, red). Furthermore, reliable estimates of the 100-year return wave height could be obtained from the raw ERA-40 data by a calibration against buoy measurements. These and other results from the ERA-40 wave data have been incorporated into the web-based KNMI/ERA-40 Wave Atlas (*http://www.knmi.nl/waveatlas*).

Estimation of extreme significant wave heights

For safety considerations it is important to know extreme wave heights, i.e., wave heights that are, on average, exceeded only once per 20, 50, or 100 years. The ERA-40 data set has proved an invaluable basis to derive global estimates of these extremes. Note that extremes of significant wave height rather than those of individual waves are obtained. Estimates of the 100-year return significant wave height H_{100} are obtained using the Peak-Over-Threshold (POT) method[9], in which the tail of the wave height distribution is fitted to the Generalized Pareto Distribution (GPD), the limit distribution for extremes.

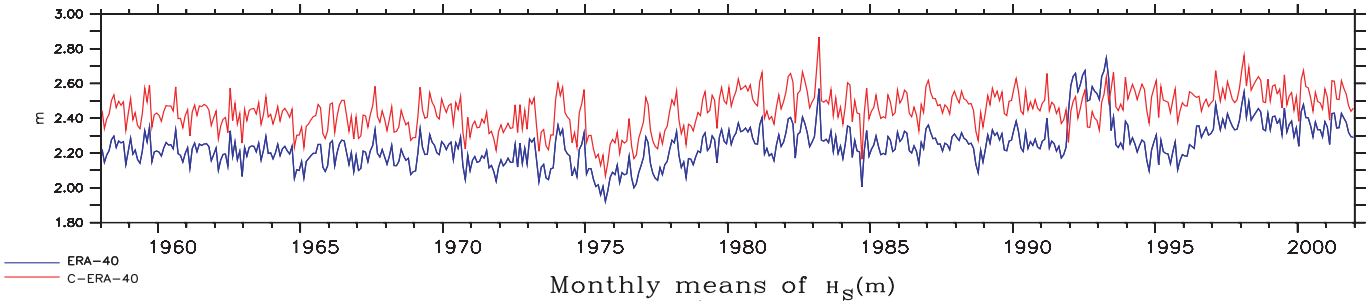

Figure 2. Time series of the monthly mean, globally averaged H_S from the raw (blue) and the corrected (red) ERA-40 data. Monthly means are computed from the 6 hourly fields.

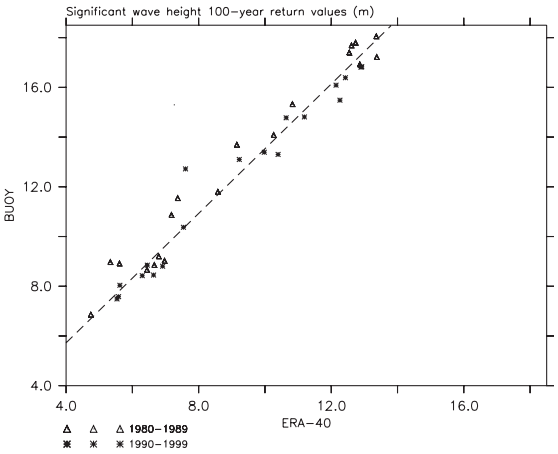

Figure 3. Linear correlation between 100 year return value estimates of H_S from buoy data and from ERA-40. The dashed line is eq. (1).

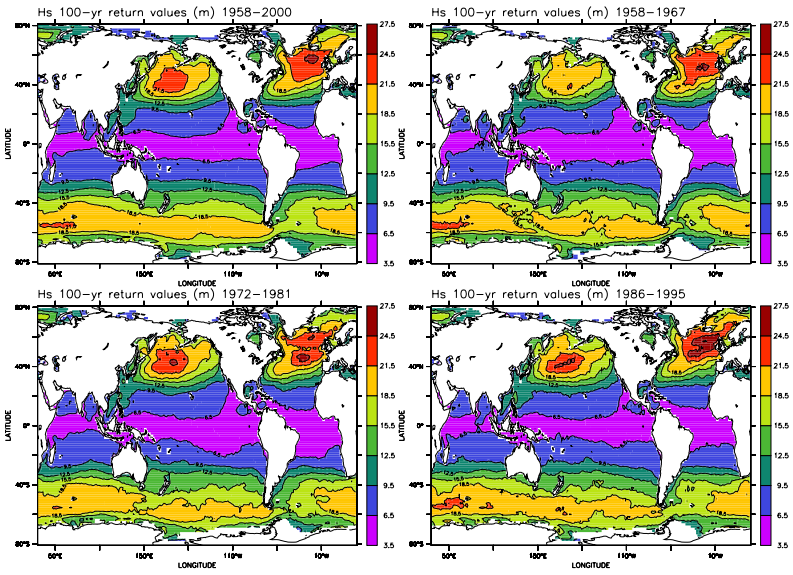

Figure 4. 100 year return H_S from ERA-40, corrected using the relationship displayed in Figure 3. Note that the results pertain to averages over 1.5° × 1.5° and 6 hours, that shallow water effects are not included, and that tropical cyclones are not resolved in ERA-40. The upper left panel is for the whole ERA-40 period (1958-2000), while the other panels are derived from three 10 year sub-periods as

Estimating H_{100} both from buoy measurements and from the raw ERA-40 data yields a linear relationship between the two[10]:

$$H_{100}(\text{buoy}) = 0{,}52 + 1{,}30\ H_{100}(\text{ERA-40}) \quad (1)$$

This relation is illustrated in Figure 3.

Buoy locations are very sparse and unevenly distributed in space, and the largest value of H_{100} found at the buoy locations is about 17 m (Figure 3). Therefore it would be preferable to have a relation between H_{100} estimates from ERA-40 and from satellites, respectively. However, satellites cross a given point only once in typically 10 days. Together with the relative shortness of the satellite record this gives too few data for a reliable extreme-value estimate at a given location. However, as far as parts of the estimation procedure were possible with satellite data their results are not incompatible with (1). We therefore apply this equation globally and for all values of H_{100}.

Figure 4 shows the H_{100} values obtained by applying the POT method to the ERA-40 data and correcting the results using (1). It is obvious that the highest values occur in the North Atlantic. While mean wave heights are not higher in the North Atlantic than they are in the North Pacific or in the Southern Ocean (Figure 5), the North Atlantic shows the highest variability (not shown). In other words, conditions in the Southern Ocean are always rough, while in the North Atlantic you can be lucky and the sea is calm even in winter, or you find yourself between the highest waves possible on earth.

Besides an estimate based on the whole ERA-40 period, Figure 4 also contains estimates of H_{100} for three different 10-year periods. The estimates obtained from these periods differ in the Northern Hemisphere storm tracks. Specifically, the estimates in the North Pacific storm track region have increased, and in the North Atlantic the pattern has changed. These differences can be attributed to decadal variability in the Northern Hemisphere, especially to changes in the phase of the NAO[8]. This example shows that it is important to take account of climate changes when designing maritime structures. A more detailed investigation reveals that in the North Atlantic changes in estimates of H_{100} are due to changes in the intensity of storms, while in the Southern Hemisphere they are mainly due to changes in the number of storms. In the North Pacific both factors contribute.

Summary and Conclusions

The ERA-40 reanalysis carried out at ECMWF produced 45 years (September 1957 - August 2002) of data describing the state of the atmosphere and the ocean surface four times a day. A subset of the raw

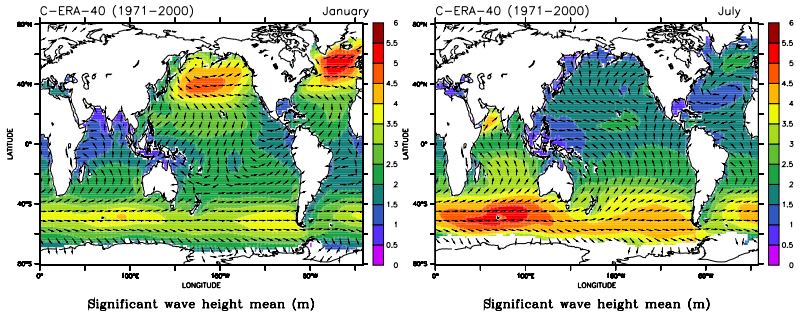

Figure 5. January (left panel) and July (right panel) averages of HS (colours) and propagation direction of waves (arrows) for the whole ERA-40 period.

ERA-40 data can be obtained from ECMWF's website at *http://www.ecmwf.int/data/d/era40_daily/*.
A thorough assessment of the ERA-40 wave height data revealed that they (a) capture very well the variability of the true wave heights on all time scales, (b) slightly overestimate low wave heights, and (c) severely underestimate high wave heights. Furthermore, inhomogeneities due to the assimilation of different data sources are clearly present. A non-parametric correction method was devised that eliminates most of these problems.

Despite the underestimation of high wave heights it is possible to give reliable estimates of extreme significant wave heights ('100-year-return values'). Estimates based on the raw ERA-40 wave data and those from buoy measurements reveal a linear relationship that can be exploited to obtain global reliable return value estimates based on the ERA-40 data. Maps of the ERA-40 data and derived quantities can be found in the web-based KNMI/ERA-40 Wave Atlas (*http://www.knmi.nl/waveatlas*).

Acknowledgments
We are indebted to many persons for their help and pleasant collaborations. Jean-Raymond Bidlot and Peter Janssen provided valuable suggestions and comments and helped with advice. Sakari Uppala and Per Kållberg as leaders of the ERA-40 production team where always open to our comments and provided valuable help in dealing with the technical aspects of the ERA-40 system. Helen Snaith helped with the altimeter data. The buoy data were obtained from NDBC-NOAA (http://www.nodc.noaa.gov/BUOY/buoy.html). This work was funded by EU as part of the ERA-40 project (no. EVK2-CT-1999-00027).

1) Sterl, A., 2004. *On the (in-)homogeneity of reanalysis products*. J. Climate, **17**, 3866-3837.
2) Kalnay, E., M. Kanamitsu, R. Kistler, W. Collins, M.I. Deaven, L. Gandin, M. Iredell, S. Saha, G. White, J. Woollen, Y. Zhu, M. Chelliah, W. Ebisuzaki, W. Higgins, J. Janowiak, K.C. Mo, C. Ropelewski, A. Leetmaa, R. Reynolds, R. Jenne and D. Joseph, 1996. *The NCEP/NCAR 40-year reanalysis project*. Bull. Amer. Meteor. Soc., **77**, 437-471.
3) Gibson, R., P. Kållberg, S. Uppala, A. Nomura, A. Hernandez and E. Serrano, 1997. *ERA description*. ECMWF Re-Analysis Project Report Series, **1**, ECMWF, Reading, UK, 73 pp.
4) Janssen, P.A.E.M., 1989. *Wave-induced stress and the drag of air flow over sea waves*. J. Phys. Oceanogr., **19**, 745-754.
5) Janssen, P.A.E.M., 1991. *Quasi-linear theory of wind wave generation applied to wave forecasting*. J. Phys. Oceanogr., **21**, 1631-1642.
6) Komen, G.J., L. Cavaleri, M. Donelan, K. Hasselmann, S. Hasselmann and P.A.E.M. Janssen, 1994. *Dynamics and Modelling of Ocean Waves*. Cambridge University Press, Cambridge, UK, 532 pp.
7) Caires, S. and A. Sterl, 2003. *Validation of ocean wind and wave data using triple collocation*. J. Geophys. Res., **108**(C3), 3098, doi:10.1029/2002JC001491.
8) Caires, S. and A. Sterl, 2005. *Validation and non-parametric correction to significant wave height data from the ERA-40 reanalysis*. J. Atmos. Oceanic. Technol., **22,** 443-459.
9) Coles, S., 2001. *An introduction to statistical modeling of extreme values*. Springer Texts in Statistics, Springer-Verlag, UK, 228 pp.
10) Caires, S. and A. Sterl, 2005. *100-year return value estimates for wind speed and significant wave height from the ERA-40 data*. J. Clim., **18,** 1032-1048.

CLIWOC - the climatological database for the world's oceans

Frits Koek and Günther Können

Introduction

Until recently the existing world climatological databases basically extended back to 1854. Examples are the Jones land database[1] and the Comprehensive Ocean-Atmosphere Data Set COADS[2,3], recently renamed ICOADS[4]. Observations prior to 1854 are generally considered to be of poorer quality. One reason is that, going back further in time, there is an increasing deficiency of instrumental observations of temperature and surface air pressure; another reason is the lack of standardization of the observation practices in the pre-1854 era. Although the data in the latest version of ICOADS (Release 2.1)[5] now extend back to the early 1800's by adding data from ship logbooks from the US Maury collection[6], no serious attempts have been undertaken so far to homogenize the pre- and post-1854 data. The main reason is that no standardized methods exist to convert archaic wind and weather terminology from old logbooks to present day units. There is, however, increasing consensus that daily wind reports made aboard ships represent an enormous potential for climate reconstruction of the pre-1850 era, enabling e.g. the study of low frequency climate variability. In 2000 the three-year EU project CLIWOC (Climatological Database for the World's Oceans 1750-1854) started the labour-intensive task of keying the contents of pre-1854 ship logbooks from voyages over the open oceans, to make them available for the scientific community.

Objectives of CLIWOC

CLIWOC was launched to compile a world's oceans meteorological database (back to 1750) by digitising and interpreting data from logbooks of pre-1854 oceanic voyages by English, Spanish, Dutch and French ships. Countries involved were Spain, UK, Argentina and The Netherlands. Also a 'dictionary' was developed that translates the archaic wind force terms from the four languages into Beaufort equivalents[7]. This dictionary is included in the database as a dynamic module, to facilitate updating. Apart from producing the database for the world's oceans between 1750 and 1854, the principal objective of CLIWOC was to draw attention to the scientific potential of the climatic data in the ships' logbooks, and to prove the value of the daily weather observations made aboard ships.

The logbooks

The ship's logbook is a legal document that contains detailed descriptions of what took place on board. It was also used to document new shipping routes and to assist in safe navigation. By 1750 the use of logbooks, often in a prescribed and tabular format, was standard practice on most ships. This resulted in a heritage of many logbooks in which detailed meteorological observations are systematically recorded.

Unravelling ancient time and position information

To be useful for climatic research the date of the observation must be known, as well as the position with sufficient accuracy, say, within 200 km.
To unravel this information several problems had to be overcome.

In the period 1750-1752 the date on board some of the British vessels referred to the old-style Julian calendar instead of the currently-used Gregorian calendar. Fortunately in most cases the weekdays were recorded as well, which allows for an unambiguous correction.

A second problem was the use of variable prime (or zero) meridians. A range of prime meridians was used by different nations. Apart from some well-known historic zero meridians, e.g. Tenerife, Cadiz and Paris, it was also common to denote the longitude with respect to the land that was sighted most recently. Hence, the prime meridian could shift several times during a voyage (Figures 1 and 2). In the project 646 different prime meridians were recognized. In about half of these cases, the meridians were documented explicitly in the logbooks and corrections were trivial. However, a straightforward reconstruction of the zero-meridian's position was frequently hampered by the fact that the geographical names often differed from present-day names. At times it was necessary to study old atlases and charts. Even more problematic are the many transitions in prime meridian that are not explicitly mentioned in the logbooks. These often become apparent only after plotting the ships' positions. Fortunately, it turned out that the latitude of the break in the ship's longitude usually provides enough information to deduce the location of the landmark upon which the new prime meridian was based.

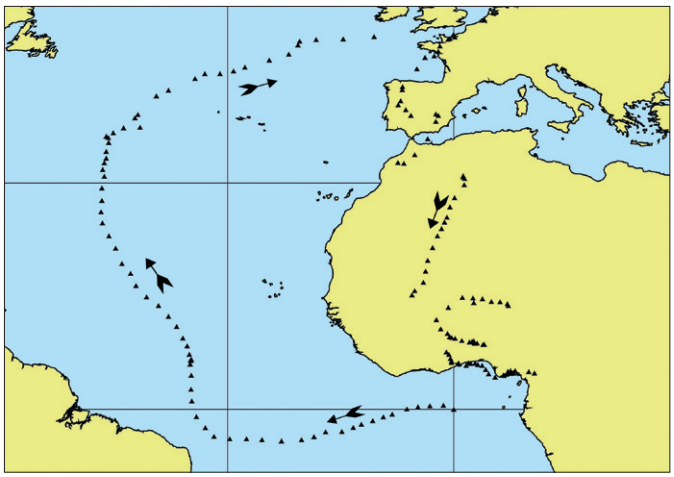

Figure 1. Raw positions of the British HMS Surprise (1750-1751) on a round trip from England to the Gulf of Guinea without correcting the longitude to the current standard, i.e. Greenwich. During the voyage back no transition in prime meridian occurred by absence of land sightings.

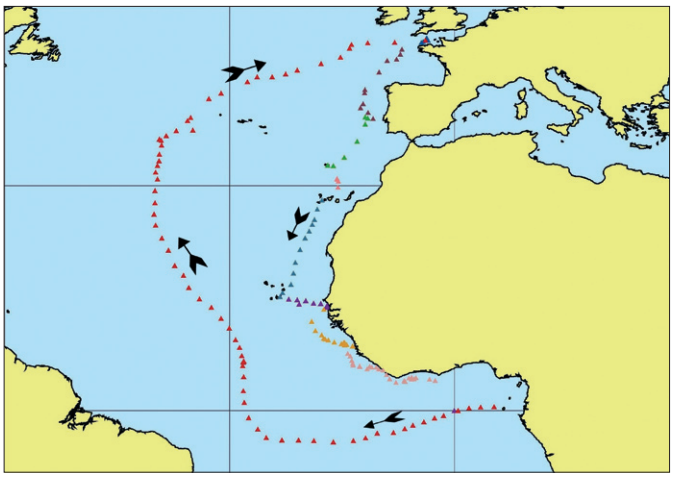

Figure 2. Corrected positions of the British HMS Surprise after converting the longitudes to the Greenwich meridian. Every colour refers to the use of another prime meridian: Start Point (which is the name of a land tongue in SE England at 50°13'N, 3°38'W), Ushant, Cape Roxent, Madeira, Point Negro, Isle of May Bay, Cape St Maries, Bananas and – at the start of the trip back – St Thomas.

The principal objective of CLIWOC was to draw attention to the scientific potential of the climatic data in the ships' logbooks, and to prove the value of the daily weather observations made aboard ships

Wind speed equivalents

Quantitative interpretation of the observation was the next step. This applies in particular to wind speed, being the bulk of the pre-1854 meteorological reports and almost exclusively the contents of the reports before 1800.

Wind speed recordings were usually given in descriptive terms. Some of them seem to bear a relationship with the Beaufort scale, but this scale was only proposed in the beginning of the 19th century and adopted by most seafaring nations in the 1850's. Since logbooks from four different countries were used, the terminology problem was even four-fold. Hence, the quantitative interpretation of the descriptive expressions of the wind force in m/s – or at least the Beaufort scale – was a major challenge.

The basis of the wind force terminologies varied markedly between the countries. The English, French and Spanish expressed the wind force in ordinary terminology (e.g. strong, or light breeze). The Dutch, however, related the wind force terminology to the amount of sail used. It is obvious that this terminology bears a direct relationship with the ship's operations and the wind force (e.g. 'dubbelgereefde marszeilskoelte' or 'double reefed topsail wind').

The CLIWOC database contains 1,606 Dutch, 1,043 English, 1,019 Spanish and 253 French wind force terms, a total of 3,911 different expressions. Fortunately only 927 of them made up 98% of all reports. It was decided to use flexible lookup-tables for the conversion, enabling changes on second thought. We compared wind force reports from ships of one or more nations during the same voyage. Analogous comparisons were carried out with observations from different ship types and sizes[8]. Although differences remained, in particular between the different countries[9], it seems that the current translation tables[7] are of sufficient quality to allow for meaningful analyses of the pre-1854 climate and its variability[10].

The database and its documentation

The first public version[9] of the CLIWOC database, Version 1.5, was released in early 2004. It can be accessed through a dedicated CLIWOC website (see below). An important development is its simultaneous availability through the ICOADS website in a standardized data format. Release version 1.5 is

available in IMMA[11] format, which is being developed under JCOMM. Release 1.5 contains 280,280 records. The database includes information on date, time and position of each report, followed by the key climatic information for wind direction and wind force. If available, instrumental observations are included as well. This is generally limited to the more recent observations. Though not of interest for climatic studies, additional information (conditions on board, reports on deaths and diseases, sightings of animals, etc.) was keyed as well.

The database is formally documented by the project's final report, submitted in 2004 to the EU[12]. The database is also extensively described in articles in a Special Issue of Climatic Change on CLIWOC. Figure 3 shows that spatial coverage of the CLIWOC data and Figure 4 the annual number of keyed observations per country.

Quality checks; scientific contents

By the end the project, sufficient records were collected to allow for a climatological check of the quality of the wind translations. This was investigated[10,12] by comparing the monthly climatology of the vector-averaged CLIWOC winds with ICOADS. The high level of agreement strengthened our belief that the CLIWOC database can be regarded as reliable[10,13]. The second step was to investigate the capability of backward extending the North Atlantic Oscillation (NAO) index and/or El Niño Southern Oscillation (ENSO) index on basis of anomalies in surface wind patterns[10]. Imprints of both indices could successfully be identified, even for ENSO, despite of the unavoidable limitation of the CLIWOC coverage over the Pacific (Figure 3). We note that this determination of ENSO stands out with respect to other (proxy) techniques, in its capability to resolve the entire phase of ENSO, hence including the La Niña events. The evaluation of the methodologies revealed that the quality of the reconstructions of NAO from CLIWOC surpasses those based on land-based proxies[13-15]. This is very encouraging, as every increase in data density will increase the signal to noise ratio in the reconstructions, while according to an inventory made during CLIWOC, the amount of material waiting to be digitised, allows for an extension of the CLIWOC density by at least a factor eight.

Conclusion

The CLIWOC project was very successful. CLIWOC has proven the intrinsic scientific value of meteoro-

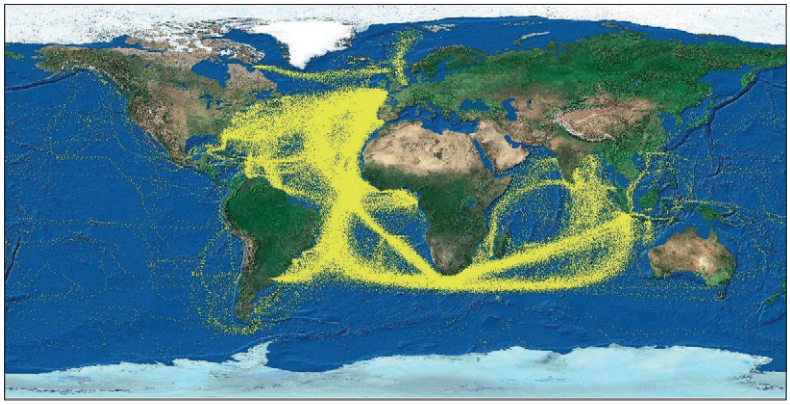

Figure 3. Spatial coverage of all CLIWOC data (1750-1854) from Release 1.5. Every yellow dot represents a ship report.

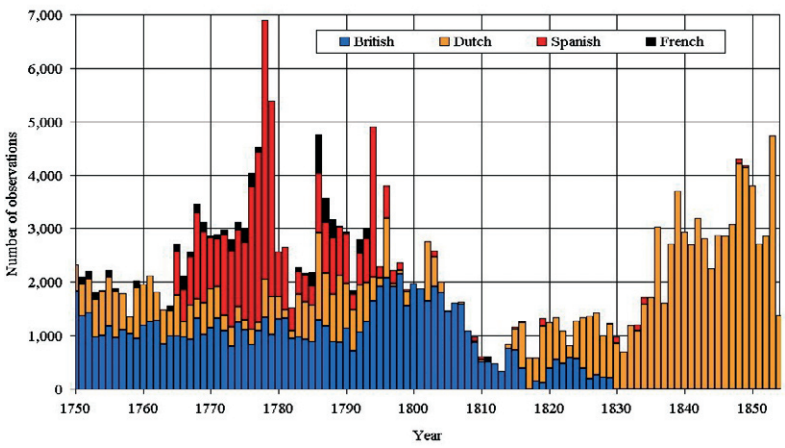

Figure 4. Annual number of keyed observations per country. The decline of the British data density in the 19th century is not a result of lack of data, but rather of deliberate selections made by CLIWOC among the huge amount of available data from English vessels.

logical observations, most notably wind, recorded in early ship logbooks for climatic studies. The CLIWOC database turned out to be able to produce indices of large-scale variability, such as the North Atlantic Oscillation and El Niño Southern Oscillation Index, for a period where no pressure data exist. CLIWOC represents a meaningful and natural backward extension of world climatological oceanic databases such as ICOADS. However, CLIWOC is only a first step, as the available logbooks allow for an extension further backward in time until at least 1690, as well as for a significant increase in data density in the 1750-1854 period. Given the abundance of ship logbooks that are decaying in archives, it is urgent to put more effort into recovering the information. CLIWOC has shown that a more worldwide approach is vital. At the end of 2004, NCDC and the former CLIWOC partners decided that the success of CLIWOC justifies the launch of an up-scaled follow-up. This new project implies an all-embracing effort to collect, image, digitise, and post-process all available pre-1854 European and USA ship logbook data. If in the far future this new project comes to completion, the in our eyes large-scale EU CLIWOC project will probably go in history as its pioneering predecessor.

More information about CLIWOC:
www.ucm.es/info/cliwoc/
www.knmi.nl/cliwoc/

---

1) Jones, P.D. and A. Moberg, 2003. *Hemispheric and large-scale surface air temperature variations: An extensive revision and an update to 2001*. J. Climate, **16**, 206-223.
2) Woodruff, S.D., R.J. Slutz, R.L. Jenne and P.M. Steurer, 1987. *A comprehensive ocean atmosphere data set*. Bull. Amer. Meteor. Soc., **68**, 1239-1250.
3) Woodruff, S.D., H.F. Diaz, J.D. Elms and S.J. Worley, 1998. *COADS Release 2 data and metadata enhancements for improvements of marine surface flux fields*. Phys. Chem. Earth, **23**, 517-527.
4) Parker, D., E. Kent, S.D. Woodruff, D. Dehenauw, D.E. Harrison, T. Manabe, M. Mietus, V. Swail and S.J. Worley, 2004. *The Second JCOMM Workshop on Advances in Marine Climatology*. WMO Bulletin, **53**, 157-159.
5) Worley, S.J., S.D. Woodruff, R.W. Reynolds, S.J. Lubker and N. Lott. *ICOADS Release 2.1 data and products*. Special Issue on CLIMAR-II of the Int. J. Climatology, in press.
6) Woodruff, S.D., H.F. Diaz, S.J. Worley, R.W. Reynolds and S.J. Lubker. *Early ship observational data and ICOADS*. Special Issue on CLIWOC of Climatic Change, in press.
7) CLIWOC Team, 2003. *CLIWOC multilingual meteorological dictionary, An English-Spanish-Dutch-French dictionary of wind terms used by mariners from 1750-1850*. KNMI Publication 205, KNMI, De Bilt, The Netherlands, 49 pp.
8) Wheeler, D.A.. *A study of the accuracy and consistency ships' logbook weather observations and records*. Special Issue on CLIWOC of Climatic Change, in press.
9) Können, G.P. and F.B. Koek. *Description of the CLIWOC database*. Special Issue on CLIWOC of Climatic Change, in press.
10) Jones, P.D. and M. Salmon. *Preliminary reconstructions of the North Atlantic Oscillation and the Southern Oscillation index from wind strength measures taken during the CLIWOC period*. Special Issue on CLIWOC of Climatic Change, in press.
11) Woodruff, S.D. (Ed), 2004. *Archival of data other than in IMMT format. The International Maritime Meteorological Archive (IMMA) Format*. CDC/NOAA, Boulder, USA. Available at *http://www.cdc.noaa.gov/coads/e-doc/imma/imma.pdf*
12) García Herrera, R., D.A. Wheeler, G.P. Können, F.B. Koek, P.D. Jones and M.R. Prieto, 2003. *CLIWOC Final Report*. Available at *http://www.ucm.es/info/cliwoc/Cliwoc_final_report.pdf*
13) Cook, E.R., 2003. *Multi-proxy reconstructions of the North Atlantic Oscillation (NAO) index: A critical review and a new well-verified winter NAO index reconstruction back to AD 1400*. In: The North Atlantic Oscillation, J.W. Hurrell, Y. Kushnir, G. Ottersen and M. Visbeck (Eds), American Geophysical Union, Washington D.C., USA, 63-79.
14) Luterbacher, J., E. Xoplaki, D. Dietrich, P.D. Jones, T.D. Davies, D. Portis, D.F. Gonzales-Rouco, H. von Storch, D. Gyalistras, C. Casty and H. Wanner, 2002. *Extending North Atlantic Oscillation reconstructions back to 1500*. Atmospheric Science Letters, **2**, 114-124. doi: 10.1006/asle.2001.0044.
15) Vinther, B.M., S.J. Johnsen, K.K. Anderson, H.B. Clausen and A.W. Hansen, 2003. *NAO signal recorded in the stable isotopes of Greenland ice cores*. Geophys. Res. Lett., **30**, 7, 1387. doi: 10.1029/2002GL016193.

Simulation of present-day and future climate with RACMO2

Geert Lenderink, Bart van den Hurk, Erik van Meijgaard and Aad van Ulden

Introduction

At present, regional climate models (RCMs) have proven to be useful tools to add local scale detail to (that is, to downscale) the output of coarse-resolution, global climate models. These RCMs represent the atmosphere and the land surface at high resolution (typically 20-50 km) on a limited domain (typically 5000 × 5000 km²). The rationale for such an approach is that the higher resolution of the RCM better resolves fine-scale dynamics, land-sea interaction, the interaction with the topography and small-scale physical processes, like cloud-radiation interaction and boundary-layer processes, while global models with such high resolution are not feasible. Regional climate models are fed at their lateral boundaries by atmospheric fields from global climate models or by data from re-analyses, like ERA40.

In the years 2001-2002 a completely new version of the KNMI Regional Atmospheric Climate Model (RACMO) has been developed. It is based on the HIRLAM dynamical core (version 5.0.6) and the ECMWF (cycle 23r4) physics package. A first run with this new model, RACMO2, using re-analysis boundaries from the ERA15 project (hereafter, the RACMO2-ERA15 simulation) revealed a strong warm and dry bias in summer compared to present-day observations.

The problem

A rather general property of regional climate models is their susceptibility to a warm and dry bias in summer. One of the main feedbacks that may lead to such a bias is the soil-atmosphere feedback. If the soil is dry, evaporation is reduced. This leads to reduced atmospheric humidity, leading to low cloud coverage, high surface radiation and higher evaporation rates. The dryer atmosphere leads to reduced rainfall rates, which also contributes to further drying of the soil. If the representation of this feedback is too strong in the model, this may lead to such drying that no further water is available for evaporation in (late) summer. When evaporation ceases the surface is not cooled anymore, and unrealistic, high surface temperatures result.

In addition, RCMs tend to produce too many blocked circulation patterns, in particular during early summer, even when they are driven with realistic atmospheric circulation statistics at their lateral boundaries. The mechanism of this circulation bias is not yet fully understood.

The warm bias in summer in the RACMO2-ERA-15 simulation is illustrated in Figure 1a. The output of the model is compared to the CRU TS 2.0[1)] data set, which contains time series of observed monthly mean

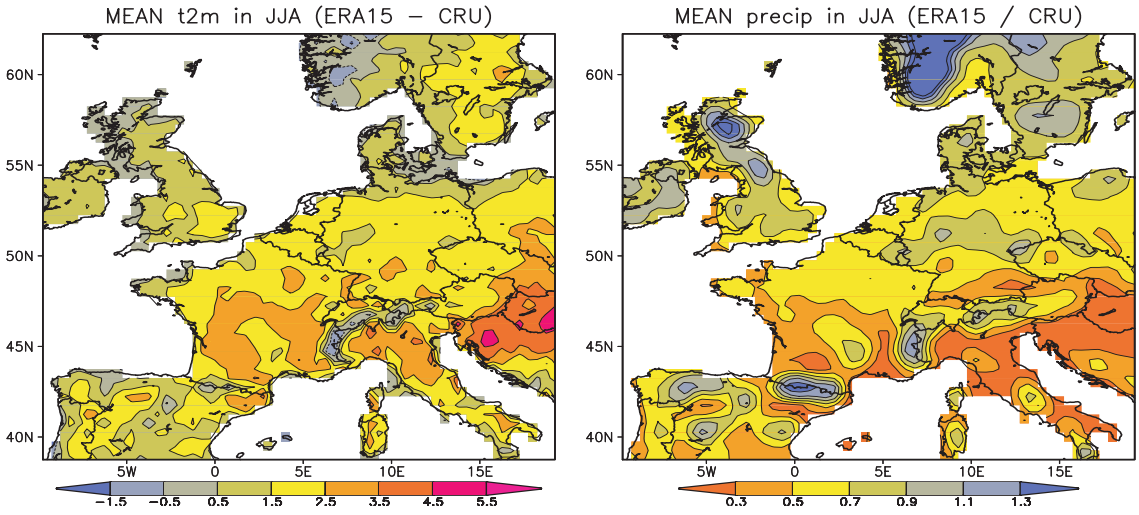

Figure. 1. Bias temperature (in °C) and mean precipitation (fraction of observed) in the RACMO2-ERA-15 simulation, with standard physics, compared to CRU TS 2.0 (1979-1993). The precipitation data has been slightly filtered in space with a Gaussian filter.

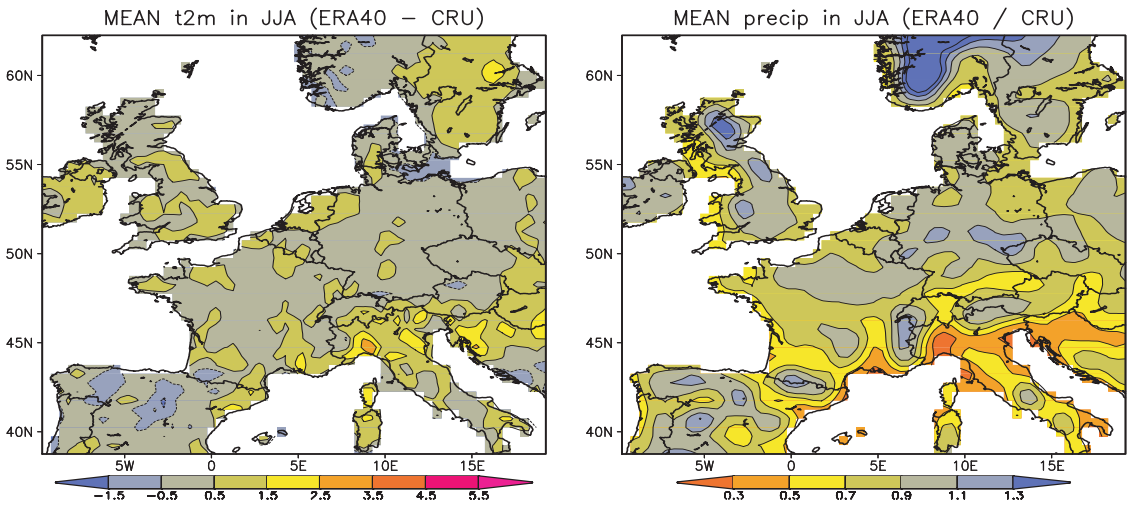

Figure 2. As Figure 1, but now for the RACMO2-ERA-40 simulation (period 1979-1993) using the updated formulation.

A rather general property of regional climate models is their susceptibility to a warm and dry bias in summer

temperatures and precipitation rates aggregated on a regular grid of 0.5 x 0.5 degree. Average temperatures in the model are about 2-3 °C higher than observed for a large area in central Europe, with maxima in southern France and northern Italy, and in southeastern Europe. The warm tail of the distribution provides the major contribution to the bias: for the 10 warmest months out of the 15 years period the bias is about 3-5 °C (not shown). Figure 1b shows the precipitation bias, as a fraction of the observed precipitation. Simulated mean precipitation rates are 30 to 50 % lower than observed.

Before using RACMO2 in climate scenario experiments, it was necessary to obtain a more realistic summer climate by incorporating a minimum set of adjustments to the ECMWF physics. It turned out that modifications in the soil scheme were most effective to reduce the bias of the model. The adjusted version of RACMO2 was verified for a long climate integration using ERA-40 boundaries. After this verification, results obtained using boundaries from a global climate model are presented, in comparison with results of other RCMs.

Results

Modifications

RACMO appeared highly sensitive to the prescription of soil moisture storage capacity, and the way soil moisture affects evaporation[2]. The total thickness of the soil was increased from nearly 3 m to nearly 5 m, divided in four soil layers. A prescribed distribution of plant roots over these layers limits the contribution of the lowest layer to the total evaporation, and most water is extracted from the upper 1.66 m of the soil in the revised scheme (compared to 1.0 m in the original). We reformulated the vegetation 'stress' function, which describes the extent to which evaporation is affected by limited soil-moisture availability. For a moderate drying of the soil the dependency of evaporation on soil moisture is weaker in the new formulation than in the original one. For very dry and very moist soils this dependency is, however, stronger. In spring with plenty of soil moisture this leads to a reduction of evaporation compared to the original scheme. Thus, more soil water remains available to sustain evaporation during summer. Apart from these soil adjustments, the procedure to nest RACMO2 was revised to enhance the control of the global model on the regional model flow patterns.

Verification with ERA-40 boundaries

With the modified formulation a long integration using ERA-40 boundaries has been completed. For the time period corresponding to ERA-15 (1979-1993) the results are shown in Figure 2. Shown is a large improvement: for most areas the bias is reduced to

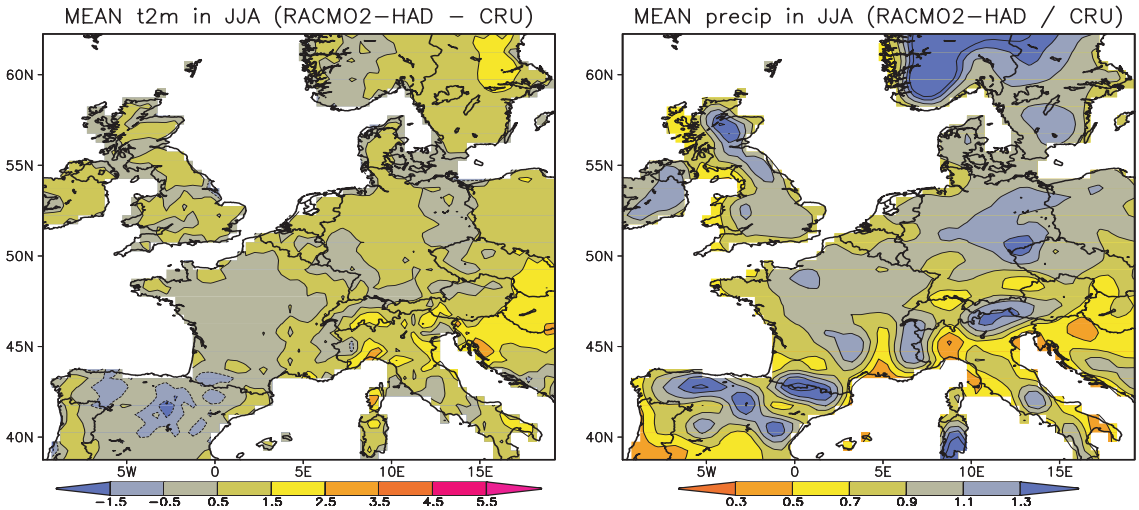

Figure 3. As Figure 1, but now for the RACMO2 (with updated formulation) simulation driven by HadAM3H boundaries (1961-1990)

small values between –1 and +1 °C. At the same time, the precipitation bias is reduced considerably. Most of the improvement of the model performance can be attributed to the changes in the soil parameterisation.

Integrations driven by a climate model

Apart from these integrations driven by re-analysis data, two 30-year integrations with boundaries from the Hadley Centre global climate model HadAM3H were carried out. These integrations were performed in the context of the European project PRUDENCE3), and consisted of a time slice for a control period 1960-1990 and a future period 2070-2100 using the (high) A2 greenhouse gas emission scenario of the IPCC. In this project nine different, European RCMs were used to downscale the same HadAM3H simulation for the control and future period in order to quantify the uncertainty in the predictions of climate change related to the representation of the regional climate (e.g., the presentation of the soil-atmosphere feedback). The summer climate in the control simulation of RACMO2 remains (fairly) close to the ERA-40 driven integration. Figure 3 shows that the temperature in this run is slightly higher than in the ERA-40 driven integration (shown in Figure 2). Also precipitation rates are slightly higher.

The increase in temperature bias can be attributed to the too frequent occurrence of easterly flows imposed by HadAM3H. Figure 4a shows the relation between the strength of the westerly flow and temperature for central Germany for both model integrations and observations for RACMO2. The model results for the control period and the observations have almost identical relationships (the blue and black solid lines in Figure 4a), and the bias in flow characteristics leads to a bias in temperature of roughly 0.5 °C. Also the spread in the simulated temperature is close to the observations. The same plot is also shown (Figure 4b) for another regional climate model, HadAM3H, which is a regional model version, with almost identical physics, of the global model HadAM3H. Compared to RACMO2 the results of HadAM3H show a much stronger dependency of the temperature on the circulation, and a much larger spread in simulated temperatures. The likely cause of this stronger dependency is related to the soil-atmosphere feedback as described above. The results for the future period show an increase in the strength of the temperature-flow dependency in both models, yet much stronger in HadAM3H. In addition, the mean temperature response is significantly larger in HadAM3H, as is the simulated temperature variability.

The strength of the hydrological feedback affects the simulated inter-annual temperature variability. Extremely warm summers are associated with dry soil conditions, particularly later in the summer season. Too shallow soil water storage and too strong soil-atmosphere feedbacks may promote the occurrence of these warm anomalies. Figure 5 shows, as a measure of the variability, the inter-quartile range of the monthly mean temperature for all regional models participating in PRUDENCE. The majority of the models over-predict the temperature range significantly. RACMO2, on the other hand, remains close to the observed variability (CRU), with a slight tendency to underestimate. For most models, like in the RACMO2-ERA15 integration, the overestimation of the inter-quartile range is caused by the overestimation of

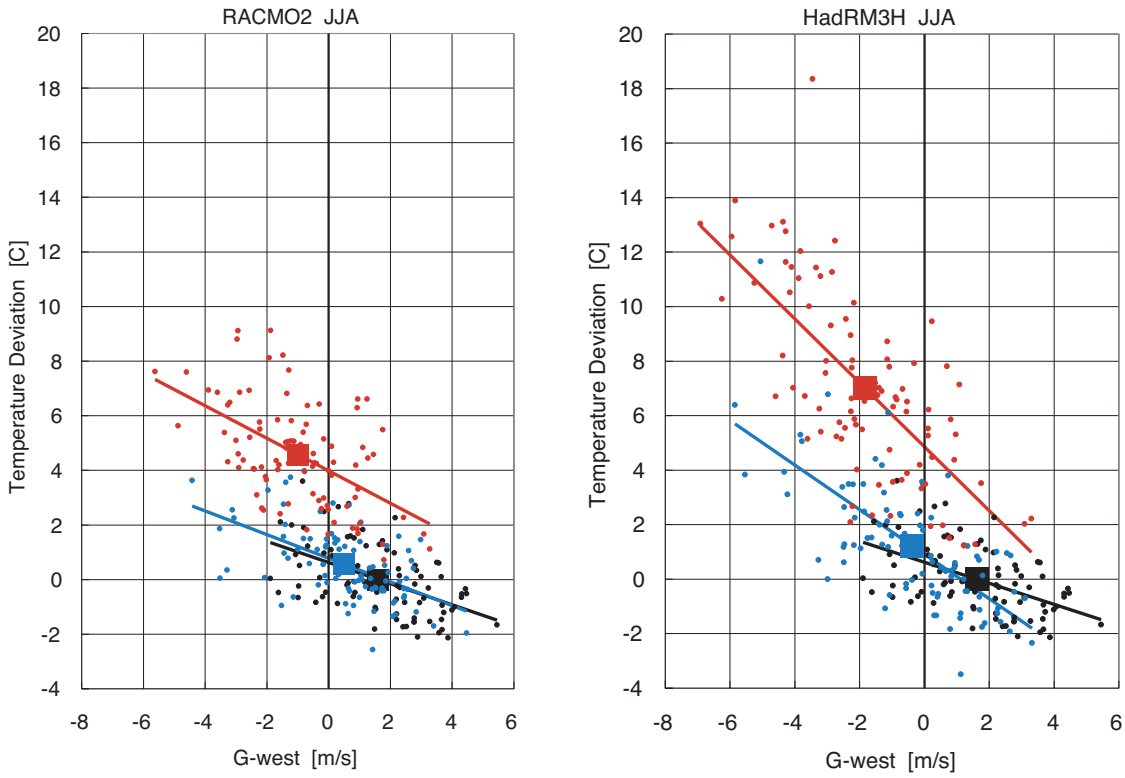

Figure 4. Monthly-mean temperature anomaly (with respect to the observed mean temperature over the period) against strength of the westerly flow. Results are shown for observations (black), and the control (blue) and future (red) climate integrations for RACMO2 (left) and HadAM3H (right). Each symbol represents a single summer month. Solid lines denote linear fits to the data and the large squares indicate the 30-years means.

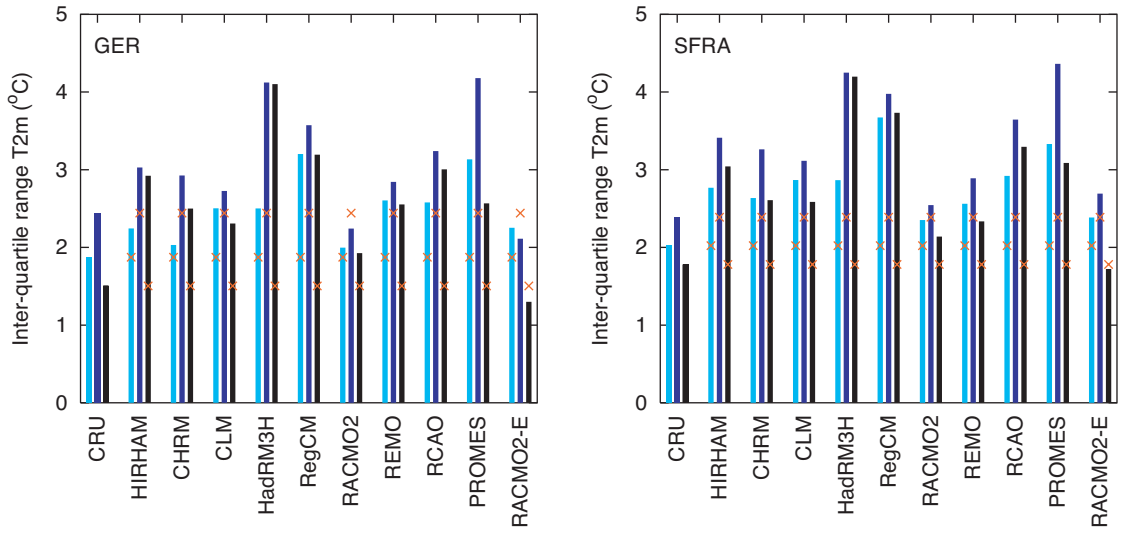

Figure 5. Inter-quartile range (between 75% and 25% percentiles) of monthly mean temperature for the months June (cyan), July (blue) and August (black). Results for central Germany (GER) and southern France (SFRA) are shown for the control simulation driven by HadAM3H boundaries (9 different regional models) and CRU observations (repeatedly shown by red crosses). RACMO2-E denotes the RACMO2-ERA-40 integration.

temperatures in the warm tail of the distribution. Two papers, one on summertime temperature variability and its relation with the modelled surface energy budget, the other on the relation between circulation statistics and temperature variability, have been submitted to the special issue of Climatic Change on the PRUDENCE project.

Outlook

Compared to other regional models RACMO2 has proven to have good skill to reproduce the summer climate of Europe. This applies to the 30-year mean of precipitation and temperature, and also to the inter-annual variability. Despite these strong features, some model weaknesses remain. As such, we mention the representation of convective precipitation, the stable boundary layer (in particular in winter) and boundary layer clouds. The amount of convective precipitation is underestimated, as is visible from the negative bias in mean precipitation in summer in southern Europe, where most rain falls in convective events. Enhanced turbulent mixing in the stable boundary layer leads to a positive temperature bias in winter, in particular in Scandinavia. Boundary layer clouds are not well represented in the present ECMWF physics, and this shortcoming might affect estimates of the indirect aerosol effect; a research field that is currently being explored.

At present, precipitation scenarios based on these RACMO2 simulations are being processed. It should be emphasized that the outcome of regional models crucially depends on the circulation statistics of the forcing boundaries, and these scenarios should therefore account for possible ranges in the predicted changes in flow regimes. Results of projects like Challenge (discussed elsewhere in this bi-annual report) could contribute to quantify this uncertainty range.

---

1) Mitchell, T.D., T.R. Carter, P.D. Jones, H. Hulme and M. New. *A comprehensive set of high resolution grids of monthly climate for Europe and the globe: the observed record (1901-2000) and 16 scenarios (2001-2100)*. Submitted to J. Climate.
2) Lenderink, G., B. van den Hurk, E. van Meijgaard, A. van Ulden and H. Cuijpers, 2003. *Simulation of present-day climate in RACMO2: first results and model developments*. KNMI Technical Report TR-252, KNMI, De Bilt, The Netherlands, 24 pp.
3) Christensen, J.H., T. Carter and F. Giorgi, 2002. *PRUDENCE Employs NEW Methods to Asses European Climate Change*. EOS, **83**, 147.

The coupling between the stratosphere and the troposphere

Peter Siegmund

Introduction

The atmosphere is heated from below by the earth's surface that absorbs the radiation from the sun, and is heated from above by the absorption of solar radiation in the ozone layer at altitudes between about 20 and 50 km. As a result, the temperature near the earth's surface and in the ozone layer is relatively high, whereas the temperature at intermediate levels between the surface and the ozone layer is relatively low. The level with the lowest temperature is called the tropopause. The altitude of the tropopause varies from about 8 km in the extratropics to 18 km in the tropics. The atmospheric layer between the earth's surface and the tropopause, in which the temperature decreases with altitude, is called the troposphere, and the layer directly above the troposphere, in which the temperature increases with altitude, is called the stratosphere. The circulations in the stratosphere and the troposphere are coupled. The vertical and meridional component of the stratospheric circulation, for example, are due to the dissipation in the stratosphere of planetary and gravity waves that originate in the troposphere and propagate towards the stratosphere. This and other effects of the troposphere on the stratosphere are well understood. On the other hand, the effect of the stratosphere on the troposphere is not well understood, and is an important subject of current research. As the mass of the stratosphere is only about 10% of the mass of the troposphere, it was intuitively assumed for a long time that the effect of the stratosphere on the troposphere is relatively small. However, recent research has shown that this effect is much larger than previously thought. The effect of the stratosphere on the troposphere has important consequences for several aspects of weather and climate, two of which will be considered below: 1) the effect of increased greenhouse gas concentrations in the stratosphere on the climate of the troposphere, and 2) extended-range weather predictions, using the stratosphere as a predictor.

The effect of stratospheric cooling on the climate of the troposphere

Stratospheric cooling

The depletion of the stratospheric ozone layer and the increase of greenhouse gas concentrations have led to changes in the climate of the stratosphere. The ozone depletion leads to less absorption of solar radiation in the stratosphere and, consequently, to lower stratospheric temperatures. Also the increased greenhouse gas concentrations lead to lower stratospheric temperatures, which can be understood as follows. Greenhouse gases emit longwave radiation at their local temperature, and absorb longwave radiation that is emitted by the surrounding air, most of which is at lower altitudes. The emission increases with increasing temperature. As in the stratosphere the temperature increases with altitude, the cooling by the emission at the local temperature exceeds the warming by the absorption of the radiation emitted at lower temperatures of the levels below. Thus in the stratosphere an increase in greenhouse gases will lead to more radiative cooling and, consequently, lower temperatures.

Temperature observations in the lower stratosphere (15-20 km) show a cooling trend of ~0.6 °C/decade since 1980. The strongest cooling occurs in the polar lower stratosphere during winter-spring (~3 °C/decade)[1]. The observed cooling in the upper stratosphere (30-50 km) is 1-2 °C /decade since 1980, with the magnitude increasing with altitude. Model simulations of the climate response to ozone depletion and increasing greenhouse gases show an increase of the equator-to-pole temperature gradient and a corresponding increase of the westerly wind in the lower stratosphere, which are both also observed[2].

European winter warming

In the past decades the surface temperature has increased almost globally. The warming is largest over the Northern Hemisphere (NH) winter continents. A part of this warming results from the observed increase in the strength of the westerly wind in the troposphere during the winter season. As described in the next paragraph, this increase might be partially due to the increase in the westerly wind in the lower stratosphere. Stronger westerly winds in the troposphere cause cold winters downstream the cold winter continents, e.g. east of Canada, and warm winters downstream the relatively warm oceans, e.g. over Europe and Siberia. The observed increase in the westerly wind strength accounts for ~30% of the warming of the NH as a whole, and ~50% of the warming of the Eurasian continent[3].

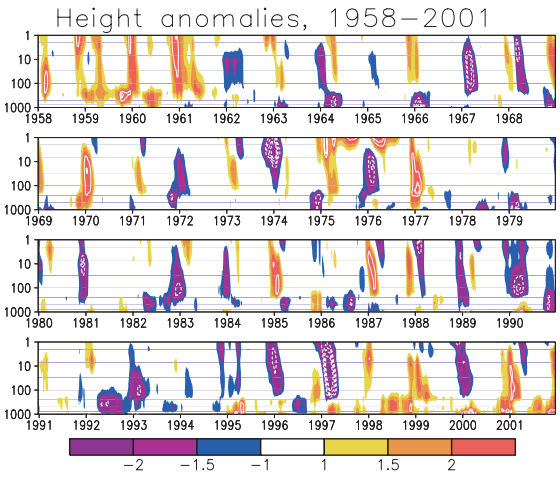

Figure 1. Height anomalies at pressure levels (in hecto-Pascal, hPa) from the surface (1000 hPa) to the top of the stratosphere (1 hPa), during the period 1958-2001. The height has been averaged over the area north of 65 °N. The anomaly for each day is relative to the 1958-2001-average for that calendar day, and has been scaled by the standard deviation of the anomaly's time series for all days of 1958-2001. To put emphasis on seasonal timescales, the daily height data have been low-pass filtered. In clear regions, most of which occur in summer, the absolute value of the height anomaly is less than the standard deviation. Red shading corresponds to high temperatures in the area north of 65 °N, and weak westerly winds; blue shading corresponds to low temperatures, and strong westerly winds.

Our results confirm the suggestion that the observed strengthening of the tropospheric westerly winds during winter is at least partially related to stratospheric climate change

Stratosphere-troposphere coupling

Observations show that on seasonal time-scales enhanced westerly winds in the troposphere correspond to enhanced westerly winds in the stratosphere[3,4,5]. This is illustrated in Figure 1, which shows for the polar region anomalies of the height at pressure levels from the surface to the top of the stratosphere, for the period 1958-2001[5]. This anomaly is a proxy for the strength of the westerly wind. A negative height anomaly corresponds to a stronger than average westerly wind, and a positive anomaly corresponds to a weaker than average westerly wind. The height has been averaged over the area north of 65 °N. The anomaly for each day is relative to the 1958-2001-average for that calendar day, and has been scaled by the total time series' standard deviation. To put emphasis on seasonal timescales, a 90-day low-pass filter has been applied. The data have been obtained from the European Centre for Medium-Range Weather Forecasts (ECMWF) 40-year reanalysis project. The anomalies are largest in winter, and in many years comprise both the troposphere and the stratosphere, suggesting a coupling between these layers. An important observation is that anomalies in the stratosphere generally (but not always) precede those in the troposphere, suggesting that variations in the westerly wind in the troposphere are often 'driven' by variations in the westerly wind in the stratosphere.

Although the details of the mechanism of this downward coupling are still being investigated, our recent study[4] suggests that in winter westerly wind variations are communicated from the stratosphere to the troposphere by variations in the meridional (north-south) wind. Our results show that variations in the meridional wind (more precisely: the meridional mass flux) at a given extratropical latitude in the stratosphere and in the troposphere have the same magnitude but opposite signs, and that the variations in the troposphere lag those in the stratosphere by about one day. This time lag leads to changes in the surface pressure averaged over the polar cap north of the given latitude, which in turn lead to variations in the westerly wind in the troposphere. The question whether climate change in the stratosphere induces an increase in the strength of the westerly wind in the troposphere has motivated us to perform idealized experiments with a global climate model comprising both the troposphere and the stratosphere.

A simulation of the separate climate effects of stratospheric and tropospheric CO_2 doubling

Our climate simulations with the ECHAM-Middle Atmosphere climate model[6] show in the northern hemispheric winter middle latitudes a strong increase of the westerlies in the stratosphere and a weak increase of the westerlies in the troposphere in response to uniform CO_2 doubling (Figure 2a). Our attention is focused on this increase in the troposphere. To address the question to what extent this increase is caused by stratospheric and by tropospheric climate change, two additional experiments have been performed in which the CO_2 concentration is doubled only in the stratosphere and only in the troposphere. The north-

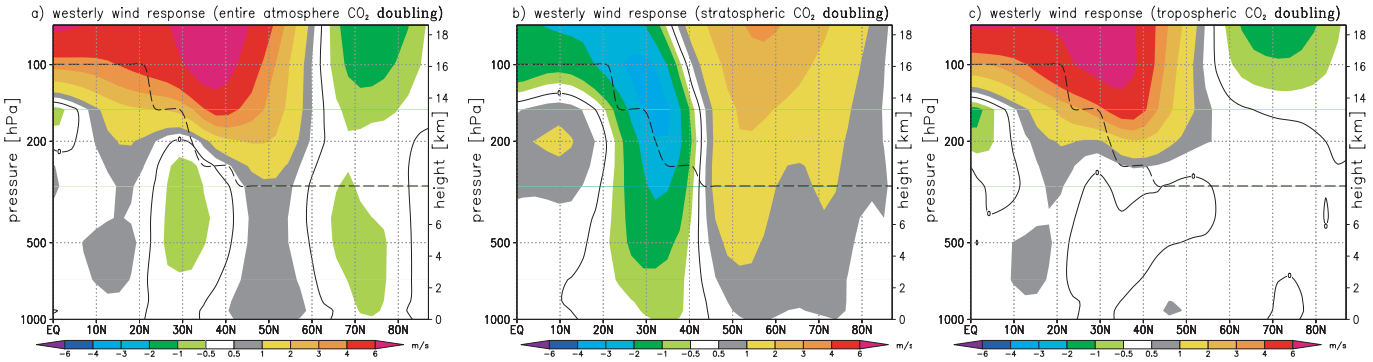

Figure 2. Latitude-altitude distribution of the simulated northern hemispheric longitudinally averaged westerly wind response to a) CO_2 doubling in both the troposphere and the stratosphere, b) CO_2 doubling in only the stratosphere, and c) CO_2 doubling in only the troposphere. Units are m/s. The climate simulations have been performed with a climate model including the troposphere and the entire stratosphere. The results are computed as the difference between 30-year simulations of the doubled CO_2-climate and of the present-day climate. The dashed line denotes the position of the tropopause, separating the troposphere and the stratosphere. Positive values denote an increase in the westerly wind relative to the present-day climate simulation, negative values denote a decrease.

ern hemispheric middle latitude tropospheric westerlies also strengthen in response to stratospheric CO_2 doubling (Figure 2b), but do not significantly change in response to tropospheric CO_2 doubling (Figure 2c). The sum of the separate responses to tropospheric and stratospheric CO_2 doubling is in most regions approximately equal to the uniformly doubled CO_2 response. Therefore, the artificial separation of the CO_2 doubling in a stratospheric and a tropospheric part is physically meaningful. These results suggest that the increase of tropospheric westerlies in response to uniform CO_2 doubling can be attributed mainly to the stratospheric CO_2 doubling. Our results confirm the suggestion that the observed strengthening of the tropospheric westerly winds during winter is at least partially related to stratospheric climate change.

Extended-range weather predictions, using the stratosphere as a predictor

A recent study has shown that the stratosphere can be used as a predictor of the troposphere on time scales beyond 10 days[7]. We have computed the skill of the stratospheric height and temperature in predicting the pressure and temperature at the earth's surface on time scales beyond 10 days[5]. The results have been obtained by analysing atmospheric circulation and temperature data for the period 1958-2001. Below two examples are shown.

Figure 3 shows the skill of the height at different pressure levels in the troposphere and the stratosphere in predicting the surface pressure at the extended range during the winter season. Both the height and the surface pressure have been averaged over the region north of 65 °N. The surface pressure has been averaged over a range of periods, from 1 to 80 days. The first day of this period lags the height predictor by 10 days. Before computing the skill, the long-term mean annual cycles have been subtracted. The predictive skill is equal to the square of the correlation between the predictor and the predicted quantity, multiplied by 100%. Figure 3 shows that the predictive skill is largest around 100 hPa, which is in the lower stratosphere, for an averaging period of about two weeks, i.e. for the average over the period from 10 to 24 days after the day of the predictor. Many aspects of the weather near the surface are related to the surface pressure. Thus, we find that during winter there exists a significant effect of the stratosphere on the time-averaged weather on time scales beyond 10 days.

As a second example, Figure 4 shows the pattern of the correlation between the area (north of 65 °N)-mean height at 50 hPa, which is at the stratospheric altitude of about 20 km, and the winter surface temperature in the Northern Hemisphere. The temperature is a monthly average for December, January and February, and the stratospheric predictor precedes the first day of these months by ten days. The figure shows that the correlation is largest around 65 °N and over the Mediterranean region. Although the correlations over the Mediterranean region are comparably large when a tropospheric predictor would be used (not shown), around 65 °N only the stratospheric predictor has a large correlation with the surface temperature. The large correlations around 65 °N can be understood as follows. A small (i.e. smaller than the long-term mean for the time of the year) stratospheric height corresponds to a low strato-

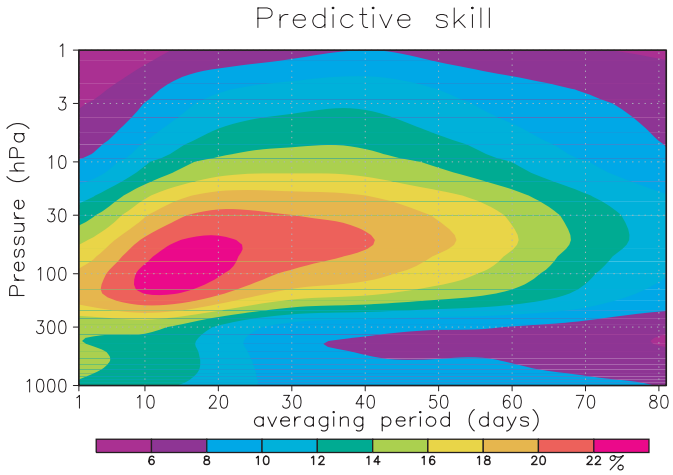

Figure 3. Winter (December, January, February)-averaged skill of the height at different pressure levels (vertical axis) in the troposphere and the stratosphere in predicting the surface pressure. The height and the surface pressure have been averaged over the region north of 65 °N. The surface pressure has been averaged over a range of periods, from 1 to 80 days (horizontal axis); the first day of this period lags the height predictor by 10 days.

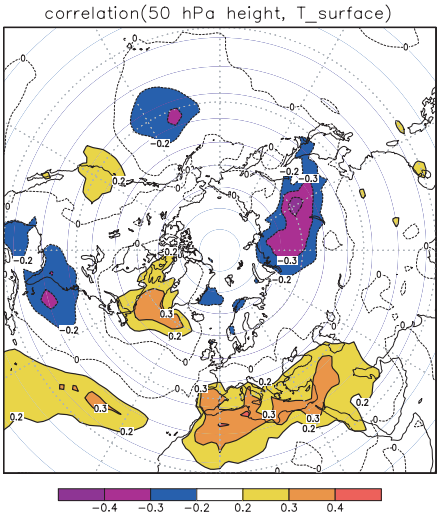

Figure 4. The geographical pattern of the correlation between the area (north of 65 °N)-mean height at 50 hPa and the monthly (December, January, February)-mean surface temperature in the northern hemisphere. The first day of the month over which is averaged lags the time of the 50 hPa-height by ten days.

spheric temperature, and to a strong westerly wind in both the stratosphere and the troposphere. As mentioned above, a strong westerly wind corresponds to a cold (i.e. colder than the long-term mean) winter downstream the cold winter continents, e.g. over the northwest Atlantic, and to a warm winter downstream the relatively warm oceans, particularly over Siberia. As a result, the correlations in Figure 4 over the latter area are negative, and over the former area positive.

The correlation between the stratospheric height and the near-surface temperature in The Netherlands is very small.

In conclusion, our results show that the stratosphere influences the troposphere at the daily[4], the monthly[5], and the climatological[6] time scale.

1) Ramaswamy, V. and 16 co-authors, 2001. *Stratospheric temperature trends: Observations and model simulations*. Rev. Geophys., **39**, 71-122.
2) Langematz, U., M. Kunze, K. Krüger and K. Labitzke, 2003. *Thermal and dynamical changes of the stratosphere since 1979 and their link to ozone and CO_2 changes*. J. Geophys. Res., **108**, doi:10.129/2002JD002069.
3) Thompson, D. W. J., J.M. Wallace and G.C. Hegerl, 2000. *Annular Modes in the Extratropical Circulation, Part II Trends*. J. Climate, **13**, 1018-1036.
4) Sigmond, M., P. Siegmund and H. Kelder, 2003. *Analysis of the coupling between the stratospheric meridional wind and the surface level zonal wind during 1979-93 NH extratropical winter*. Climate Dyn., **21**, 211-219.
5) Siegmund, P., *Stratospheric polar cap-mean height and temperature as extended-range weather predictors*. Mon. Wea. Rev., in press.
6) Sigmond, M., P. Siegmund, E. Manzini and H. Kelder, 2004. *A simulation of the separate climate effects of middle atmospheric and tropospheric CO_2 doubling*. J. Climate, **17**, 2352-2367.
7) Baldwin, M.P., D.B. Stephenson, D.W.J. Thompson, T.J. Dunkerton, A.J. Charlton and A. O'Neill, 2003. *Stratospheric memory and extended-range weather forecasts*. Science, **301**, 636-640.

Past climate changes

Nanne Weber

Introduction

In the past decade, climate research has made considerable progress in understanding and modelling climate variability on timescales of years to decades. The accurate simulation of the current climate, and its decadal variability, is an important benchmark for climate models. However, it does not guarantee the correct simulation of variability on longer timescales or climatic conditions very different from today's. These features are difficult to evaluate on the basis of the instrumental record, since it is only 50-150 years long and climatic changes have been relatively modest during this period. Proxy data are the only source of information for variability on timescales longer than a few decades or on past (pre-instrumental) climatic behavior. There is a growing research effort to reconstruct the historic evolution of the climate from such indirect data that register variations in, for example, temperature or precipitation. Testing climate models against these data is crucial for evaluating their ability to predict the impact of anthropogenic changes in atmospheric composition in the coming centuries.

This chapter first discusses model results for the mid-Holocene period and two extensions of this work, namely the simulation of cyclic variations in climate and possible future climatic changes. Next it describes some studies on the role of solar forcing, followed by an outlook to the last glacial.

The mid-Holocene Optimum, a PMIP subproject

The international Paleoclimate Modelling Intercomparison Project (PMIP) was initiated in 1991 with a twofold goal. Firstly, to coordinate the systematic intercomparison of climate model simulations for key periods in the past and, secondly, to foster the creation of well-documented data sets for use in model evaluation. PMIP is endorsed by both the World Climate Research Programme and the International Geosphere Biosphere Project. One of the PMIP foci is the mid-Holocene Optimum (6000 years ago). This was a relatively warm period with stable climatic conditions, which is thought to have been an important stimulus for the emergence of agriculture.

The seasonal and geographical distribution of the insolation received at the top of the atmosphere undergoes periodic variations due to changes in the precession and obliquity parameters of the Earth's orbit. Here precession refers to the date of perihelion and obliquity is the tilt of the rotation axis of the Earth. At 6000 years before present the orbital configuration was such that northern hemisphere summer insolation was considerably stronger than today, especially at low latitudes. This results in an enhanced summer heating of the Sahara and the Eurasian continent compared to the nearby oceans, a stronger low-level convergence into the monsoon lows and an intensified summer monsoon precipitation. This is the most pronounced response in model simulations, which is in qualitative agreement with proxy data[1]. The amplitude of the response of ECBilt, KNMI's intermediate-complexity climate model, was found to be at the lower end of the range obtained from the PMIP simulations. Over northern Africa, proxy data of

Figure 1. Sapropels (organic-rich, dark layers), which were deposited in the deeper parts of the Mediterranean Sea, are now exposed above sea level due to tectonic uplift. These sapropels at Sicily were formed ca. 9 million years ago.

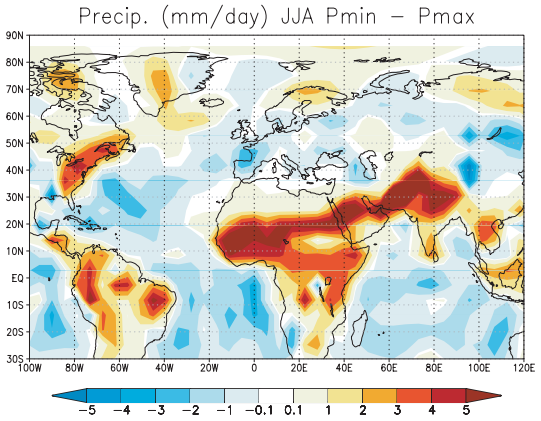

Figure 2a. The response in June-July-August precipitation (in mm/day) to a change in the precession parameter in the ECBilt climate model. The figure shows precipitation during minimum precession minus precipitation during maximum precession.

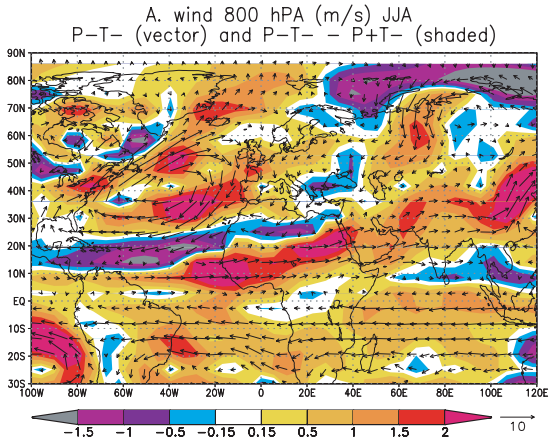

Figure 2b. The wind vector at 800 hPa during minimum precession (in m/s; arrows) and the response in the wind strength to a change in the precession parameter (in m/s; shaded). The increase in precipitation shown in (a) is associated with a stronger inflow of moist air from the Atlantic ocean.

As models underestimate the magnitude of past monsoon changes, these results are considered as a lower bound for the applied business-as-usual scenario

vegetation and lake levels indicate a northward shift by 5-10° of the Sahara/Sahel boundary. A detailed model-data comparison[2] shows that climate models consistently underestimate this northward extension as well as the magnitude of the precipitation changes required to produce the reconstructed vegetation and lake levels.

Cyclic variations in circum-Mediterranean climate

Sediment records often exhibit periodic signals which can be related to the orbital forcing. One example are sapropels (organic-rich dark layers; Figure 1), which have been deposited in the deeper parts of the Mediterranean Sea throughout at least the last 13 million years. A statistical analysis[3] of these deep-sea sediment cores points to a precession dominated oscillation (periodicity of ca. 21,000 years) and a weaker obliquity signal (periodicity of ca. 41,000 years). The paleoclimatic origin of sapropels is not yet fully understood. The most common hypothesis is that sapropels are deposited when the African summer monsoon is strong and the associated discharge of the river Nile is high, resulting in oxygen depletion of bottom waters through the cessation of deep-water formation.

A series of model experiments[4] was used to test this hypothesis. The ECBilt model indeed exhibits a precession signal and a weaker obliquity signal[5] in the discharge of the river Nile. Increased monsoonal precipitation is found to be related to local insolation forcing (due to precession; Figure 2). In addition, heating of the Asian landmass at midlatitudes plays a role (due to precession and obliquity). Proxy data for sea-surface salinity in the outflow region of the Nile confirm that the model underestimates the climatic signal, consistent with results from the PMIP model-data comparison for the mid-Holocene. The inclusion of vegetation feedbacks[6] is found to enhance variations in monsoon precipitation considerably (Figure 3). In addition to the signals in the Nile discharge, precipitation over the Mediterranean Sea itself and the river discharge from the northern borderlands show a precession and obliquity signal. In an ocean circulation model the influence of increased Nile discharge is found to be strictly located to the Eastern coast, while increased discharge from European rivers and increased local precipitation cause lower salinity over the entire Mediterranean Sea. This leads to an alternative hypothesis, namely that the deposition of sapropels is caused by changes in the hydrological cycle over the northern borderlands and over the Mediterranean Sea itself. This hypothesis will be further examined at the Faculty of Geosciences of Utrecht University, by studying ultra-long sedimen-

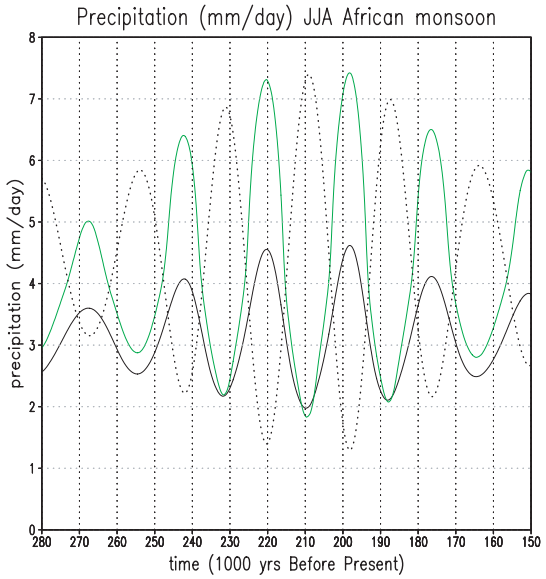

Figure 3. June-July-August precipitation (in mm/day; solid lines) as it evolves with time in response to variations in the precession parameter (dotted line). Time on the horizontal axis in thousands of years before present. The results are obtained with an atmosphere-ocean model (black line) and with an atmosphere-ocean-vegetation model (green line) (CLIMBER-2). Vegetation feedbacks result in a stronger response, which is in better agreement with proxy data.

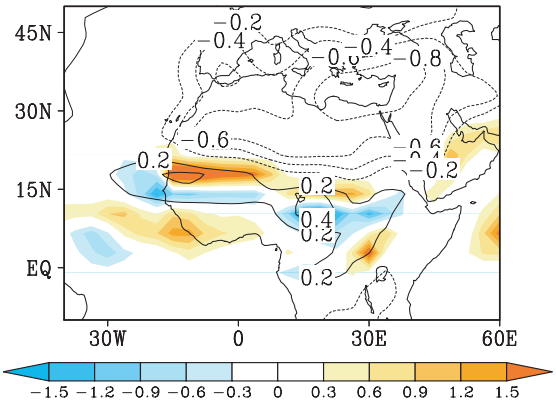

Figure 4. The response in summer precipitation (in mm/day; shaded) and in geopotential height at 925 hPa (in dm; contours) to an anthropogenic increase in Greenhouse Gases. The figure shows the mean difference between the periods 2050-2080 and 1950-1980 in 62 coupled model runs (see chapter Selten and Kliphuis). The decrease in geopotential height over the Sahara indicates reduced surface pressure and enhanced low level flow carrying moist air from the Atlantic into the Sahel region (compare Figure 2).

tary records from Spain, Greece and Marocco for the presence (or absence) of orbital signals.

The past as a key for the future?

An ensemble of model simulations of the anthropogenic warming at the end of this century shows an enhanced heating of the Sahara compared to the Atlantic ocean. In this case the enhanced land-sea contrast is probably related to the formation of low-level clouds over the ocean, which tempers the warming. This results in an anomalous low pressure over the Sahara and an increase in Sahel rainfall between 1980 and 2080 (Figure 4). The increase is relatively small, but it goes with a strongly reduced probability of prolonged droughts (Figure 5). As models underestimate the magnitude of past monsoon changes, these results are considered[7] as a lower bound for the applied business-as-usual scenario.

Variations in solar irradiance during the Holocene

Solar forcing is generally thought to play an important role in generating climate variability on sub-orbital timescales. This was studied[8] in a transient experiment with the ECBilt model for the last 10,000 year (the Holocene). A timescale analysis of the results shows that the response of atmospheric parameters to the solar irradiance forcing can be characterised as the direct response of a system with a large thermal inertia. This is evident in, for example, surface air temperature, which shows a strong response (and

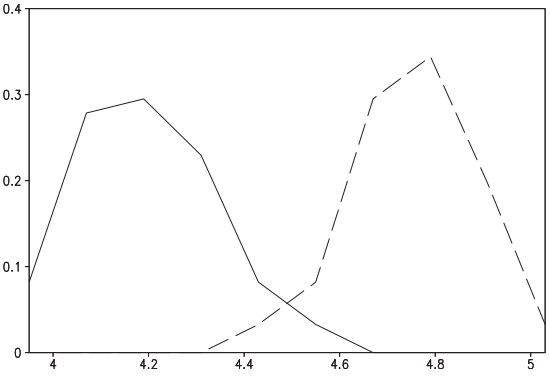

Figure 5. The probability density function of 30-year mean summer rainfall for the Sahel region for the period 1950-1980 (solid curve) and 2050-2080 (dashed curve), computed from 62 coupled model runs. The model predicts that the probability of prolonged droughts will be much lower at the end of this century than it was previously.

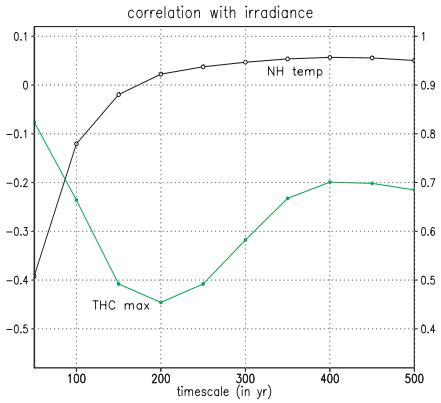

Figure 6. The correlation between variations in solar irradiance and the annual northern-hemisphere temperature (black line; right-hand axis) and an index of the strength of the Atlantic ocean's overturning circulation (green line; left-hand axis) in a 10,000 year solar-forced experiment with the ECBilt climate model.

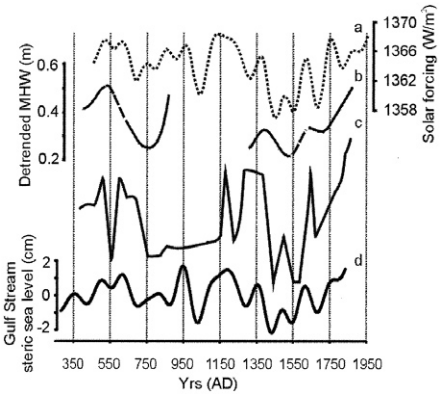

Figure 7. An estimate of solar irradiance variations (upper curve), sea-level reconstructions from Clinton and Farm River Marsh (both in Connecticut, USA; middle two curves) and the average of two 2000-year long ECBilt simulations of sea level in the Gulf Stream area (lower curve). All sea-level curves have been shifted 125 year back in time.

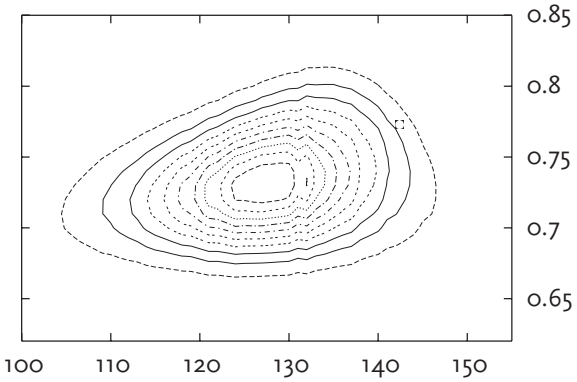

Figure 8. The probability density function of the optimum correlation and associated lag (in years) between variations in solar irradiance and the reconstructed sea level at Clinton. The sea-level reconstruction is dated at a number of depths using ^{14}C dating. The probability density function is computed from 108 different realisations which are constructed by randomly chosing the age of the sample within the dating uncertainty. The contour interval is 5.104, the dot represents the location of the original sea-level record.

better correlations) for long timescales (Figure 6). At shorter timescales the response is attenuated by the thermal inertia of the oceans. This explains the presence of solar signals in proxy data with low temporal resolution which registrate only the longer timescales, whereas those signals are difficult to detect in the short instrumental record.

The oceanic response, on the other hand, is strongly modified by internal feedback processes. This results in an optimum correlation of the thermohaline circulation at a preferred range of timescales (Figure 6) and a significant spectral peak at 200-250 year, which is absent in a reference run[9]. A detailed analysis shows that the underlying mechanism is based on the generation of salinity anomalies in the northern Atlantic due to solar-forced variations in circulation strength, which are advected southward in the deep ocean. This modifies the north-south density contrast, resulting in a resonant response when the period of the forcing matches the advection timescale of the salinity anomalies.

A number of shorter experiments[10] for the late Holocene show that centennial variations in regional sea level can be associated with the southward propagating deep-ocean salinity anomalies. This puts forward a mechanism for centennial variations in a sea-level record for the northwest Atlantic, which is reconstructed from foraminifera in cores from salt marshes (figure 7). This record optimally fits the solar forcing with a lag of roughly 125 years, which is consistent with the transit time from the deep-water formation sites in the northern Atlantic to the location of the salt marshes in Connecticut (USA). Although this result seems very encouraging, the error margins inherent in radiocarbon dating of the sea-level record may render the satisfactory match fortuitous. Therefore, we devised the following test[11] to quantify the effect of the dating uncertainties. A large number of differ-

ent realisations of the sea-level record were made by randomly selecting individual ages within the ±1 sigma error band of each of the 48 independent ^{14}C measurements. This results in a probability density function of the optimum correlation and associated lag (Figure 8), which shows that the match between forcing and sea-level variations is a robust feature.

Forward to the last glacial

As a next step in the PMIP project KNMI will examine the last glacial maximum (21000 years ago) with its intermediate-complexity climate model. The cold climate of this period is strongly affected by internal feedback processes and especially modelling its ocean state is a challenge. It is expected that this exercise will provide a benchmark for the model's representation of the Atlantic freshwater budget.

Conclusions

Climate models tend to underestimate the response of the African summer monsoon to orbital forcing during the mid-Holocene and earlier time periods. However, qualitatively they capture the response well and this enhances our confidence in the ability of models to predict future changes in Sahel rainfall. Model experiments allow to examine the mechanisms underlying orbital and solar signals identified in proxy records. This has lead to an alternative hypothesis for sapropel formation in the Mediteranean Sea over the last 13 million years, and to a possible explanation for solar signals in reconstructed sea-level records in the northwest Atlantic during the late Holocene. Solar forcing was found to excite an internal model of variability on centennial timescales in the thermohaline circulation, while there is a direct response of atmospheric parameters.

1) Joussaume, S. and 33 co-authors, 1999. *Monsoon changes for 6000 years ago: results of 18 simulations from PMIP*. Geophys. Res. Lett, **26**, 859-862.
2) Braconnot, P., S. Harrison, S. Joussaume, C.D. Hewitt, A. Kitoh, J. Kutzbach, Z. Liu, B. Otto-Bliesner, J. Syktus and S.L. Weber, 2004. *Evaluation of PMIP coupled ocean-atmosphere simulations of the mid-Holocene*. In: Past climate variability through Europe and Africa, R.W. Battarbee, F. Gasse and C.E. Stickley (Eds.), Springer, Dordrecht, The Netherlands, 515-533.
3) Lourens, L.J., A. Antonarakou, F.J. Hilgen, A.A.M. van Hoof, C. Vergnaud-Grazzini and W.J. Zachariasse, 1996. *Evaluation of the Plio-Pleistocene astronomical timescale*. Paleoceanography, **11**, 391-413.
4) Tuenter, E., 2004. *Modeling orbital induced variations in circum-Mediterranean climate*. PhD Thesis, University of Utrecht, The Netherlands, 152 pp.
5) Tuenter, E., S.L. Weber, F.J. Hilgen and L.J. Lourens, 2003. *The response of the African summer monsoon to remote and local forcing due to precession and obliquity*. Glob. Plan. Change, **36**, 219-235.
6) Tuenter, E., S.L. Weber, F.J. Hilgen, L.J. Lourens and A. Ganapolski, 2005. *Simulation of climate phase lags in the response to precession and obliquity forcing, and the role of vegetation*. Climate Dyn., **24**, 279-295.
7) Haarsma, R.J., F. Selten, S.L. Weber and M. Kliphuis. *Sahel rainfall variability and response to Greenhouse warming*. Submitted to Geophys. Res. Lett..
8) Weber, S.L., T.J. Cowley and G. van der Schrier, 2004. *Solar irradiance forcing of centennial climate variability during the Holocene*. Climate Dyn., **22**, 539-553.
9) Weber, S.L. and J. Oerlemans, 2003. *Holocene glacier variability: three case studies using an intermediate-complexity climate model*. The Holocene, **13**, 353-363.
10) Van der Schrier, G., S.L. Weber and S.S. Drijfhout, 2002. *Sea level changes in the North Atlantic by solar forcing and internal variability*. Climate Dyn., **19**, 435-447.
11) Van de Plassche, O., G. van der Schrier, S.L. Weber, W.R. Gehrels and A.J. Wright, 2003. *Sea-level variability in the northwest Atlantic during the past 1500 years: a delayed response to solar forcing?* Geophys. Res. Lett, **30**, 17558-17561.

Assessing the skill of seasonal forecasts

Geert Jan van Oldenborgh

Introduction

Seasonal forecasts are predictions of the average weather up to one year ahead. Ordinary weather forecasts are limited to one or two weeks because of the chaos of the highly non-linear weather system. However, in some regions, in some seasons, the average weather is influenced in a predictable way by slowly varying boundary conditions, such as sea surface temperature (SST), ice or land conditions. These factors can have a local or a remote effect. Remote influences are called teleconnections.

The most important factor influencing the global weather on seasonal time scales is the El Niño – Southern Oscillation (ENSO) phenomenon in the eastern equatorial Pacific Ocean. There, SST can be up to five degrees above normal; this situation is called El Niño, the Christmas boy, as it often peaks at the end of the year. SST below normal is denoted by La Niña, the girl. El Niño and La Niña last for many months and can be predicted reasonably well up to half a year ahead. ENSO predictions are used to make seasonal forecasts of the weather in regions and seasons affected by ENSO teleconnections. The forecast is often computed as a shift in the mean weather depending on the strength and phase of ENSO. This means that simple, often linear, forecast models can be very useful in seasonal forecasting. In fact statistical models based on linear ENSO teleconnections are used in many locations throughout the world.

In contrast, dynamical seasonal forecast models, such as the system run operationally at the European Centre for Medium-Range Weather Forecasts (ECMWF), consist of ensembles of integrations of coupled General Circulation Models (GCMs) of the ocean and atmosphere, similar to the models used to make the weather forecast. If the models were perfect, this approach would yield better forecasts, both for ENSO itself and for the teleconnections that give rise to seasonal forecasts, as all physical processes thought to be relevant are included. In practice model errors limit the skill, and there has been some debate whether the theoretical advantages of GCMs translate in better forecasts than those produced by statistical models[1].

Methods

KNMI has made a systematic investigation[2] of the skill of the ECMWF seasonal forecast model[3], in collaboration with the seasonal forecasting group at the ECMWF. The skill was compared to that of statistical models over the period 1987-2001. The comparison considered both ENSO predictions and seasonal forecasts for temperature and precipitation. Shown here are results for the current version of the operational forecast model, named System-2 (S2).

Firstly, for ENSO forecasts, we compared the ECMWF model forecasts with those of a set of statistical models. Two of these are used operationally at the National Centers for Environmental Prediction (NCEP): the Markov model[4] and Constructed Analogue model[5] (CA). We also consider the ENSO-CLIPER model of Landsea and Knaff[1]. A baseline is given by the Cliper model: the optimal combination of climatology and persistence.

Secondly, ECMWF seasonal forecasts for temperature and precipitation were compared with those of a straightforward statistical model (STAT). This model uses persistence and lagged regressions of observations over 1901-1986 against two patterns of SST. The first pattern is ENSO, the second one the wider decadal ENSO-like pattern. Where the training period indicated a significant relationship between these patterns and observed temperature or precipitation some time later, the same relationship was used to make 'forecasts' for the verification period 1987-2001.

A problem in seasonal forecasting is the lack of data for a thorough verification. The ECMWF has made historical forecasts starting in 1987 for calibration, so only the 15 years 1987-2001 were available. Moreover, the skill of seasonal forecasts depends very strongly on the season and the region. This means one cannot combine forecasts from two different regions, or two different seasons, to increase the number of independent forecasts to compute the skill. Due to this lack of data we use the simplest possible measure of skill: the correlation of the ensemble mean. This is appropriate when biases in the mean state and variance are known and corrected for.

Even a measure as simple as the correlation coefficient has large uncertainties in samples of only 15 data points: if the true skill is zero, there still is a 5% chance that the correlation is 0.44: in those areas the system was just lucky. Conversely, in other areas it

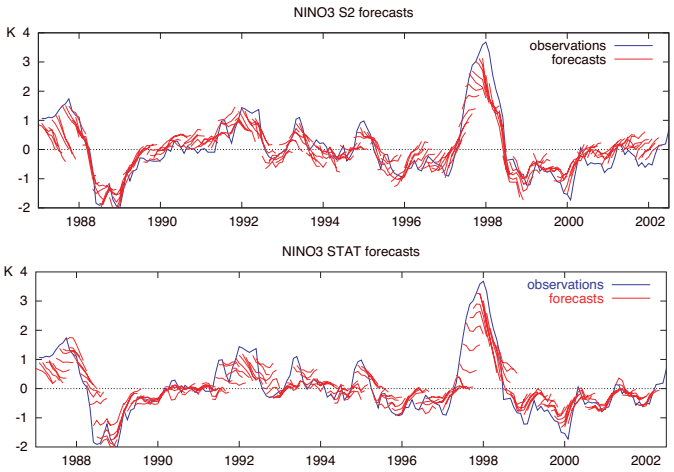

Figure 1. 6-month forecasts of the Niño3 index by the ECMWF seasonal forecast model S2 (top) and a statistical model STAT (bottom).

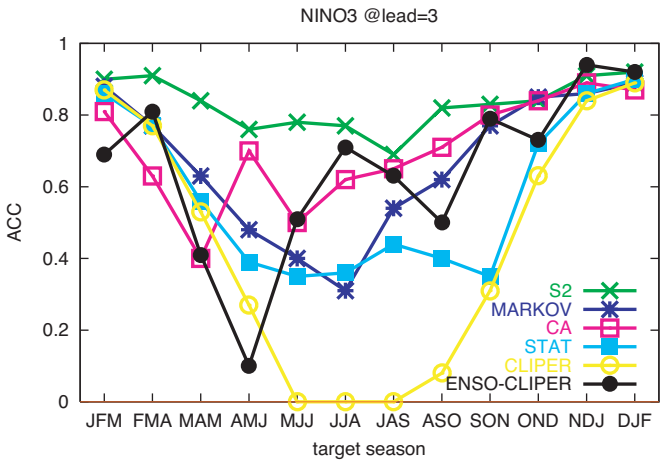

Figure 2. Skill of the Niño3 forecasts at lead time 3 months as function of the target season.

The skill of seasonal forecasts depends very strongly on the season and the region

may have been unlucky a few times. When considering large numbers of possible regions and seasons it is therefore inevitable that some areas of relatively high correlation occur by chance.

El Niño - Southern Oscillation forecasts

The forecasts of the current ECMWF seasonal forecast system (S2) and the statistical forecast system (STAT) of the Niño3 index (SST anomalies averaged over 5°S-5°N, 150°-90°W) over 1987-2001 are shown in Figure 1. The differences between the two are visible in the onset of El Niño (peaks) and La Niña (troughs). S2 correctly predicted the onset and decay of most El Niño and La Niña events. The exceptions are the failure to predict the 1987 El Niño and the tendency in 2001 to start the 2002 El Niño too early. The systematical underestimation of the strength of El Niño is due to a known model deficiency. In contrast, the statistical model failed to predict the onset of every El Niño and La Niña except 1999.

The same difference in behaviour can also be seen in the skill as a function of the target season, with an example for lead-time +3 months shown in Figure 2. (Lead time is defined here as the number of months between analysis time and the beginning of the forecast period.) The strong drop in prediction skill of the SST-based statistical models for forecasts through the boreal spring is known as the spring barrier. This barrier is reduced in the more sophisticated statistical models, and smallest in the dynamical ECMWF model. In making forecasts of SST for boreal winter, however, the statistical models do just as well as the coupled GCM.

Global temperature forecasts

We consider the 2-metre temperature T2m, and compare the seasonal forecasts of deviations from climatology (normal for the time of year) against the observed temperature, represented by the NCEP/NCAR reanalysis[6]. Over the oceans T2m is highly correlated with SST. The results from forecasts from November for December-February are shown in Figure 3 (left panels) for the S2 and STAT models. The statistical model has no forecasts (white) in areas where there is not enough data in the training period 1901-1986, or where persistence and teleconnections were not strong enough to base a forecast on. The colours indicate the skill of the forecasts over 1987-2001. Roughly, red denotes a good forecast, dark orange a useful one, light orange is doubtful and yellow useless.

One sees that temperature over the Indian, Pacific and equatorial Atlantic Oceans is forecast reasonably well by both models. However, over land the skill is lower than over the ocean. In northern South America and along the North American northwest coast one sees well-known ENSO teleconnections in winter as areas where both models have positive skill.

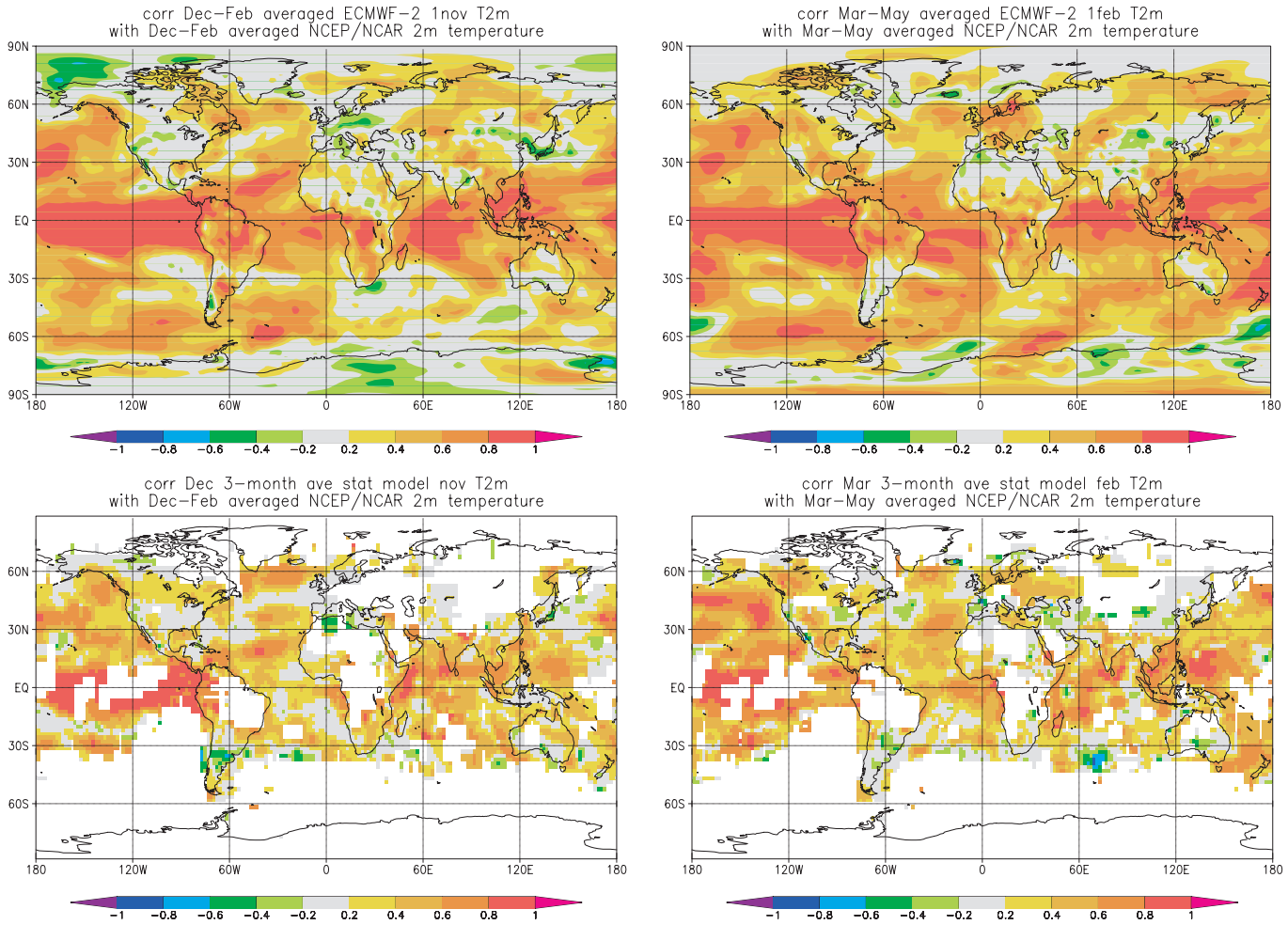

Figure 3. Skill of the T2m forecasts of the ECMWF model S2 (top) and the statistical model STAT (bottom) for December–February (left) and March–May (right) at lead +1 month. Roughly, red denotes a good forecast, dark orange a useful one, light orange is doubtful and yellow useless. White areas did not have enough data or not enough skill to make a forecast.

Comparing the skill plots, one sees that over the oceans the ECMWF model clearly outperforms the statistical model. Over land, the statistical model is hindered by lack of data in many tropical regions. In North America it is slightly better than the ECMWF model, which misrepresents the effects of El Niño along the US-Canada border. In Europe neither model shows any skill in predicting the temperature in winter.

In March-May (Figure 3, right panels) one sees comparable patterns over the oceans. Over land, melting snow and ice gives rise to predictability in North America and Europe in spring. The dynamical model uses this slightly better than the statistical persistence forecast.

Global precipitation forecasts

Precipitation forecasts of the S2 and STAT models are verified against the Global Precipitation Climatology Project[7] analysis, which merges rain gauge observations with satellite estimates.

The strongest effects of ENSO on precipitation occur in eastern Indonesia and the western Pacific during the dry season (Augustus-November). The ECMWF model has skill r=0.8 in these areas in the last three months (September-November from August), see Figure 4 (left panels). These skills are higher than the skill of STAT. As the STAT model is based on ENSO teleconnections, this indicates that there are other factors than ENSO that give rise to predictability. A strong point of a GCM is that these factors are 'automatically' included and increase the skill of the forecasts.

In Australia one sees some skill along the east coast. However, the ECMWF model overextends the telecon-

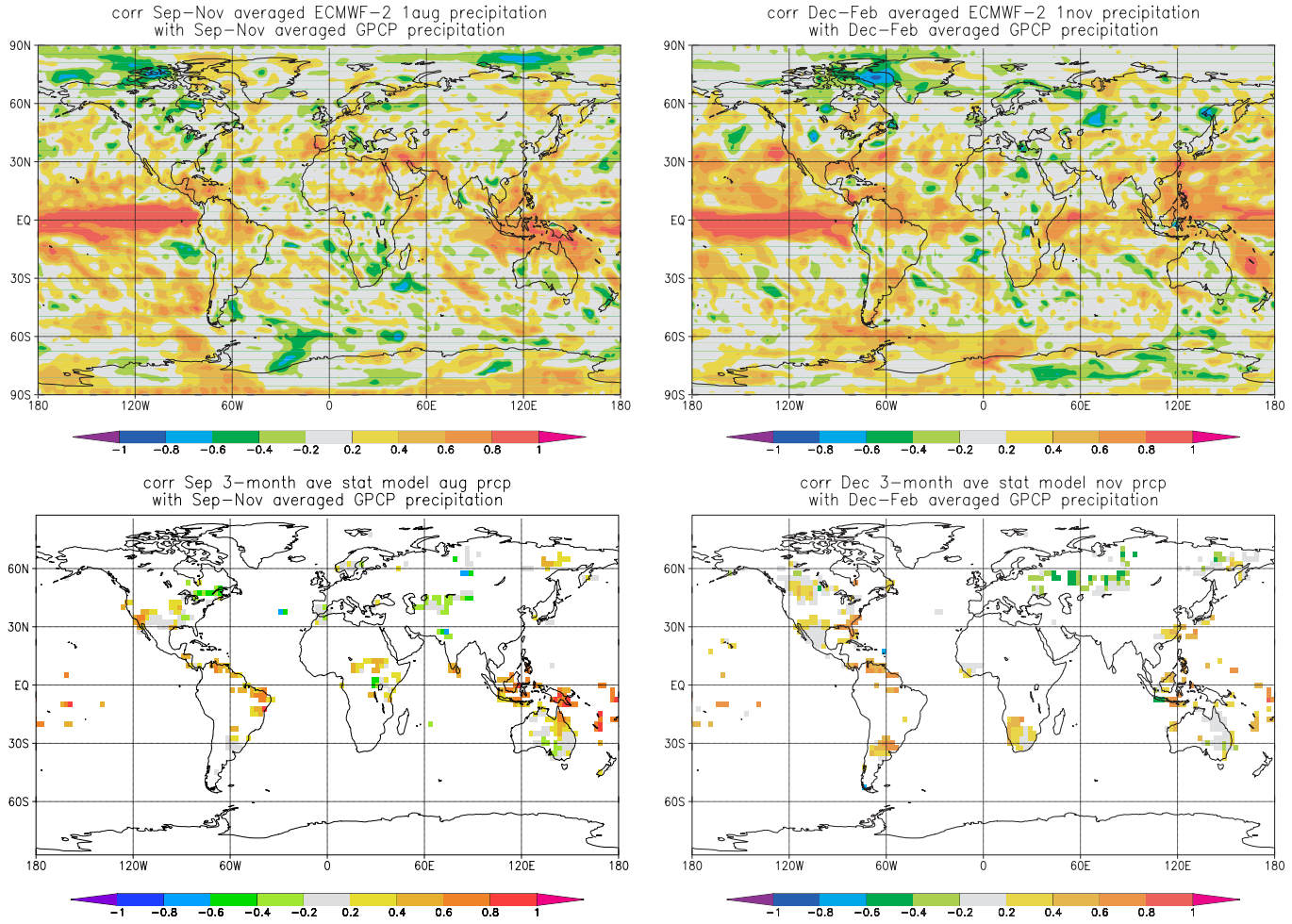

Figure 4. Skill of the precipitation forecasts of the ECMWF model S2 (top) and the statistical model STAT (bottom) for September–November (left) and December–February (right) at lead +1 month.

nection toward the west, leading to forecasts without skill in other parts of Australia. Model deficiencies can give rise to spurious forecasts, when the model itself indicates it can predict the weather when in fact it cannot. Precipitation in Central America and parts of the Caribbean was forecast fairly well by the ECMWF model, as was rainfall in parts of the Middle East and the Sahel. In Europe the model showed skill in the Iberian Peninsula. The statistical model performed much worse in these areas.

The extratropical ENSO teleconnections are strongest in the Americas in December-February. The skill of forecasts for this season is shown in the right panels of Figure 4. The ECMWF model reproduces the historical teleconnection patterns well in Florida, northern South America and southern Brazil. El Niño related rainfall along the coast of Ecuador and northern Peru was also forecast well by the ECMWF model, whereas the linear statistical model did not see a strong enough historical teleconnection to base forecasts on. On the west coast of the US the ECMWF model reproduced the long-term historical pattern of no ENSO effects. In contrast, the teleconnections observed over 1987-2002 were quite strong. It is not clear whether this change is predictable.

Outside the Americas there are also ENSO teleconnections in the season December-February. The ECMWF model used these to make reasonably successful forecasts in eastern China and India in this season. It also showed some skill in southern Africa and Morocco.

Overall view

Due to the limited number of years in the verification period, few of the differences between the ECMWF and statistical forecasts noted above are statistically

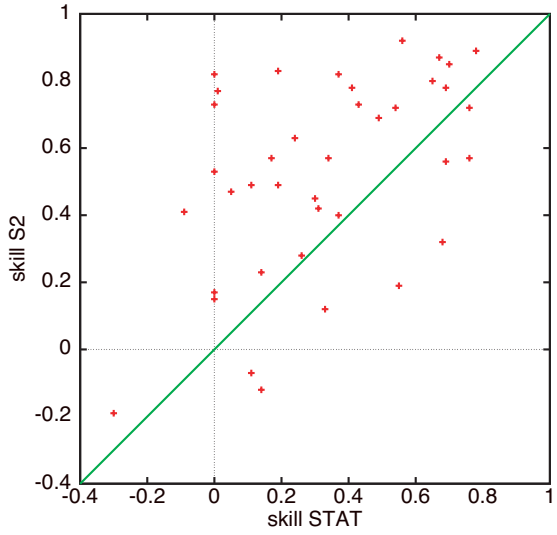

Figure 5. The correlation skill score of the +2 month precipitation forecasts of the ECMWF seasonal forecast model S2 versus that of the statistical model STAT for 40 regions and seasons where skill is expected due to ENSO teleconnections.

significant. The skill of precipitation forecasts for 40 regions and seasons where we expected skill due to ENSO teleconnections is shown together in Figure 5 for a lead-time of +2 months. In 32 out of the 40 cases the ECMWF model performed better than the statistical model. This result is very unlikely to be due to chance, implying that the ECMWF model performs better overall than this statistical model.

Conclusions

The performance of the ECMWF seasonal forecasts has been compared with that of some statistical ENSO forecast models and a simple but global statistical model. The ECMWF forecast model is shown to be better on average than these statistical models in

- predicting El Niño through the spring barrier
- predicting SST in the Indian and Pacific Oceans
- forecasting rain in areas of known ENSO teleconnections.

Many other aspects of performance have not been investigated here, particularly in mid-latitudes. Nonetheless, our results show that there are already a significant number of seasonal forecast 'targets' where the ECMWF numerical model is outperforming straightforward statistical techniques.

All maps have been produced at the KNMI Climate Explorer web site (*http://climexp.knmi.nl*). Readers are invited to investigate the skill in other areas and seasons.

1) Landsea, C.W. and J.A. Knaff, 2000. *How much skill was there in forecasting the very strong 1997-98 El Niño?* Bull. Amer. Meteor. Soc., **81**, 2107-2119.
2) Oldenborgh, G.J. van, M.A. Balmaseda, L. Ferranti, T.N. Stockdale and D.L.T Anderson, 2003. *Did the ECMWF seasonal forecast model outperform a statistical model over the last 15 years?* Technical Memoranda 418, ECMWF, Reading, UK, 32 pp, to appear in J. Climate.
3) Anderson, D.L.T., T. Stockdale, M.A. Balmaseda, L. Ferranti, F. Vitart, P. Doblas-Reyes, R. Hagedorn,

T. Jung, A. Vidard, A. Troccoli and T. Palmer, 2003. *Comparison of the ECMWF seasonal forecast systems 1 and 2, including the relative performance for the 1997/8 El Niño*. Technical Memoranda 404, ECMWF, Reading, UK, 93 pp.

4) Xue, Y., A. Leetmaa and M. Ji, 2000. *ENSO Prediction with Markov Models: The Impact of Sea Level*. J. Climate, **13**, 849-871.
5) Dool, H.M. van den, 1994. *Searching for analogues, how long must one wait?* Tellus, **46A**, 314-324.
6) Kalnay, E. and 20 co-authors, 1996. *The NCEP/NCAR 40-year reanalysis project*. Bull. Amer. Meteor. Soc., **77**, 437-471.
7) Huffman, G. J., R.F. Adler, B. Rudolf, U. Schneider and P.R. Keehn, 1995. *A Technique for Combining Satellite Data, Raingauge Analysis and Model Precipitation Information into Global Precipitation Estimate*. J. Climate, **8**, 1284-1295.

The Challenge project: ensemble simulations of the global climate

Frank Selten and Michael Kliphuis

Introduction

Over the last decade, climate models have grown in complexity at a fast pace. One reason is the inclusion of an increasing number of physical processes that have been found to be relevant. Another reason is the increased numerical resolution in order to capture an extended range of spatial scales. Both factors increase the computational load of climate model simulations.

For a given scenario of future emissions of greenhouse gases (GHG) often just one or a few transient coupled climate simulations are performed in view of the high computational demand of a single simulation. This allows an assessment of the mean climate change. But if one wants to investigate possible changes in the probability and character of extreme events, and changes in the character of internal climate variations such as the El Niño-Southern Oscillation (ENSO) or the North Atlantic Oscillation (NAO), a large ensemble of such simulations is necessary.

The ensemble experiment

To study extreme events and internal climate variations, scientists of the Netherlands Centre for Climate Research (CKO, a collaboration between KNMI, IMAU and RIVM) decided to produce a large ensemble of transient simulations of the global climate. Computing power and data storage were provided by the National Computing Facilities Foundation, which funded the project as a Dutch Computing Challenge Project. The project started in January 2003 and a version of the NCAR Community Climate System Model (CSM1.4) was ported to the SGI 3800 machine of the Academic Computing Centre in Amsterdam (SARA). During the three summer months, 256 of its processors were dedicated to this project. The choice for CSM1.4 was motivated by computational constraints, the fact that this version was carefully tuned to simulate the ENSO phenomenon rather well[1)] and the relatively small effort involved in preparing the system to suit the purpose of the project. A group of about fifteen climate scientists contributed to the design of the experiment and the subsequent analysis of the data.

The CSM1.4 climate model consists of four components. The atmospheric component was run with a $3.75° \times 3.75°$ horizontal grid resolution in latitude and longitude with 18 levels in the vertical, with the highest level at about 35 km. The land model distinguishes between specified vegetation types and contains a comprehensive treatment of surface processes. The ocean model has 25 vertical levels and a 3.6° longitudinal resolution. The latitudinal resolution ranges from 0.9° in the tropics to 1.8° at higher latitudes. The sea ice model includes ice thermodynamics and dynamics.

The system was integrated 62 times for the period 1940-2080. During the historical part of the simulations, GHG concentrations, sulphate aerosols, solar radiation and volcanic aerosols were prescribed according to observational estimates[2)]. From 2000 onwards, the solar constant was held constant and sulphate and volcanic aerosols were kept fixed. Only the GHG concentrations varied according to a business-as-usual scenario[3)]. Each ensemble member starts from a slightly different initial condition by adding a small random perturbation to the initial temperature field of the atmosphere. This perturbation is enough to lead to entirely different atmospheric evolutions within the first couple of weeks of the integrations. This way, independent realizations of the global climate were obtained under the same forcing conditions. The climate variations in the individual ensemble members can be decomposed into an externally forced component and an internally generated component. Averaging over all ensemble members reduces the random, internally generated component of the climate variations, producing an estimate of the externally forced climate change signal. The total amount of data from the computations is 8 Terabytes. This data was transferred to the Mass Storage System at KNMI. A website was launched to communicate the project to the general public *(http://www.knmi.nl/onderzk/CKO/Challenge_live)*.

Simulation of temperatures

Figure 1 shows the global mean surface air temperature as simulated by all 62 members, the ensemble mean and an observational estimate obtained from the Climate Research Unit *(http://www.cru.uea.ac.uk/cru/data/temperature)*. The simulated temperatures cover the observations very well. The random fluctua-

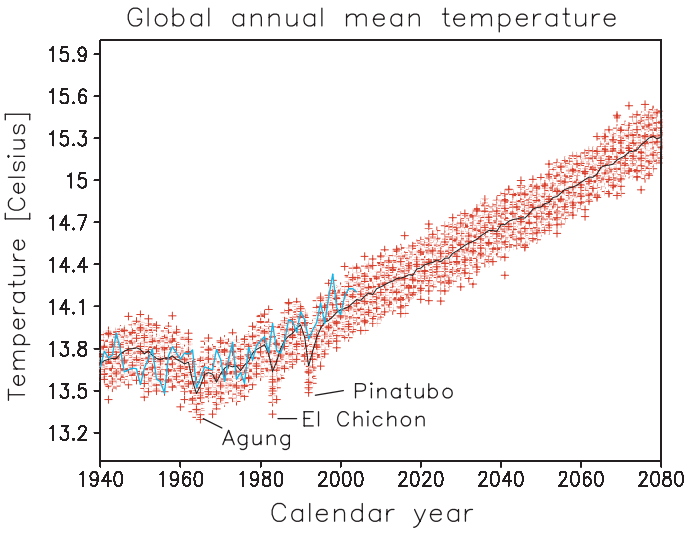

Figure 1. Global annual mean temperatures of all 62 simulations (red crosses), the ensemble mean (black line) and observed temperatures (blue line) from the website of the Climate Research Unit (http://www.cru.uea.ac.uk/cru/data/temperature). Major volcanic eruptions are indicated.

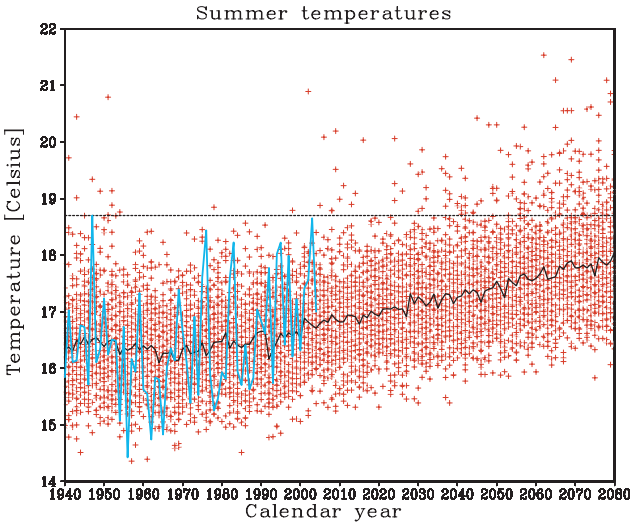

Figure 2. Mean summer temperatures in a grid box partially overlapping the Netherlands of all 62 simulations (red crosses), the ensemble mean (black line) and observed temperatures at weather station De Bilt in the Netherlands (blue line). A summer bias of –1.7 °C has been removed from the simulated temperatures. The horizontal line marks the warmest summer on record.

62 Independent realizations of the global climate were obtained under the same forcing conditions

tions around the ensemble mean are on the order of several tenths of a degree. The ensemble mean itself reflects the effect of the time-dependent climate forcings. The effect of the volcanoes, Agung (1963), El Chichon (1982) and Pinatubo (1991) is clearly visible as a temporary cooling on the order of several tenths of a degree. The temperature decrease between 1940-1970 is related to the prescribed decreased solar radiation in this period. The temperature rise after 2000 is solely due to the increased concentrations of GHGs. Extrapolating the rise to 2100 leads to a global warming of about 1.5 °C in this century. This is on the low side of the range (1.4 to 5.8 °C) established in the IPCC Third Assessment Report[4]. This range is based on results from different model simulations and emission scenarios.

For a grid box, partially overlapping the Netherlands, we calculated the mean summer temperatures in all simulations (Figure 2) and compared these with temperatures from weather station De Bilt in the Netherlands. Apart from a summer bias of -1.7 °C, the range of simulated temperatures covers the observations well. This bias is at least partly caused by a westerly bias in the simulated circulation. The hottest summer on record (1947) is also a rare event in the simulations. The probability of extreme hot summers increases stronger than might be expected on the basis of the mean warming.

This result suggests that the probability density function (PDF) of temperature not simply shifts with the mean, but changes shape in the warming climate. Figure 3 shows the PDF for August for the same grid box. In August, the probability density in the warm tail rises. The one in 10 year warm event warms twice as much as the mean warming. Additional analyses have shown that the depletion of soil moisture is one contributing factor, because this limits the cooling effect of evaporation. In the future period, hot summers with low evaporation occur more often. Another contribution is a change in the mean summer circulation with a stronger southeasterly flow over Europe bringing warm, dry air into the region.

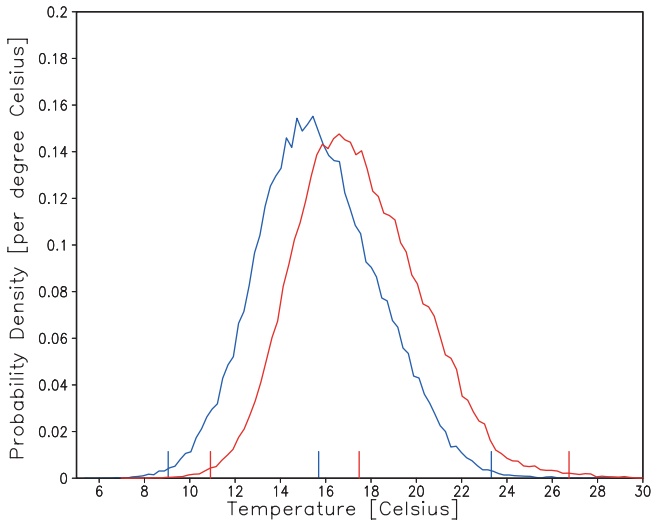

Figure 3. Probability density function of daily mean temperatures in the same grid box as mentioned in Figure 2 in August for the period 1951-1980 (blue) and 2051-2080 (red). Short vertical lines indicate the temperatures of the one in 10 year cold extremes (left ones), the mean temperatures (middle ones) and the one in 10 year warm extremes (right ones).

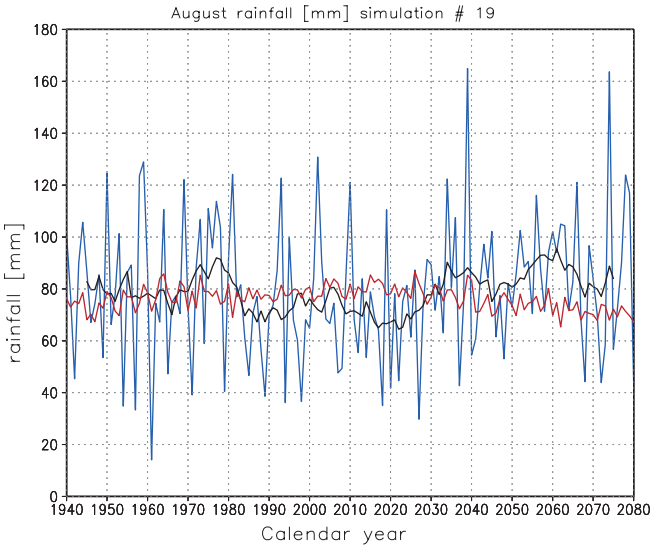

Figure 4. August precipitation time series (blue) of simulation 19 in the same grid box as mentioned in Figure 2. In addition, the ensemble mean time series is shown (red) and a low-pass filtered time series using an eleven-year running mean (black) to emphasize the decadal variations.

Internal climate variations

Strong internal climate variations occur on a regional scale that temporarily mask or enhance the trend induced by the increasing levels of greenhouse gases. For example, the precipitation time series of simulation 19 (Figure 4) in August in the same grid box as mentioned above show large variations at decadal timescales. These internal variations are larger than the GHG induced trend, which is given by the ensemble mean. Note that the GHG induced trend starts decreasing beyond 2020 after an initial increase.

Large natural variations are also found in the simulated strength of the North Atlantic Oscillation (NAO)[5], a large-scale pattern of atmospheric surface pressure variations. This pattern is characterized by a simultaneous intensification (or weakening) of the Icelandic low- and the Azores high-pressure system and describes much of the year-to-year variations in the mean winter circulation in the North Atlantic area. As such it has a large impact on the European winter climate. Figure 5 shows the simulated NAO (a) and its impact on winter surface air temperatures (b). These patterns compare well with observations (not shown).

Figure 6a presents an index of the strength of the NAO for ensemble member 13 (red) and 32 (orange) and the observations (blue) to illustrate the temporal variations in the NAO. The observations show a large trend over the past 40 years, which is well reproduced in ensemble member 13, but not in member 32. Averaging over all ensemble members (the black curve in figure 6a) reveals no significant systematic change in the NAO index in response to the applied forcings. Random, internally generated climate variations are large enough to explain the observed long-term NAO trend and thus need not be related to the increased GHG concentrations.

Observed and simulated Eurasian winter temperature variations are plotted in Figure 6b. In ensemble member 13, the warming rate over the period 1960-2000 is comparable to the observed rate of about 1 °C per decade. This is about four times the ensemble mean warming. In contrast, ensemble member 32 simulates a cooling trend during that same period of about 0.5 °C per decade. This implies that our ability to predict the future course of the winter temperature in Eurasia over the coming decades is severely limited by the strong, natural variations of the NAO on this timescale. It also implies that large ensembles of climate simulations are necessary to average out the random, unpredictable component and obtain an accurate estimate of the climate change signal related to variations in external factors. Long NAO trends of 30 years or more are by no means rare events. In about half the simulations, at least one such trend is simulated. So nature's course over the past decades might not have been exceptional. But it is rare for simulated NAO index values averaged over a decade to exceed the presently observed value of around 200.

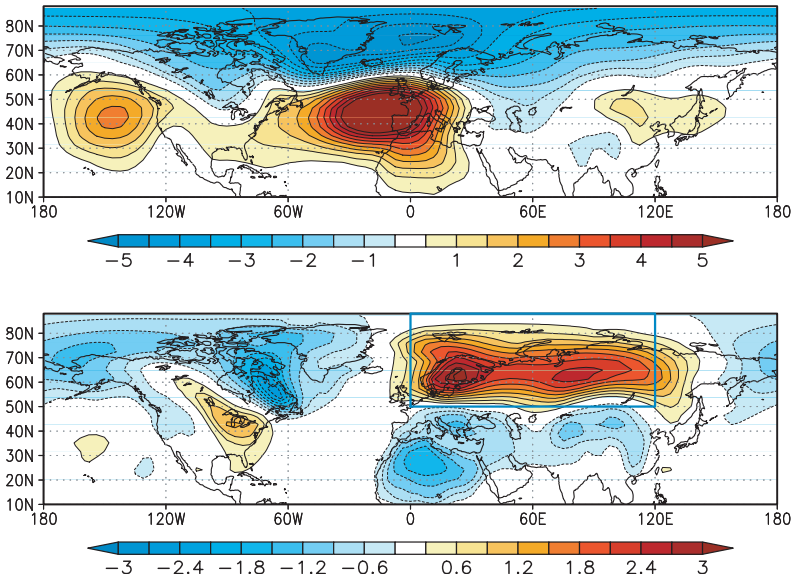

Figure 5. (a) Winter atmospheric pressure variations at sea level that co-vary with the NAO index. (b) Winter surface-air temperature variations that co-vary with the NAO index. Units are in hPa and °C per standard deviation of the NAO index respectively. The NAO index is defined by the projection of winter mean sea-level pressure deviations from the long-term mean onto the first Empirical Orthogonal Function of winter mean sea-level pressure fields for the period 1961-1990 over the North Atlantic area. Observational estimates are from the NCEP/NCAR reanalysis dataset.

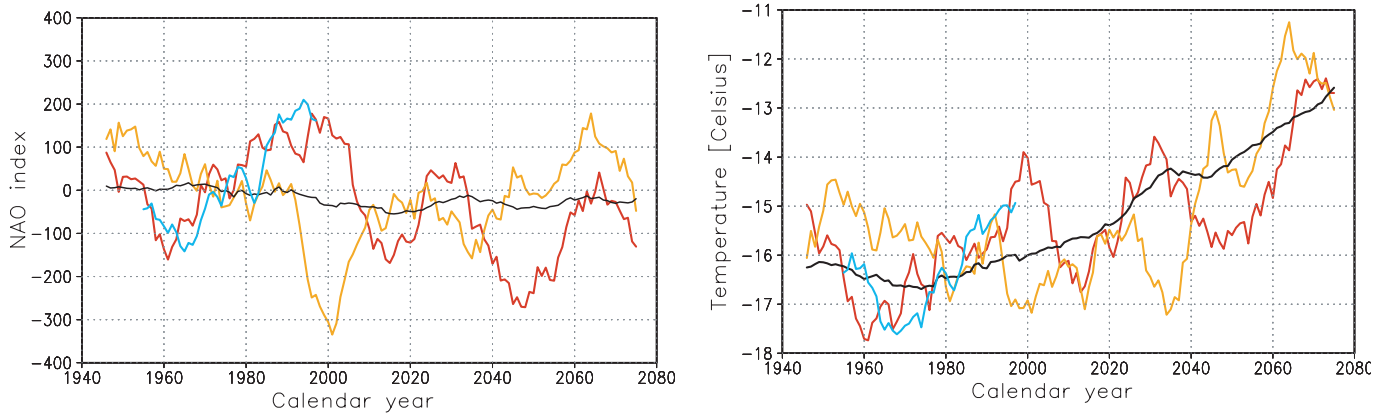

Figure 6. (a) Time series of the NAO index for the observations (blue), ensemble member 13 (red), member 32 (orange) and the mean of all ensemble members (black). Units are in hPa. (b) Winter mean temperatures over Northern Eurasia (averaged over the box indicated in Figure 5b) using the same colour code as panel (a). Units are in °C. A bias of 4.5 °C is added to the simulated temperatures. All time series are low-pass filtered using an eleven-year running mean.

We therefore do not expect that the NAO trend will continue. A slower warming or even a cooling trend over northern Eurasia in the coming decades is likely to occur due to internal climate variations.

Evaluation

The Challenge project has provided valuable information on the occurrences of extremes and the relation between natural and forced climate variations. Nevertheless, it has become apparent that the simulations are far from perfect. For instance, no changes in the characteristics of ENSO were detected, despite the fact that the mean sea surface temperatures warmed[6]. This was attributed to an unrealistic response of the atmospheric winds to changes in tropical SST's, rendering ENSO too stable. Biases in European winter and summer temperatures exist that are related to a westerly bias in the circulation. Daily mean temperatures in winter over land are too persistent around the melting point of snow. The meridional overturning circulation in the North Atlantic Ocean is too strong. Stratospheric dynamics are not well resolved which might have implications for the response of the NAO to the enhanced greenhouse effect. These shortcomings leave much room for improvements and should be kept in mind when interpreting the climate change results.

The Challenge dataset is still being analysed. Characteristics of the most extreme storms over Europe are being studied and simulated in greater detail using a regional climate model. The aim is to evaluate the impact of such a worst-case scenario for the water levels in the Lake IJsselmeer in cooperation with the

'Waarschuwingsdienst voor het IJsselmeer'. Other topics include the study of Sahel rainfall variability, variations in the meridional overturning of the Atlantic Ocean, variability of the Indian Ocean, characteristics of extreme European summers and extra-tropical climate change due to changes in tropical rainfall.

---

1) Otto-Bliesner, B.L. and E.C. Brady, 2001. *Tropical Pacific variability in the NCAR Climate System Model*. J. Climate, **14**, 3587-3607.
2) Ammann, C.M., G.A. Meehl, W.M. Washington and C.S. Zender, 2003. *A monthly and latitudinally varying volcanic forcing dataset in simulations of 20th century climate*. Geophys. Res. Lett., **30**(12), 1657-1660.
3) Dai, A., T.M.L. Wigley, B.A. Boville, J.T. Kiehl and L.E. Buja, 2001. *Climates of the twentieth and twenty-first centuries simulated by the NCAR Climate System Model*. J. Climate, **14**, 485-519.
4) Cubasch, U., G.A. Meehl and 39 co-authors, 2001. *Projections of future climate change*. In: Climate Change 2001: The Scientific Basis. Contribution of Working Group I to the Third Assessment Report of the Intergovernmental Panel on Climate Change (J.T. Houghton et al., Eds.), Cambridge University Press, Cambridge, UK, 527-582.
5) Selten, F.M., G. Branstator, M. Kliphuis and H.A. Dijkstra, 2004. *Tropical origins for recent and future Northern Hemisphere climate change*. Geophys. Res. Lett. , **31**, L21205, doi:10.1029/2004GL020739.
6) Zelle, H., G.J. van Oldenborgh, G. Burgers and H.A. Dijkstra. *El Niño and Global Change: Results from Ensemble Simulations with the NCAR CCSM*. Submitted to J. Climate.

Seismic hazard in the North of The Netherlands

Torild van Eck, Femke Goutbeek, Hein Haak and Bernard Dost

Introduction

Seismicity in The Netherlands occurs mainly in the southeastern part of the country and is related to tectonic movements along the Roer Valley Graben[1]. The Dutch seismological monitoring network of the KNMI, however, also observes earthquakes in the North of The Netherlands since 1986. These earthquakes have been classified as induced seismicity due to the exploration of oil- and gasfields. Here we find one of the world's largest gas reservoirs, the Groningen reservoir, which contains a reserve lasting at least several decades. Most of the felt events are of general annoyance to the local population, occasionally earthquakes up to magnitude $M_L = 3.5$ have caused minor damage (such as cracks in buildings). Therefore, since January 1, 2003, the new Dutch mining legislation requires for each concession a risk analysis and a monitoring plan. Up to now only general hazard estimates were available, i.e. maximum possible earthquake and maximum possible Intensity. Within the context of this new mining law we have been estimating site-specific engineering hazard parameters, i.e. ground motion that can be associated to specific risks.

In general, small earthquakes ($M_L \leq 3.5$) are considered irrelevant in seismic risk analysis. The challenge of this hazard analysis is that it addresses only the effects of small, shallow earthquakes. However, these induced events occur at shallow depths (< 4 km), as compared to 'natural' earthquakes (usually depths > 10 km) and may therefore cause ground motions that reach significant amplitudes. In order to quantify possible risks (= hazard x vulnerability) due to such earthquakes we first need to specify the hazard. In Van Eck et al.[2] we estimated the seismic hazard due to induced seismicity.

Observations

The Dutch seismological monitoring network of the KNMI consists currently of 21 permanent and mobile seismograph stations and 20 accelerometers. Out of these, eleven borehole seismometer strings and 14 accelerometers are especially deployed to improve monitoring of the induced seismicity (Figure 1) to detect and locate all earthquakes with $M_L \geq 1.5$. Since 1986 and up to 2004 the KNMI observed more than 340 induced events within a magnitude range $-0.8 \leq M_L \leq 3.5$. Approximately 60 of those events have been felt. Only nine of those had magnitudes $M_L \geq 3.0$ and no intensities (EMS scale) larger than VI have been observed. All events in the northern part of The Netherlands have been located in or in the direct vicinity of gas reservoirs.

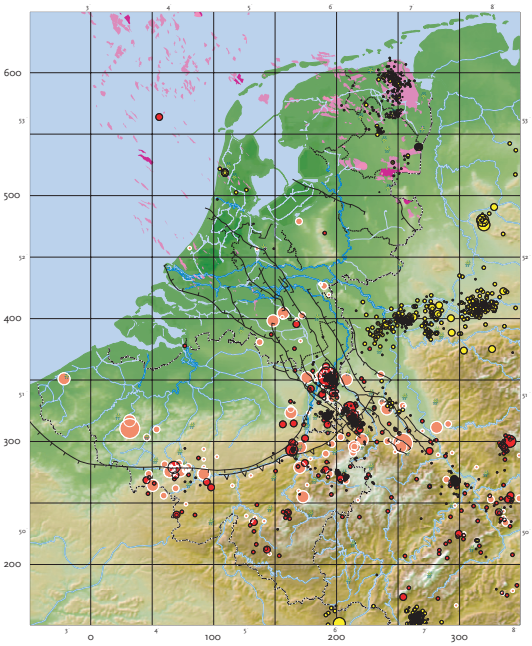

Figure 1. Seismicity in The Netherlands and its immediate surroundings 1900-2004. Red circles indicate natural tectonic earthquakes. Yellow circles are induced events identified by the KNMI. The earthquakes are scaled according to magnitude. Our hazard analysis concerns the induced seismicity in the northern part of the Netherlands[2].

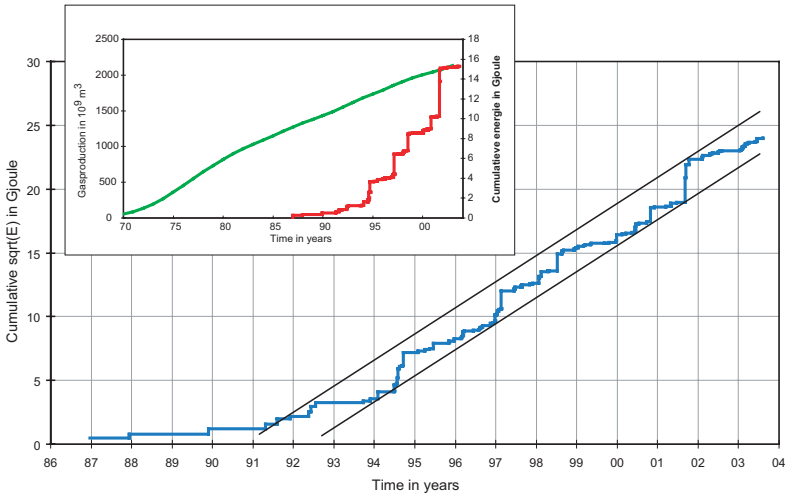

Figure 2. Cumulative of the square root of the earthquake energy in Gjoule (blue curve) of all induced events with M > 1.4 in the northern part of The Netherlands as a function of time. The black straight lines indicate the upper and lower energy boundaries of an assumed stationary seismic energy release. The inlay figure compares the cumulative seismic energy release (red curve) with cumulative gas production on land (green curve). Gas production numbers are kindly supplied by the NITG[2].

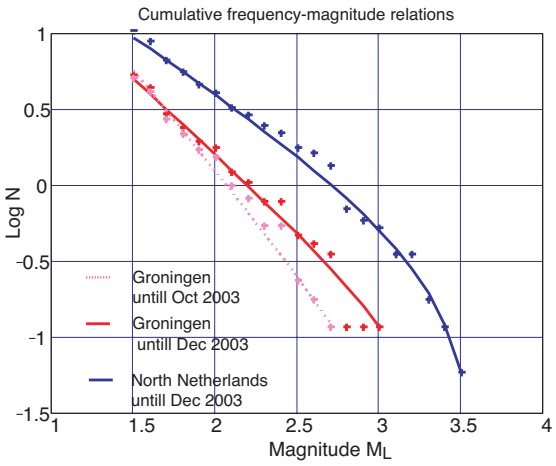

Figure 3. Cumulative annual frequency-magnitude model for all induced seismicity in the North of The Netherlands for the period 1986 - 2003 (solid blue curve) and observations (blue crosses). Also shown is the frequency-magnitude relation for all induced events in the Groningen field excluding (purple broken curve) and including (red curve) three events 2.7 < M < 3.0 that occurred October-November 2003. This suggests that the slope (b-value) of the frequency-magnitude model for a subset of 179 events has a tendency to approach the b-value of the frequency-magnitude model for all earthquakes (340 events)[2].

In general, small earthquakes ($M_L \leq 3.5$) are considered irrelevant in seismic risk analysis. The challenge of this hazard analysis is that it addresses only the effects of small, shallow earthquakes

Although it is generally accepted that induced earthquakes are caused by stress changes and fluid injection in and around the reservoir[3] we have so far not succeeded in correlating changes in gas production (rate) with the occurrence of seismicity[2,4]. We only see a relation in general terms; an overall constant (stationary) rate of production causing a stationary rate of seismic energy release (Figure 2) combined with an exponential distribution of numbers of events as a function of size (Figure 3). This is comparable with statistics of natural events.

In order to obtain more ground motion measurements close to the epicentre the KNMI is deploying 14 accelerometers in the North of The Netherlands. Among the nearly 30 acceleration records obtained within six years we observed in some cases horizontal accelerations exceeding 0.3 g (gravity g = 9.8 m/sec^2). This is considered significant in earthquake engineering terms. However, its duration, determined by the distance and depth of the event, is in our case usually very short, about one cycle. These short strong ground motion pulses have little damaging effect.

Hazard estimation approach

We used a standard probabilistic seismic hazard approach to obtain ground motion estimates. In this approach statistical models of the seismicity distribution and the frequency-magnitude distribution are used in combination with a ground motion prediction equation to obtain the probability of exceeding a certain ground motion at a specific site. This analysis is repeated for a large number of grid points at the surface above and in the direct vicinity of the hydrocarbon exploitation fields.

Seismicity distribution model

The induced seismicity occurs generally in and

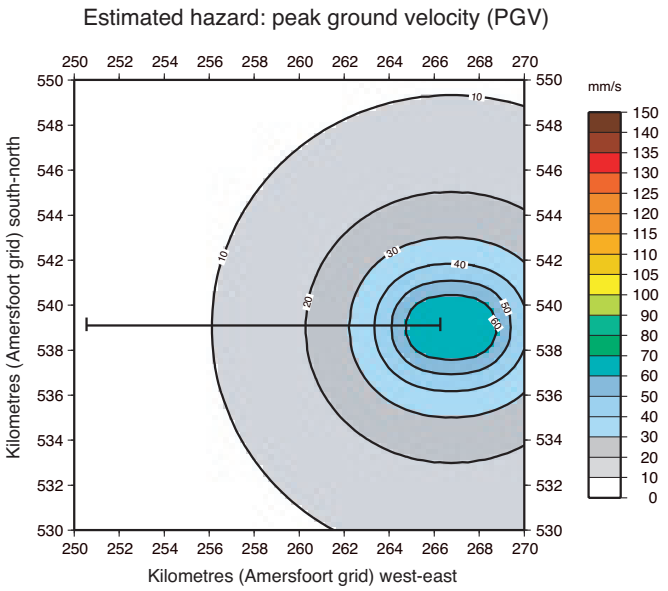

Figure 4. Estimated hazard at the surface above and around the Roswinkel field for a return period of T=100 years, i.e. the peak ground velocity that can be exceeded with an annual probability of 1%. The x- and y-axis indicate distance in kilometres. In the following figure we show the hazard only along a section as indicated.

around the hydrocarbon reservoirs[2] usually around 1.5 to 3.0 km depth. Although we have strong indications that most seismicity is associated with existing faults, we are currently unable to identify precisely the active faults. Consequently, the best seismicity model is currently a homogeneous distribution of the seismicity at 2.5 km depth in the direct vicinity of a hydrocarbon reservoir that has been identified as being seismically active.

Frequency-magnitude model

The frequency of occurrence versus size of all induced seismic events resembles nicely an exponential distribution. Local variations do exist however. We observed, for example, in the period 1994-2004 only four events in the Bergermeer field near Alkmaar, North-Holland, all had $M_L > 2.9$. As we lack a specific physical model explaining such behaviour we adhere to the general statistical frequency-magnitude model as shown in Figure 3.

Ground motion prediction equation

Peak ground velocity and peak ground acceleration are two pragmatic parameters used to characterize seismic hazard. The amplitude can be predicted for a given magnitude and distance using a basic equation, which describes the geometrical spreading and attenuation. The variables of this equation for our region have been estimated using accelerometer and seismometer observations from small and shallow events in The Netherlands[5].

Results

We found that seismic hazard estimates due to induced events in the northern part of the Netherlands are best given in terms of the Peak Ground Velocity (PGV) or, alternatively, the maximum in the 50% damped response spectra at 10 Hz. The results are, among others, presented in maps that give the PGV values with 10% and 1% annual probability of being exceeded once (Figure 4 and 5). For example above the largest Dutch gas field, the Groningen field, we expect PGV of 20 and 30 mm/sec that may be exceeded with a 10% probability in one and 10 years, respectively. Above some small (about 3-4 km_2) gas fields, Roswinkel and Bergermeer, we expect values around 35 and 60 mm/sec, respectively. These values would, if they occur, exceed the Dutch building research (SBR) vibration guidelines. Our systematic approach to estimate the hazard, which includes a sensitivity analysis, provides the decision maker with an insight as to which relevant uncertainties may be decreased and which not. This can be and is consequently used to set research and monitoring priorities.

Discussion

Our presented hazard approach provides first order estimates of (a) the strong ground motion at the surface due to induced seismicity and (b) its probability of occurrence. These are increasingly important for risk analysis in a society with high awareness of disturbances and increased vulnerability. Eventually we would like to replace our analysis with more precise estimates, including local surface geology, exploitation information and detailed local geological and tectonic information. To accomplish this we have and continue cooperation in this aspect with the NITG. Wassing et al.[6] added the local surface geology

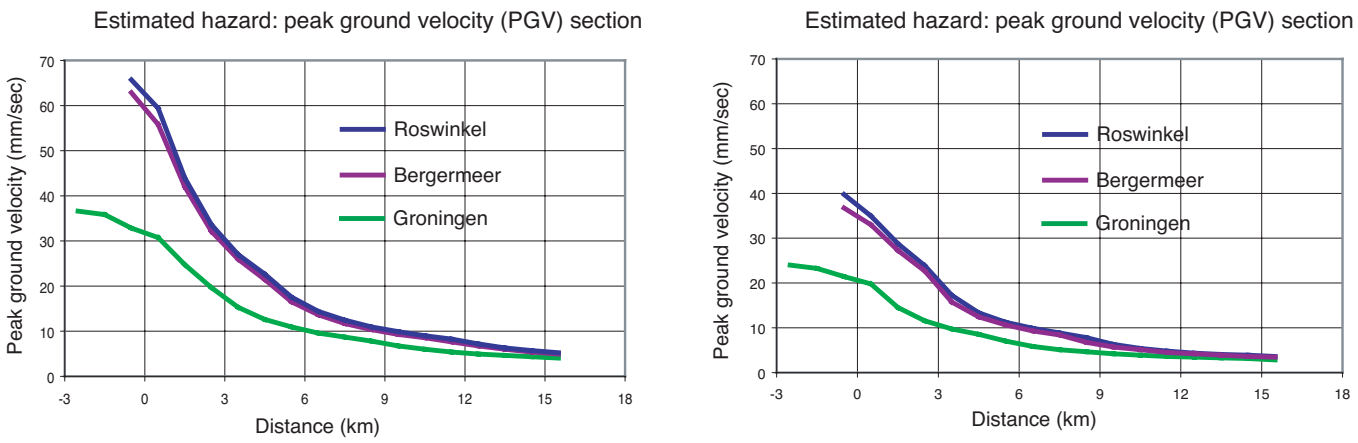

Figure 5. Seismic hazard sections. The estimated hazard at the surface as a function of distance from the surface projection of the exploitation field for three reservoirs; The Groningen, the Bergermeer and the Roswinkel field. The hazard is shown in terms of PGV for a return period of T=100 years (left) and T=10 years (right), i.e. annual probability of exceedance of 1% and 10% respectively.

effect. Van Eijs et al.[4] used the extensive confidential concession and exploitation information, which companies have to provide to the NITG since 2003 within the new mining legislation, to take the first step to include exploitation and geological information. Recently, the KNMI monitoring network has been extended with three strategically placed extra borehole stations to improve detection, location and quantification. Six additional well-placed accelerometers will help us to predict better the strong ground motion at the surface due to these small and shallow induced earthquakes in and around hydrocarbon reservoirs. Last, but not least, we compared the current seismicity statistics with those obtained by De Crook et al.[7] in 1998. From this we conclude that, provided the exploitation rate remains constant, we expect neither more nor less events in the near future.

1) Dost, B. and H. W. Haak. *Seismicity.* In: Wong, Th.E., D.A.J. Batjes and J. de Jager (Eds.), Geology of The Netherlands, in press.
2) Eck, T. van, F.H. Goutbeek, H. Haak and B. Dost. *Seismic hazard due to small shallow earthquakes in The Netherlands.* Engineering Geology, in press.
3) Zoback, M.D. and J.C. Zinke, 2002. *Production-induced Normal faulting in the Valhall and Ekofisk Oil fields.* Pure Appl. Geophys., **159**, 403-420.
4) Eijs, R.M.H.E. van, F.M.M. Mulders, M. Nepveu, C.J. Kenter and B.C. Scheffers. *Correlation between hydrocarbon reservoir properties and induced seismicity in The Netherlands.* Submitted to Engineering Geology.
5) Dost, B., T. van Eck and H. Haak, 2004. *Scaling peak ground acceleration and peak ground velocity recorded in The Netherlands.* Bolletino di Geofisica, **45**, 153 - 168.
6) Wassing, B.B.T., T. van Eck and R.M.H.E. van Eijs, 2004. *Seismisch hazard van geïnduceerde aardbevingen – Integratie van deelstudies.* KNMI Publication 208/TNO Report NITG-04-244B, KNMI, De Bilt, The Netherlands, 10 pp. (in Dutch).
7) Crook, Th. de, H.W. Haak en B.Dost, 1998. *Seismisch risico in Noord-Nederland.* KNMI Technical Report TR-205, KNMI, De Bilt, The Netherlands, 24 pp. (in Dutch).